



**CHARACTERIZATION OF DETONATION PHENOMENA OBSERVED IN  
HIGH-SPEED, VISIBLE IMAGERY**

THESIS

Trevor W. Warren, First Lieutenant, USAF

AFIT/GAP/ENP/06-20

**DEPARTMENT OF THE AIR FORCE  
AIR UNIVERSITY**

**AIR FORCE INSTITUTE OF TECHNOLOGY**

---

**Wright-Patterson Air Force Base, Ohio**

APPROVED FOR PUBLIC RELEASE; DISTRIBUTION UNLIMITED

The views expressed in this thesis are those of the author and do not reflect the official policy or position of the United States Air Force, Department of Defense, or the United States Government.

AFIT/GAP/ENP/06-20

**CHARACTERIZATION OF DETONATION PHENOMENA OBSERVED IN  
HIGH-SPEED, VISIBLE IMAGERY**

THESIS

Presented to the Faculty

Department of Engineering Physics

Graduate School of Engineering and Management

Air Force Institute of Technology

Air University

Air Education and Training Command

In Partial Fulfillment of the Requirements for the

Degree of Master of Science (Applied Physics)

Trevor W. Warren, BS

First Lieutenant, USAF

March 2006

APPROVED FOR PUBLIC RELEASE; DISTRIBUTION UNLIMITED

AFIT/GAP/ENP/06-20

**CHARACTERIZATION OF DETONATION PHENOMENA OBSERVED IN  
HIGH-SPEED, VISIBLE IMAGERY**

Trevor W. Warren, BS  
First Lieutenant, USAF

Approved:

---

Glen P. Perram, (Chairman)

---

date

---

Ronald F. Tuttle, (Member)

---

date

---

Ralph A. Anthenien Jr. (Member)

---

date

---

David W. Gerts, (Member)

---

date

### **Abstract**

Measurements for radius, angular velocity, initial time of observation, and final time of observation were made for turbulent vortices around detonation fireballs. A proxy for vortex power, determined through unit analysis, was found to correlate well to initial (and final) time of observation with  $R^2$  equal to 0.8572. The linear trend on a  $\log_{10}$ - $\log_{10}$  plot was indicative of a rapid decrease (over  $10^{-1}$  s) in power associated with the decay of the fireball. Predictions, based on turbulent spectral theory were made for root-mean-square velocity fluctuations and Reynolds numbers, both as functions of time. In addition, reflected shock speeds inside the fireball were found to be, on average, 69% higher than those of the un-reflected shock outside. This difference in speed was used to estimate the adiabatic exponent inside the fireball. Values of the adiabatic exponent were found to range between 1.08 and 1.3, while exhibiting a decreasing trend in time, and a weak quadratic dependence on time. Lastly, comparisons of the primary and secondary shock velocities showed that the secondary shock was faster in six out of ten events. For two events, the speeds were equal to within the uncertainty of the measurements. The speed of the secondary shock varied from 1.8% to 30% faster than the primary shock.

## **Acknowledgments**

I would like to express my sincere appreciation to my faculty advisor, Dr. Glen Perram, for his guidance through the course of this endeavor, which would not have been possible in the absence of his tremendous foresight and experience. I would also like to express my gratitude to my committee members, Dr. Ronald Tuttle, Dr. Ralph Anthenien, and Major David Gerts for their selfless expenditure of time and effort necessary to bring this work to completion. I owe great thanks to NASIC, ATK Mission Research, AFRL, the 46<sup>th</sup> Test Wing, and TPL Inc, whose contributions of data provided the foundation for this research; and likewise to Marken Houle and Greg Smith for their superb test management. I would also like to thank my lab partners: Bryan Steward, Kevin Gross, and Carl Druffner for their generous contributions of time and assistance.

Trevor W. Warren

## Table of Contents

	Page
Abstract.....	iv
Acknowledgments.....	v
List of Figures.....	viii
List of Tables .....	xiii
1. Introduction.....	1
1.1 Relevance .....	1
1.2 Background.....	3
1.3 Theory.....	5
1.3.1 Chapman-Jouguet (CJ) theory .....	5
1.3.2 Shocks.....	8
1.3.3 Turbulence and vorticity.....	11
2. Experimental Setup.....	16
2.1 Instrumentation.....	16
2.2 Field Tests .....	22
2.2.1 Bronze Scorpio (Yuma).....	22
2.2.2 Northern Lights II (NL2).....	24
2.2.3 Dual Thrust Smokey SAM (DTSS).....	25
2.2.4 TPL muzzle flash.....	27
3. Data Analysis and Characterization.....	30
3.1 Methodology.....	30
3.1.1 Phantom Software Processing .....	30
3.1.2 MATLAB processing .....	32
3.1.3 Measurement difficulties and quantification of uncertainty .....	33
3.2 Characterization of Phenomena.....	36
3.2.1 Vortices.....	36
3.2.2 Reflected shocks, secondary detonations, secondary shocks, and opacity.....	49
4. Discussion .....	64
4.1 Vortices.....	64
4.1.1 Further speculation .....	66
4.2 Reflected and secondary shocks, and secondary detonations .....	71
4.3 Spectral analysis .....	79

5. Conclusions and Recommendations .....	83
5.1 Vortices.....	84
5.2 Reflected Shocks .....	86
5.3 Secondary detonations and secondary shocks.....	87
5.4 Recommendations .....	89
Appendix A-1: Phantom Camera Data .....	92
Appendix A-2: Bronze Scorpio Data.....	94
Appendix A-3: NL2 Data.....	95
Appendix A-4: DTSS data .....	97
Appendix A-5: Muzzle Flash data .....	98
Bibliography .....	101



## List of Figures

Figure	Page
1. Phantom high-speed, digital imager. ....	16
2. Example of a residual (latent) image. Initial images of cartridge silhouette in frame 339 (left), and a subsequent image in frame 349 (right). The camera was framing at 200 pps. Settings for contrast, gamma, and brightness are the same for both images and have been modified to enhance the silhouette. ....	19
3. M760 105 mm Cartridge (left), M107 155 mm Comp-B (center), and TNT Cartridge (left). ....	23
4. View of the target area from the Phantom camera. The suspended charge is centered in the white circle. ....	25
5. Location of Smokey SAM test stand, WPAFB area B ....	26
6. Test stand with rocket un-ignited (top) and ignited (bottom) ....	26
7. The instrument arrangement for TPL muzzle flash tests. The Phantom camera is at the approximate center of the image (left ellipse). The test pistol is slightly below and to the right (right ellipse).....	28
8. Muzzle flash captured by Phantom. The cumulative gray and white region constitutes the gun barrel opening. ....	29
9. Comparative plots for data distributions using linear and log scales. Data for $t_a$ (upper left), $\text{Log}_{10} t_a$ (upper right), $\omega$ (lower left), and $\text{Log}_{10} \omega$ (lower right) was plotted against itself to illustrate its distribution in one dimension. ....	38
10. $\text{Log}_{10}$ - $\text{Log}_{10}$ Relationship between angular speed and appearance time for the entire set of vortex data. The regression line is determined by $\text{Log } \omega = -0.8661 \text{ Log } t_a + 0.5989$ , with $R^2 = 0.7648$ . ....	40
11. $\text{Log}_{10}$ - $\text{Log}_{10}$ Relationship between angular speed and disappearance time. The regression line is determined by $\text{Log } t_d = -0.8793 \text{ Log } \omega + 0.3875$ , with $R^2 = 0.8032$ .....	41
12. Relationship between time of disappearance and angular speed of a vortex on a linear scale.....	41

Figure	Page
13. Relationship between angular speed of a vortex and its time of appearance on a linear scale. The regression curve is a power law given by $\omega = 624031 t_a^{-0.8661}$ , with $R^2 = 0.7648$ .....	42
14. Log <sub>10</sub> -Log <sub>10</sub> relationship between the angular speed of a vortex and the duration for which it was observed. The regression line is determined by $\text{Log } \Delta t = -0.8849 \text{ Log } \omega + 0.0316$ , with $R^2 = 0.7259$ .....	42
15. Linear relationship between duration of a vortex and its time of appearance. The regression line is determined by $\Delta t = -0.6316 t_a + 7120$ , with $R^2 = 0.5693$ . ....	43
16. Linear relationship between duration of a vortex and its time of disappearance. The regression line is determined by $t_d = -1.9013 \Delta t + 0.6952$ , with $R^2 = 0.8547$ . ....	44
17. Log <sub>10</sub> -Log <sub>10</sub> relationship between vortex duration and energy. The regression line is determined by $\text{Log } \Delta t = -0.4152 \text{ Log } E - 0.4954$ , with $R^2 = 0.5769$ .....	44
18. Log <sub>10</sub> -Log <sub>10</sub> relationship between pressure and vortex duration. The regression line is determined by $\text{Log } \Delta t = -0.4243 \text{ Log } p + 0.1626$ , with $R^2 = 0.7496$ . ....	45
19. Log <sub>10</sub> -Log <sub>10</sub> relationship between pressure and appearance time. The regression line is determined by $\text{Log } p = -1.7627 \text{ Log } t_a + 1.6357$ , with $R^2 = 0.7056$ . ....	46
20. Energy of a vortex versus time of vortex appearance. The regression line is determined by $\text{Log } E = -1.6709 \text{ Log } t_a + 0.322$ with $R^2 = 0.7889$ .....	47
21. Power of a vortex versus time of vortex appearance using (33a). The regression line is given by $\text{Log } W = -2.5416 \text{ Log } t_a + 0.6321$ with $R^2 = 0.8572$ . ....	47
22. Comparative plots detailing correlations for incomplete parts of the power parameter with appearance time. Beginning at the upper left and moving from left to right: 1) $\omega^2/\Delta t$ versus $t_a$ , $R^2 = 0.8016$ ; 2) $\omega^2 r^2$ versus $t_a$ , $R^2 = 0.7889$ ; 3) $r^2/\Delta t$ versus $t_a$ , $R^2 = 0.7194$ ; 4) $r$ versus $t_a$ , $R^2 = 0.0097$ . Abcissae and ordinates are on a Log <sub>10</sub> scale in all four plots, with $t_a$ and $\Delta t$ given in $\mu\text{s}$ . ....	49

23. Progression of a shock reflection in NL2 event 2 through several (non-successive) images: 1) interaction with ground (upper left); 2) formation of dome-shaped reflection (upper right); 3) propagation of reflection (bright band) through fireball column (lower left); 4) continued propagation through fireball column (lower right). The cross-shaped fireball is due to the cylindrical geometry of the charge. Also note the primary shock at the top of the fireball in the lower two images. Gamma has been adjusted to enhance each image. .... 51
24. Sequential images of a secondary detonation in NL2 event 3, beginning in the upper left and moving from left to right. The detonation appears to be initiated when the reflected shock (bright band in the first image) reaches the approximate center of the fireball, where the primary detonation originated. The expansion of the bright region is much faster than the primary or reflected shocks. Images have not been modified. .... 54
25. Primary and secondary shocks for NL2 event 3. The positions of the shocks along the horizon are visible due to the change in the index of refraction. The primary shock (right circle) lies outside the span of the two vertical poles, while the secondary shock (left circle) lies within. Contrast and Gamma have been modified to enhance the image..... 56
26. Motion of refractive index disturbance along the horizon for the leftward propagation of the primary shock in NL2 event 2. The regression line follows the relation  $x = -0.0621 f - 997.24$ , with  $R^2 = 0.9824$ . The slope of the regression line is the velocity of the disturbance in meters per frame. The negative sign indicates that the frames were captured prior to trigger (a manual post-event trigger was utilized)..... 58
27. Motion of refractive index disturbance along the horizon for the leftward propagation of the secondary shock in NL2 event 2. The regression line follows the relation  $x = -0.0641 f - 1025.1$ , with  $R^2 = 0.9992$ . The slope of the regression line is the velocity of the disturbance in meters per frame. .... 58
28. NL2 event 3. Before-detonation (left) and during-detonation (right) spliced images showing the suspended explosive charge (centered in the white circle) still visible in the center of the fireball after the primary detonation has occurred. The images have not otherwise been altered. .... 60

Figure	Page
29. Scatter plot of the mean red value of each event versus the standard deviation of the red values for each event. Values are derived from an 8-bit (0-255) color scale. Symbols are defined according to the legend in the upper right, where <i>con</i> stands for conventional, <i>fran</i> for frangible, <i>nov</i> for novel, and <i>fmj</i> for full metal jacket. ....	61
30. Comparison of the flashes created by two separate conventional rounds. ....	62
31. Same as Figure 29 but for green. ....	62
32. Same as Figure 29 but for blue. ....	63
33. Scatter plot of diameter and time of initial observation. A weak trend toward increasing vortex dimensions is evident but the data is highly uncorrelated, with $R^2 = 0.0547$ . ....	65
34. Top: $\text{Log}_{10}$ - $\text{Log}_{10}$ relationship between $u'_{rms}$ and time of vortex appearance computed using the distributed power $W$ . The regression line is given by $\text{Log } u'_{rms} = -0.837 \text{Log } t_a + 0.0647$ , with $R^2 = 0.8559$ . Bottom: $\text{Log}_{10}$ - $\text{Log}_{10}$ relationship between $u'_{rms}$ and time of vortex appearance computed using instantaneous power $Y$ . The regression line is given by $\text{Log } u'_{rms} = -0.8355 \text{Log } t_a + 0.462$ , with $R^2 = 0.7889$ . ....	68
35. Top: $\text{Log}_{10}$ - $\text{Log}_{10}$ relationship between Reynolds number and time calculated using equation 36. The regression line is given by $\text{Log } Re = -2.2362 \text{Log } t_a + 2.1864$ , with $R^2 = 0.8579$ . Bottom: $\text{Log}_{10}$ - $\text{Log}_{10}$ relationship between Reynolds number and time calculated using equation 36b. The regression line is given by $\text{Log } Re = -0.8049 \text{Log } t_a + 4.5455$ , with $R^2 = 0.6601$ ....	70
36. Correlation between $\gamma$ and time of measurement. The regression curve is determined by $\gamma = 0.002 t_m^2 - 0.045 t_m + 1.3534$ with $R^2 = 0.2916$ . ....	75
37. Top: Removal of one outlying data point at (6,1.3) from the original data shown in fig. 36 permits the new quadratic fit $\gamma = 0.0029 t_m^2 - 0.0571 t_m + 1.382$ , and $R^2 = 0.4953$ . Bottom: omission of a second outlying point at approximately (12,1.1) permits the cubic fit $\gamma = 0.0033 t_m^3 - 0.05 t_m^2 + 0.2061 t_m + 0.9755$ and $R^2 = 0.8198$ . ....	76
38. Plots of the ratios of mean and standard deviations of different colors as a function of frame number for Yuma event 46. R, G, and B refer to red, green, and blue respectively. ....	79

Figure	Page
39. Plots of : 1)the coefficients of variation for red R, green G, and blue B (first row); 2) the differences of the coefficients for each unique combination of colors (second row), and 3) the three unique ratios of these differences (third row). The abscissae are in frame number. Plots are all generated from NL2 event 3.....	80
40. Plots for Yuma event 3. Parameters of each plot are the same as figure 39. Note the similarity, between the two events, in the magnitudes of the values and in the respective behavior of the three colors, such that $R > G > B$ . ....	81

## List of Tables

Table	Page
1. Table 1. Geodetic data for Bronze Scorpio test. ....	22
2. Table 2. Statistics for vortex data. Appearance time refers to the initial observation of a vortex relative to event initiation at time $t=0$ . Disappearance time refers to the final observation of a vortex relative to event initiation at time $t=0$ . Duration refers to the longevity of observation of a vortex. ....	37
3. Table 3. Statistics for vortex data using log scales .....	37
4. Table 4. Measurement uncertainty statistics .....	39
5. Table 5. Summary of reflected shock data. Reported times and speeds are not necessarily associated. ....	50
6. Table 6. Simultaneous velocities and uncertainties for the primary and reflected shocks. The far-left column gives the difference of the minimum value of the reflected shock and the maximum value of the primary shock, as determined by the respective subtraction or addition of the associated uncertainty.....	52
7. Table 7. Summary of secondary detonation data. Reported times and speeds are not necessarily associated .....	53
8. Table 8. Complete set of measurements taken for secondary detonations. All events were part of the NL2 test. ....	53
9. Table 9. Speeds of the primary and secondary shock, speed differences between the primary and secondary shock, and uncertainties. All events were part of NL2. A negative sign in the second-to-last column indicates that the velocity difference between the two shocks is within the uncertainty in the velocity of the primary shock. ....	59
10. Table 10. Values of $\gamma$ for their respective events and times. $\gamma^-$ is taken to be the physically meaningful solution. The mean value of $\gamma^-$ is approximately 1.16 with a standard deviation of 0.06 over the 15 data points. ....	74

# **CHARACTERIZATION OF DETONATION PHENOMENA OBSERVED IN HIGH-SPEED, VISIBLE IMAGERY**

## **1. Introduction**

### **1.1 Relevance**

The threats of global terrorism and widespread instability throughout the world in recent years have necessitated the continued advancement of remote sensing capabilities. Essential among these capabilities is the capacity to accurately detect and identify the source of rapid exothermic reactions (i.e. detonations and deflagrations) in a timely and cost-effective manner. At a minimum, one must be able to derive the chemical composition, size, and packaging (if applicable) of a given explosive or combustible from remote sensing data for the purpose of making a valid identification. Such identification is contingent upon the development of reliable signatures. The extraction of statistically distinctive features from large data sets is the most logical course to signature creation. However, although the approach is simple, the problem is multifaceted, and not wholly understood. At this time, a limited understanding largely precludes any certainty of key feature relevance. It is therefore necessary to engage in a trial-and-error process to isolate key features that serve as faithful discriminators. One step toward this end is an accurate survey and characterization of physical phenomena observed in visible regions of the spectrum. As in the infrared, most energetic chemical events of interest are very active at

visible wavelengths, with the added benefit of spectrally independent, atmospheric transmission near unity.

Several features have been explored to ascertain their reliability for service as discriminators. Among these is the temporal profile of an event as a function of frequency (2). This approach involves representing an event as a set of frequency-dependent vectors whose component (basis) vectors are the set of time intervals over which the event was recorded, scaled by the radiance values at a particular frequency during each time interval. When these vectors are normalized and dotted with normalized vectors of equivalent frequency from another event, a temporal overlap is produced. The temporal overlap may be interpreted as the cosine of the angle between the vectors of equivalent frequency. The value of the cosine function ranges from one to zero, where one indicates the profiles are identical and zero indicates the profiles are orthogonal. Perhaps even more promising, and particularly useful for detonation events, is the relationship between temperature and fireball size. This approach attempts to measure the fireball's deviation from a Planckian graybody. Non-Planckian behavior is most apparent when the fireball is small and hot, immediately following detonation; this is consistent with what one would expect for a body that is not in thermal equilibrium (2). A third feature currently under consideration is the area of a fireball as a function of time, which has shown promise as a discriminator sans the issue of flame obscuration by dust and debris (2). It has been consistently observed that the area of a fireball will grow and then shrink rapidly, then undergo a slower growth phase followed by a comparably slow shrinking phase. Structure in this general pattern may be dependent on explosive type.



These analyses, thus far, have taken place in the near IR (NIR) and mid-wave IR (MWIR) spectral regions, and at temporal sampling approximately on par with that of human vision (30 Hz). Due to the nature of the instrumentation, which collected the data, the previous analyses have neglected both the visible regions of the spectrum and very short time-scales (on the order of microseconds), where a wealth of phenomenology is present. This phenomenology includes secondary detonations, secondary and reflected shockwaves and flame regions that are occasionally optically thin in the visible.

Turbulence and vorticity provide insights into the mechanical and chemical behavior of the fireball. Development of this understanding could lead to enhanced knowledge of the fireball's deflagration and also provide a means for corroborating spectral measurements of temperature or other physical quantities. Secondary and reflected shocks are important because they contain information about the transient thermodynamic properties of the fireball. Since the intuitive assumption has been that flame regions are always optically thick, optically thin flame regions have the potential to alter previous interpretations of spectra. Spectral classification techniques are being explored in the IR and show a great deal of promise. Answering key questions about the optical thickness of fireball flame regions and whether spectra are taken from inside the fireball or from its surface will enhance this approach.

## **1.2 Background**

This research focuses primarily on the mechanical nature of the fireball through the investigation of turbulence and shocks. Secondary efforts have been made to derive rudimentary spectral information from the visible, three-band Phantom camera and assess

reproducibility of energetic chemical events in visible wavebands through controlled muzzle-flash tests.

It is suspected that turbulence and vorticity arise in fireballs as a result of rapid expansion of gasses, which produces a high velocity flow-field in the region of the detonation. These turbulent motions may play a role in fireball boundary deflagration. On their own, turbulence and vorticity are well studied problems in fluid mechanics but their characterization in terms of energetic, transient phenomena is not thorough. A good deal of work has been performed on modeling of simple combustion-flow problems, which apply to turbulent mixing of fuel and oxidizer. Among these are the simulations of Kagan and Sivashinsky on non-adiabatic, premixed combustion in large-scale, vortical flows (11), and the effect of Lewis number on flame propagation through vortical flows (10). Turbulent convection due to internal heat generation in a cavity has been modeled by Horvat et al (9), and is applicable to the convective actions accompanying the large temperature gradients. The spatial and temporal distribution of turbulence induced by a coaxial jet mixer has been modeled by Hassel et al (8) and a similar analysis was performed for a jet of falling particles by Uchiyama and Naruse (18), both of which provide insight into understanding a fireball's turbulent energy spectrum. None of these alone, however, approach the complexity and diversity of phenomena associated with a detonation event, and, therefore, they can not simply be superposed into a complete understanding of the problem.

In addition to turbulence, shockwaves are an intrinsic mechanical underpinning of detonation events. They are also easy to measure directly and provide fundamental

information about the initial conditions associated with a fireball. Shockwaves have been studied more thoroughly than turbulence, in the context of detonations. Much of the foundation for the current understanding of shockwaves comes from Zel'dovich and Raizer (20). A shockwave develops when a detonation wave reaches the boundary of a detonation medium and makes contact with an inert surrounding medium (air in this case). Rapid expansion of the explosive material induces a sudden spatial change in the local fluid. The energy associated with this change is deposited in the fluid and travels as a shockwave. The exact nature of the energy deposition is contingent on the geometry of the explosive charge, the casing material, and the intrinsic properties of the condensed explosive (19); these determine the speed of the shock and may be derived through Chapman-Jouguet (CJ) theory. Shockwaves are particularly interesting because their propagation is highly dependent on thermodynamic properties of the propagation medium (20). Given that shocks have been observed to reflect and propagate back through the evolving fireball, their utility in regards to thermodynamic quantification should not be neglected; likewise for secondary detonations and their associated shocks.

### **1.3 Theory**

Explanations of the observed phenomena are contingent on basic theoretical formulations of detonations, shocks, turbulence, and vorticity.

#### **1.3.1 Chapman-Jouguet (CJ) theory**

Detonation is the propagation of chemical combustion by means of energy transfer through compression waves; it differs from other forms of combustion in the negligible contributions of heat flow (5:16). The physics of detonation is most simply

described through CJ theory. Applicable assumptions include: 1) a one dimensional (laminar) flow; 2) a detonation front described by a jump discontinuity with emergent material in thermodynamic equilibrium; and 3) a time-independent discontinuity resulting in a time-independent state of emergent material (5:16) Conservation of mass, momentum, and energy are given, respectively in equations 1, 2 and 3 as

$$\rho_0 D = \rho(D - u), \quad (1)$$

$$p - p_0 = \rho_0 u D, \quad (2)$$

$$E(p, v, \lambda = 1) + pv + 1/2(D - u)^2 = E(p_0, v_0, \lambda = 0) + p_0 v_0 + 1/2 D^2, \quad (3)$$

where  $D$  is the velocity of the detonation front,  $u$  is the velocity of the detonation products,  $p$  is the pressure,  $\rho$  is the density of the explosive material, and  $E$  is the chemical energy liberated in the explosion.  $\lambda$  represents the progress of the chemical reaction, which at  $\lambda = 0$  is uninitiated and at  $\lambda = 1$  is complete. The subscript “0” denotes the initial state. Eliminating  $u$  from equations (1) and (2) gives the “Rayleigh line” (17:17), expressed as

$$R = \rho_0^2 D^2 - (p - p_0)/(v_0 - v) = 0, \quad (4)$$

with  $v = \rho^{-1}$  denoting the specific volume. The slope of the Rayleigh line is then  $\rho_0^2 D^2$ , and is clearly constrained to lie between 0 (horizontal) and  $\infty$  (vertical) (5:17).

Elimination of  $u$  and  $D$  from equation (4) is possible using equations (1) and (2), which defines the Hugoniot curve  $RH$  in the  $p$ - $v$  plane as (5:17)

$$RH = E(p, v, \lambda = 1) - E(p_0, v_0, \lambda = 0) - 1/2(p + p_0)(v_0 - v) = 0 \quad (5)$$

An equation of state is required to close this system and determine the set of possible final values of  $p$  and  $v$  for a given  $p_0, v_0, D$ , and complete heat of reaction  $q = -\Delta H = \Delta E(\lambda)$  (5:17). Assuming an ideal gas with constant heat capacity, the Hugoniot curve becomes

$$\left( \frac{p}{p_0} + \mu^2 \right) \left( \frac{v}{v_0} - \mu^2 \right) = 1 - \mu^4 + 2\mu^2 \frac{q}{p_0 v_0} \quad (6)$$

with

$$\mu^2 = (\gamma - 1) / (\gamma + 1) \quad (7)$$

where  $\gamma$ , the adiabatic exponent, is equal to 1.4 for air at room temperature and about 1.28 for heated air in the vicinity of combustion (5:18). The conservation laws dictate that the final values of  $p$  and  $v$  satisfy both equations (4) and (6), when  $p$  and  $v$  are related by the ideal gas equation of state (5:18). This constrains the state pair  $(p, v)$  to lie on an intersection of the Hugoniot curve and the Rayleigh line. The location of an intersection determines the relative magnitudes of  $D$  and  $u$ . Under the special circumstance that the Rayleigh line is tangent to the Hugoniot curve, the difference between  $D$  and  $u$  is the speed of sound,  $c$ , in the product medium (5:19). This is known as the CJ point and  $D$  follows as the CJ velocity. Cases with two intersections have an upper, “strong” solution where  $D - u < c$  and a lower, “weak” solution where  $D - u > c$ . When the value of  $D$  precludes intersection, the system can not support a stable detonation (5:19).

The Zel’dovich-Von Neumann-Doering (ZND) model augments CJ theory with the additional assumption of finite reaction rate behind the shock front (5:42). This generalizes the Hugoniot curve (1.6) to include the reaction parameter  $\lambda$ , giving

$$\left( \frac{p}{p_0} + \mu^2 \right) \left( \frac{v}{v_0} - \mu^2 \right) = 1 - \mu^4 + 2\mu^2 \frac{\lambda q}{p_0 v_0} \quad (8)$$

A chemical rate law is now required for closure of the ZND system. When sufficient information is considered, the intersections of the Hugoniot curve and the Rayleigh line acquire a spatial or temporal dependence but can still be modeled as a traveling wave.

### 1.3.2 Shocks

Rapid displacement of the atmosphere, following the emergence of the reaction wave from the reaction medium, establishes a shock front that initially propagates at speed  $C$ . This shock front is idealized to a mathematical (though physically unrealizable) discontinuity in pressure, temperature, and density. Here, it becomes convenient to change reference frame, considering the shock to be stationary and the fluid to be in motion. Prior to reaching the discontinuity, the fluid flows with pressure  $p$ , density  $\rho$ , and velocity  $u(=-C)$ ; it then emerges behind the discontinuity with pressure  $p'$ , density  $\rho'$ , and velocity  $u'$ . These six variables are linked by the Rankine-Hugoniot (RH) relations for shock propagation in an ideal gas (4:102). Treatment of shocks becomes more manageable when the velocities  $u$  and  $u'$  are replaced with their respective Mach numbers such that  $M = u/c_s$  and  $M' = u'/c_s'$  where  $c_s$  and  $c_s'$  are the speeds of sound on their respective sides of the shock front. The first of the RH relations (4:102) posits the validity of Bernoulli's theorem in terms of the enthalpy change across the shock, giving:

$$\frac{p}{\rho} \left( 1 + \frac{1}{2}(\gamma - 1)M^2 \right) = \frac{p'}{\rho'} \left( 1 + \frac{1}{2}(\gamma - 1)M'^2 \right) \quad (9)$$

The second RH relation establishes the continuity condition for conservation of mass, written in terms of the Mach numbers as

$$p\rho M^2 = p'\rho' M'^2 \quad (10)$$

The last of the RH relations (4:103) establishes conservation of momentum, returning

$$p(1 + \gamma M^2) = p'(1 + \gamma M'^2) \quad (11)$$

Upon manipulation of these relations (4:103), it becomes evident that the Mach numbers are uniquely determined by the dimensionless parameter  $\sigma$ , whereby

$$M^2 = 1 + \frac{(\gamma + 1)}{2\gamma} \sigma \quad (12)$$

$$M'^2 = 1 - \frac{(\gamma + 1)}{2\gamma} \frac{\sigma}{(1 + \sigma)} \quad (13)$$

with

$$\sigma = \frac{(p' - p)}{p} \quad (14)$$

Taking  $p' > p$  forces the condition that the flow in the low-pressure  $p$  region be supersonic relative to the shock, while that in the high-pressure  $p'$  region be subsonic (4:103). Both Mach numbers approach unity as  $\sigma$  tends toward zero and when  $\sigma$  is finite but small, terms in  $\sigma$  higher than first order may be neglected, giving

$$u = Mc_s \approx c_s \left( 1 + \frac{(\gamma + 1)}{4\gamma} \sigma \right), \quad (15)$$

which is, of course, equal to the negative of the shock propagation speed  $-C$  (4:104).

However, for strong shocks, this becomes

$$C \approx c_s \sqrt{\frac{(\gamma + 1)p'}{2\gamma p}} = \sqrt{\frac{(\gamma + 1)p'}{2\rho}} \quad (4:104). \quad (16)$$

The previous treatment, though applicable at early times of shock propagation, is subject to the assumption that the discontinuity and its velocity  $C$  are constant. In reality, as one would suspect, such is not the case, and  $C$  must inevitably decrease while  $\sigma$

weakens with time (20:100). In many ways, the shock, once free of the detonation medium, is analogous to a ballistic projectile, whose trajectory depends only by the impulse that initiated its motion. Nevertheless, over brief intervals,  $C$  and  $\sigma$  may be assumed to remain approximately constant.

Further development of the explosion-induced, strong shock phenomenon may be accomplished subject to the assumptions that the propagation medium is a perfect gas and that the energy release of the explosion occurs nearly instantaneously, at a single point (20:93). It is also assumed that the shock is still close enough to the source that  $p' \gg p$  is valid, making  $\sigma$  large (20:93). Dimensional analysis returns (20:94), in terms of the liberated energy  $V$ , the position  $x$ , and the time  $t$ , the non-dimensional quantity

$$\zeta \equiv x \left( \frac{\rho}{V t^2} \right)^{1/5} \quad (17)$$

The concurrent inclusion of both position and time satisfies the condition for self similar motion such that the distributions of the flow variables with respect to the coordinate variable always remain similar in time (20:93). Algebraic manipulation of equation (17) provides, in terms of the independent variable  $\zeta_0$ , the shock radius  $X$  as a function of time, whence

$$X(t) = \zeta_0 \left( \frac{V}{\rho} \right)^{1/5} t^{2/5}, \quad (18)$$

given that the strong shock condition is satisfied (20:94). It follows that the propagation velocity (20:94), equivalent to equation (16), is then

$$C = \frac{dX}{dt} = \frac{2}{5} \frac{X}{t} = \zeta_0 \frac{2}{5} \left( \frac{V}{\rho} \right)^{1/5} t^{-3/5} = \frac{2}{5} \zeta_0^{5/2} \left( \frac{V}{\rho} \right)^{1/2} X^{-3/2} \quad (19)$$



Parameters behind the shock may be quantified according to their limiting values. Thus, equations (20), (21), and (22) give the values of density, pressure and velocity (20:94), respectively as

$$\rho' = \rho \frac{\gamma+1}{\gamma-1}, \quad (20)$$

$$p' = \frac{2}{\gamma+1} \rho C^2, \quad (21)$$

$$u' = \frac{2}{\gamma+1} C \quad (22)$$

While the density remains constant, the pressure acquires a temporal dependence (20:94) given by

$$p' \sim \rho C^2 \sim \rho \left( \frac{V}{\rho} \right)^{2/5} \sim t^{-6/5} \sim \frac{V}{X^3} \quad (23)$$

Self similarity also permits the derivations of distributions for density, temperature, pressure, and velocity, as a function of the linear coordinate  $x$ . The equation for pressure behind a planar shockwave is given below as

$$P(x/X) = \frac{1}{2} (p' - p) \tanh \left( \frac{x}{\delta} \right) + \frac{1}{2} (p' + p), \quad (24)$$

where it can be shown that  $\delta$  is approximately equal to the mean free path of a gas particle (12:340).

### 1.3.3 Turbulence and vorticity

Turbulent fluid flow is characterized by random variations in the velocity of a fluid element; fluctuations in both space and time are rapid and irregular (17:16). Transition

from laminar or smooth, predictable flow to turbulence is governed by the Reynolds number,  $Re$ , defined as

$$Re = \frac{uL}{\nu} \quad (25)$$

where  $u$  is the fluid velocity,  $\nu$  is the kinematic viscosity, and  $L$  is a characteristic length-scale of the system. Transition to turbulence usually occurs with Reynolds numbers on the order of  $10^3$  (17:19). As a result of high shear rates in turbulent flows, fluid elements will acquire a vorticity  $\omega$ , which is representative of a fluid elements' differential rotation at a particular point, given by

$$\omega = \nabla \times \vec{u}, \quad (26)$$

where  $u$  is the local flow velocity. When the vorticity is distributed, local streamlines may become convoluted, bending backward and eventually closing on themselves.

Application of Stokes's theorem to bounded surfaces containing non-zero, net vorticity results in bulk fluid circulations or eddies (the terms “eddy” and “vortex” are henceforth used interchangeably) (17:83). One may obtain the equation for conservation of vorticity by distributing the curl operation through the Navier-Stokes equation (17:86).

It is often convenient to analyze turbulence in terms of its component velocities, whence decomposition results in a spectrum. The spectrum may be defined in numerous ways; but commonly it is taken to be the energy present at a given frequency of velocity oscillation. However, when thinking in terms of the spatial structure of vorticity and distributions of eddies, it is more advantageous to formulate a spatially-dependent spectrum, despite the complications incurred by the additional dimensionality. This is most readily done using wavenumber (17:310).

The division of turbulent motion into interacting motions on various length scales is often expressed by referring to ‘eddies of different sizes’ (17:310). Due to their distinctive characteristics with respect to the flow field, large eddies may be termed ‘coherent structures.’ Although eddies are localized in the flow, they contribute to wavenumber components of the turbulent spectrum according to their size and are, therefore, directly (if loosely) related to a length-scale dependent energy distribution (17:311).

The utility of spectral analysis becomes apparent through consideration of homogeneous, isotropic turbulence. Turbulence of this nature is generated experimentally by placing a grid or mesh perpendicular to a laminar flow field. In the case of homogeneous, isotropic turbulence, one may write

$$\frac{\partial E(k,t)}{\partial t} = F(k,t) - 2\nu k^2 E(k,t) \quad (27)$$

where  $E$  is the energy spectrum and  $k$  is the wavenumber (17:314). This is a statement relating the rate of change in the energy at a given wavenumber (left-hand side) to the difference in the rates of energy transfer between wavenumbers  $F$  (first right-hand term) and the rate of viscous dissipation (second right-hand term). Conservation of energy requires that

$$\int_0^{\infty} F dk = 0, \quad (28)$$

when dissipation is the only means of energy outflow (17:315). The quadratic dependence of this dissipation on  $k$  in equation (27) implies that more kinetic energy is lost to fluidic heating at larger wavenumbers (smaller length scales), which is a

consequence of the high Reynolds numbers associated with turbulent flows. This may be interpreted as the minimization of the influence of viscosity at the length-scale of the mean flow (taken to be the mesh separation distance) (17:317). However, the addition of turbulent energy occurs most readily at the mean flow length-scale and, therefore, is fed first into the largest eddies. In order that dissipation balance influx and satisfy equation (27), energy must be transferred to the small scale dissipative eddies. This occurs through a cascade of eddies, such that eddies at a particular scale are driven by larger eddies up to the mean flow scale. The energy transfer is the source of the wavenumber spectral distribution subject to equation (28).

Due to the requisite energy balance, the dissipation is only dependent on the rate at which energy is supplied and is thus independent of the dynamics of the small eddies where it occurs; it is then, necessarily, independent of the magnitude of the viscosity as well (17:317). A decrease in viscosity, corresponding to an increase in Reynolds number, only changes the scale of the smallest dissipative eddies. Effectively, the spectrum becomes stretched at the large wavenumber end (17:317). Given that energy addition occurs at small wave numbers and outflow occurs at large wavenumbers, if the spectrum is broad enough, there exists a range of intermediate wavenumbers independent of production and viscosity, such that

$$E = E(k, \varepsilon_0), \quad (29)$$

where  $\varepsilon_0$  is the rate at which energy is added to the system.  $E(k)dk$  is then the mean kinetic energy per unit mass, which is stored in the range of wavenumbers between  $k$  and

$k + dk$  (18:355).  $E$  and  $\varepsilon_0$  have dimensions of  $[L]^3[T]^{-2}$  and  $[L]^2[T]^{-3}$ , respectively, making  $\varepsilon_0^2/(k^5 E^3)$  a dimensionless combination, from which may be derived

$$E \sim \varepsilon_0^{2/3} k^{-5/3} \quad (30)$$

This relation is known as the Kolmogorov -5/3 power law (17:355). In the intermediate wavenumber range, also called the inertial subrange, where dissipation is negligible,  $\varepsilon_0$  is approximately equal to  $F (= \varepsilon)$  in equation (27). However, experimental evidence suggests that  $\varepsilon$  has a wavenumber dependence, especially at higher wavenumbers (17:318).

## 2. Experimental Setup

### 2.1 Instrumentation

All data were recorded with the Phantom version 7.1 high speed digital imager. The Phantom instrument, patented by Vision Research, houses a complete system consisting of 1) a CMOS sensor; 2) a processor; 3) an internal operating system; 4) sufficient memory to store the image information captured from the sensor; and 5) an interface system that allows for data downloads, streaming video signaling, camera software control, and camera networking. The instrument is shown in Figure 1.



Figure 1. Phantom high-speed, digital imager.

The CMOS based focal plane array (FPA) provides an adjustable window (digital field stop) with a maximum size of 800 x 600 pixels. Maximum framing frequencies range from 1000 pictures per second (pps), when the FPA is fully enabled, to 150,000 pps with a 32 x 32 pixel (minimum) window. The FPA integrates over three color-bands in the visible spectrum to produce full color red-green-blue (RGB) images. RGB readouts are stored in a 24-bit color-space as three independent 8-bit values with digital numbers ranging from 0 to 255. CMOS sensors are immune to blooming as well as multi-panel

imaging artifacts attributed to many high-speed sensors (15). Exposure times, window sizes, and frame rates can be adjusted to accommodate a range of environmental or data-dependent conditions. The instrument can also be synchronized with external events and other Phantom imagers to an approximate precision of one microsecond.

While the sensor is producing images, analog-to-digital conversion and digital processing creates binary representations of those images (15). Images are stored internally or transmitted to an attached server as Cine (.cin) files. Stored images can then be processed, converted into other formats, and compressed using the instrument's native control software. The instrument's internal memory consists of 4 GB of SDRAM, which will store approximately 11,000 frames of data at maximum window. A quick reference for Phantom specifications is supplied in Appendix A-1

### **2.1.1 Trade-space limitations**

Acquisition of data is constrained to lie within the trade-space created by window size, frame-rate, exposure time, and available memory. Events that are highly transient require rapid framing, on the order of twice the highest frequency expected in the data (to meet the Nyquist criterion). Rapid framing, however, necessarily reduces the integration time and the amount of light that the FPA can use to form an image. Events that are both highly transient and dim may be un-acquirable at frame rates high enough to resolve them temporally. Events that are large, or that require a great deal of spatial resolution necessitate the use of larger window sizes. Limitations on FPA readout and memory writing restrict the amount of data that can be stored in a given time. Therefore, larger windows require slower framing. If events are also long relative to the desired temporal

resolution, they may saturate the camera's internal memory and their capture may be truncated. Camera software automatically restricts frame rates to meet memory requirements based on changes in window size, and also restricts exposure time based on frame rate. Adjustments within the automatically imposed limits may be made manually by the user. Typically, this becomes a trial and error process to maximize important parameters of collected data.

Most of the data, to be presented later, was collected well within the camera's trade-space envelope. The notable exception was the TPL muzzle flash data. It has been determined, contrary to expectations, that the muzzle flash events were near the instrument's detection threshold and it was thus necessary to minimize frame rate.

### **2.1.2 Image Latency**

During muzzle-flash tests, artifacts in the form of residual or latent images developed as a result of data acquisition near the limit of the instrument's detection threshold. Almost every capture consisted of one bright image succeeded by a series of faint images whose spatial distributions remained nearly identical to that of the first. The most notable occurrence was that of an ejected sabot caught between the camera and the flash such that the sabot silhouette was clearly visible in the image, depicted in Figure 2.

The identical pair of coordinates ( $x = 617$ ,  $y = 256$ ) in the lower right corner of each image are the coordinates for the topmost point of the cartridge silhouette. At 200 pps, displacement due to gravitational acceleration should be approximately 0.0125 meters or 47 pixels after ten frames, if the cartridge was at rest in the initial frame (frame 339). It is therefore necessary to conclude, in the absence of any expected motion, that



image 349 is a residual image of 339 and does not provide any unique data. This effect may be attributed to an incomplete readout of charge from the focal plane between frames. Remaining charge is then sufficient to generate a distinct latent signal, when true signal, background, and noise are minimal. Under these circumstances, real data is only identifiable by a change in the pattern of the flash between subsequent frames.

Fortunately, this low signal phenomenon has not been observed in, and is thus inconsequential for bright events, even at high framing speeds where charge readout should be less complete. Consideration of this artifact may be safely neglected in the analysis of all but the muzzle flash collections.

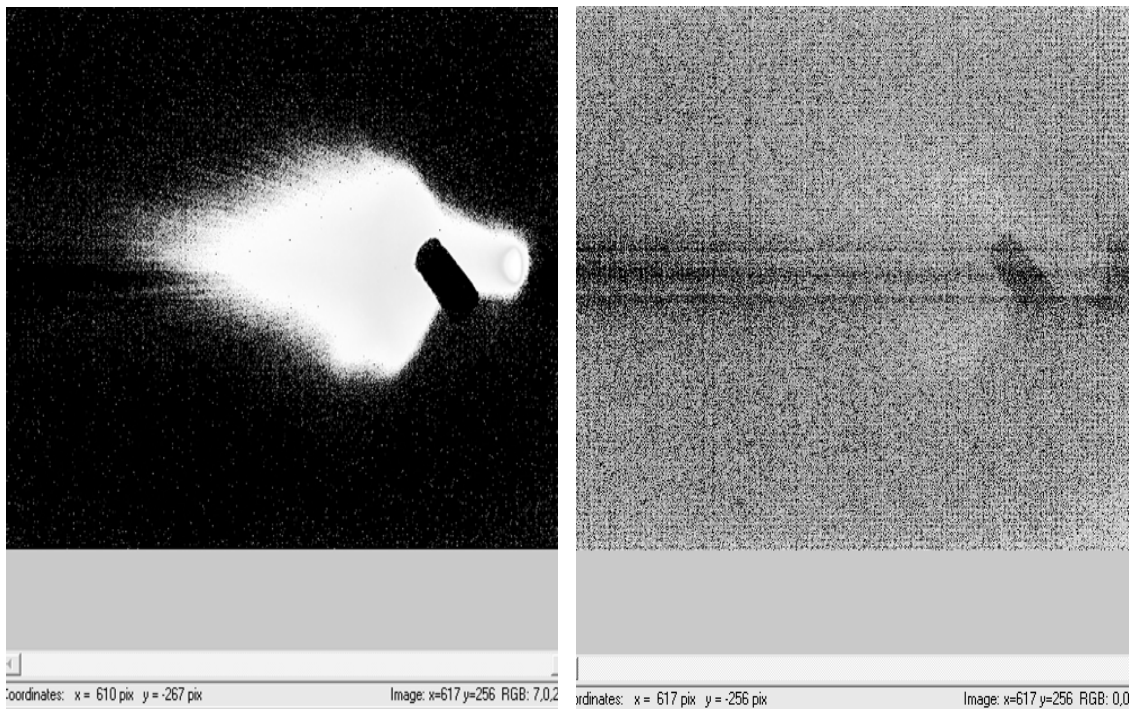


Figure 2. Example of a residual (latent) image. Initial images of cartridge silhouette in frame 339 (left), and a subsequent image in frame 349 (right). The camera was framing at 200 pps. Settings for contrast, gamma, and brightness are the same for both images and have been modified to enhance the silhouette.

### **2.1.3 Software**

#### **Control**

Commands are sent to the Phantom camera through a standard Windows Graphical User Interface (GUI) that allows the user to establish data acquisition parameters and set the recording mode. In the case that highly transient phenomena exceed the capabilities of human reaction, the instrument may be synchronized to an event through a “hard,” TTL, electronic, 5-volt trigger. Typically, however, the camera provides enough recording time at high frame rates for the user to respond manually with a “soft” software trigger. Both “soft” pre-trigger and post-trigger options are available through the GUI. Under circumstances where the event time interval is much smaller than the total recording time, a soft post-trigger is sufficient to capture the entire event.

#### **Calibration**

Two simple calibrations may be performed to improve image quality. White balancing adjusts color ratios based on a non-saturated 16 x 16 or 32 x 32 segment of the FPA, defined as white by the user. This is accomplished by placing a white or nearly white object in the detector field of view. Captured images that contain objects known to be white can also be white balanced. White balance can also be adjusted manually using slider bars. A black reference is performed with the lens cap in place (or the FPA otherwise in total darkness) and sets the FPA pixels uniformly to zero digital number. The black reference must be taken prior to data acquisition and is not reversible.

#### **Processing and conversion**

The phantom camera control software is designed to allow a limited amount of

image processing and analysis. Basic image adjustments may be performed using slider bars that modify brightness, contrast, gamma, and saturation. Various filters may also be applied to enhance gradients in digital numbers, and sharpen or smooth images. Both filters and image adjustments may be applied before or after data acquisition and both processes are reversible in either case. It is assumed that zero modification is the closest equivalent to the raw FPA readout with the digital values altered only according to the white balance and black reference calibrations. The Phantom software is also equipped with code to convert and compress individual images and entire video files from their native Cine (.cin) file-type to more common file-types. Multiple conversion options are available for stills but a 24 bit format such as Bitmap24 (.bmp) is preferable to maintain the appropriate color-space. Video files may be converted to the Audio Visual Interlaced (AVI) (.avi) format. Any processing applied before a conversion is irreversible in the converted file for both stills and videos; this is undesirable if the conversions are meant for further processing where individual pixel values are important.

## **Analysis**

The native software provides several tools for making mechanical analyses. Scaling is accomplished with a function that allows the user to identify a known length-scale, present in the image, and set the appropriate units. Linear and angular kinetic measurement functions may also be selected by the user. Measurements of an individual target are taken by marking the coordinates of the target at different frames in a video. Differences in time are determined by the frame interval. Ideally all measurements should be taken in the same plane as the original scale marker, since length scale will vary with

distance from the camera. However, in cases where the scale of the event is much less than the distance to the event, errors generated by ignoring the geometric idealization are insignificant. Image histograms detailing the number of pixel counts per digital number can be generated for the separate RGB bands or in-total for each image.

## 2.2 Field Tests

Data was gathered over the course of roughly 12 months at four separate field tests. The author had direct participation in the two latter tests. The tests are listed in order of occurrence.

### 2.2.1 Bronze Scorpion (Yuma)

The Bronze Scorpion data set was acquired between 17 and 19 November 2004 at the US Army Yuma Proving Ground in Yuma, Arizona (1). Data acquisition was managed by the National Air and Space Intelligence Center (NASIC) and the Air Force Institute of Technology (AFIT) (1). The test was designed to explore the nature of explosive signatures with the detonation of a small variety of US howitzer warheads (1). Teams from NASIC and AFIT deployed a suite of spectro-radiometric and imaging devices to collect data for subsequent signatures analysis (1). Table 1 lists the applicable geodetic data for the test (1).

Table 1. Geodetic data for Bronze Scorpion test.

Location	Latitude (deg)	Longitude (deg)	Elevation (m)	Target distance (m)	Target bearing (deg)
Ground zero	33.321249	-114.330074	1347	x	x
Observation site	33.330689	-114.331597	1420	1076	170

There were 65 events in total, involving the detonations of 105mm M760 and 155mm M107 howitzer projectiles. The M760 shells had a 4.6 lb TNT-fill, while the 155mm shells had either 14.6 lb TNT or 15.4 lb composition-B fills. Test munitions were detonated using a 5/16 lb (approximately ¼ stick) of C4, packed into the shell's fuse well (1). Shells were detonated individually. However, in the event of a misfire, the defective shell was then paired with another. One additional test involving an M107 composition-B shell, supplemented with 12.5 lbs of C4 was also conducted (1). The M760 and M107 shells are depicted in Figure 3.



Figure 3. M760 105 mm Cartridge (left), M107 155 mm Comp-B (center), and TNT Cartridge (left).

Data acquisition by the phantom was performed for 29 of the 65 events. No white balances or black references were performed on the Phantom camera during these tests. Individual descriptions of each event, and associated Phantom camera settings where applicable, may be referenced in Appendix A-2. The camera settings were determined through trial and error by the operator.

### **2.2.2 Northern Lights II (NL2)**

The Northern Lights II tests took place over the period July 11 to 22, 2005 on the Multi-burst Site of the Experimental Proving Grounds (EPG), Defence Research and Development Canada (DRDC) Suffield (13). The tests were conducted for the purpose of collecting radiometric, imagery, and overpressure data for various explosive configurations (13). Data acquisition was managed by NASIC; AFIT was not a direct participant in the test. However, AFIT did deploy instrumentation, including the Phantom v. 7.1, to supplement that of NASIC. The geodetic data for ground zero follows as: 50° 16' 33" North latitude, 110° 54' 47" West longitude, 704.1 m mean sea level altitude.

Test charges were modulated according to 1) mass (20kg or 150 kg); 2) casing geometry (spherical or cylindrical); 3) casing material (aluminum, steel, or polyethylene); and 4) explosive type. As a consequence of the variability, there was no repetition of any one configuration. Charges were suspended between two vertical poles and detonated above a level concrete surface to minimize the influence of disturbed debris and particulates on fireball data (13). A view of the target area, as seen by the Phantom camera is given in Figure 4. Burst heights for the 20 kg and 150 kg charges were three meters and six meters, respectively (13). The test sequence was organized such that

polyethylene charges were detonated first, followed by aluminum, then steel (13). Casing geometry was alternated, successively, while mass was varied serially, beginning with 20 kg and concluding with 150 kg devices. Individual test descriptions and associated instrument settings may be referenced in Appendix A-3.



Figure 4. View of the target area from the Phantom camera. The suspended charge is centered in the white circle.

### **2.2.3 Dual Thrust Smokey SAM (DTSS)**

The intent of this test was to produce imagery and spectral data for the exhaust plumes of DTSS rockets, tethered to a ground test stand (3). Data were acquired jointly by AFIT and AFRL. The DTSS tests took place 26 October 2005 on the Wright-Patterson Air Force Base Area-B test range. The location is depicted in Figure 5. Six identical rockets were fired and their burns were recorded by a suite of instruments, including the Phantom v. 7.1, 139 feet down range. Each burn was made in the same orientation such that the instruments were looking perpendicular to the length of the plume. Sky conditions were either cloudy or dark so illumination of the target was always uniform in the visible spectrum. Figure 6 illustrates the rocket--test stand configuration.

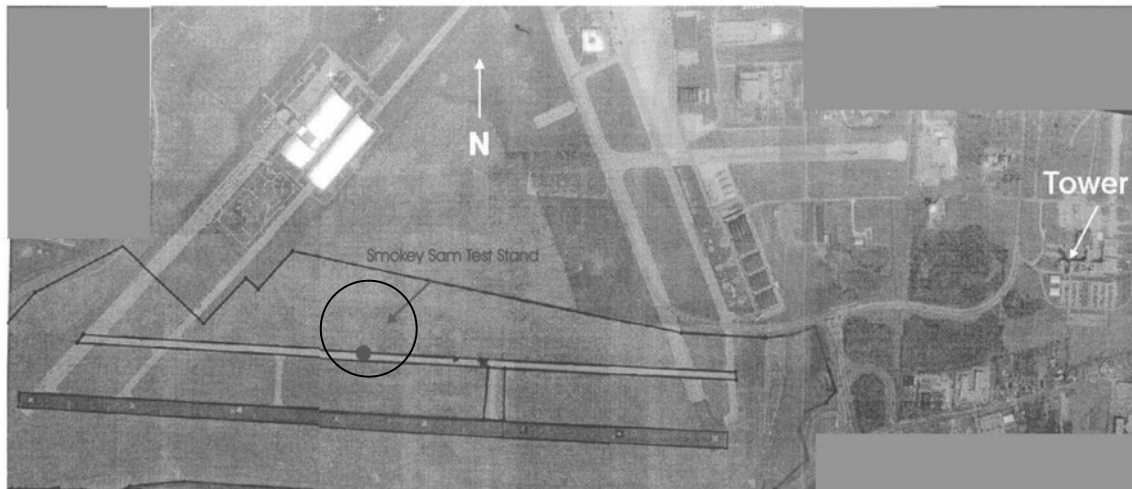


Figure 5. Location of Smokey SAM test stand, WPAFB area B



Figure 6. Test stand with rocket un-ignited (top) and ignited (bottom)



Specific event data and instrument settings may be referenced in Appendix A-4. A frame rate of 1000 pps was requested by AFRL to evaluate the propagation of missile body vibrations into the plume. Integration time and aperture settings were adjusted to maximize dynamic range and minimize detector saturation.

#### **2.2.4 TPL muzzle flash**

The purpose of the muzzle flash tests was to measure the brightness of a novel, “flash-less” gunpowder flash relative to off-the-shelf varieties. Determination of absolute flash radiance was not an objective. The tests took place over the period 28 November—01 December 2005 at the WPAFB Area-B test range number 1. The range was completely enclosed and provided near total darkness (in the visible spectrum) during data collection. All events were .45 caliber rounds, fired from a pistol that was secured with a Ransom Rest. Tests combined frangible or full metal jacket (FMJ) projectiles with either conventional, Wolf, or novel powder types. Multiple firing sequences, each with one to seven rounds, were recorded by a suite of instruments including the Phantom v.7.1. Event types and collection parameters may be referenced in Appendix A-5.

Several test firings were incorporated into 28 and 29 November, which permitted instrument adjustments necessary to maximize data collection. Due to low radiance of the events, collections at high frame rates used only a small portion of the dynamic range of the detector. Frame rates were adjusted from 2000 pps to 100 pps in order to ensure accurate, relative brightness comparisons among the different powder types. An attempt was made to improve temporal resolution by increasing frame rate to 200 pps but this had

negligible impact. In the interest of maintaining consistency in the data, frame rate was not adjusted any further.

The instrument arrangement, depicted in Figure 7, was the arrangement used while collecting actual data but differed for the test-firing sequences.



Figure 7. The instrument arrangement for TPL muzzle flash tests. The Phantom camera is at the approximate center of the image (left ellipse). The test pistol is slightly below and to the right (right ellipse).

Note the angle that the phantom camera made with the line of fire, which was perpendicular to the plane of the image in Figure 7. Ideally, profiles of the flash would have been recorded perpendicular to the line of fire but the large number of instruments and proximity to the target precluded this. Clearly evident in Figure 8 is the oblong

appearance of the gun barrel opening due to a viewing angle that was not perpendicular to the line of fire.

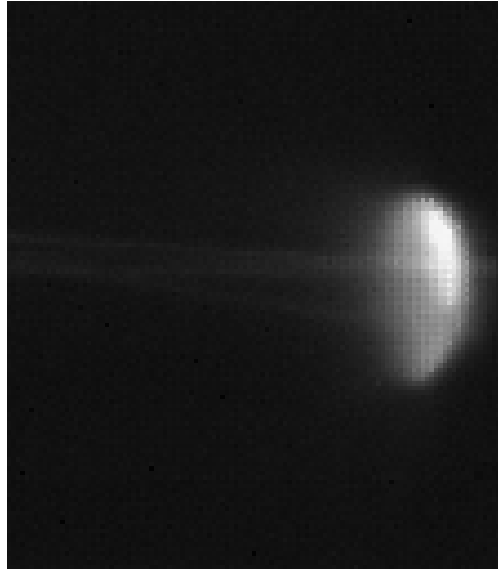


Figure 8. Muzzle flash captured by Phantom. The cumulative gray and white region constitutes the gun barrel opening.

### **3. Data Analysis and Characterization**

The primary objective of this research was the characterization of phenomena observed in the high-speed video imagery. This section details the measurements of those phenomena and the procedures used to generate them. Optical depth observations and kinetic analyses of shockwaves were derived from the detonation events recorded at Yuma and NL2. Vorticity analyses were derived from Yuma data only. Image processing was performed on all four data sets.

#### **3.1 Methodology**

Data analysis was accomplished using both the indigenous Phantom software, and MATLAB. Phantom software was used primarily to take geometric, kinetic, and temporal measurements of vortices, secondary shockwaves, secondary detonations, and reflected shockwaves observed in the Yuma and/or NL2 data. MATLAB was used on the Yuma, NL2, and DTSS data (to a limited extent) to perform image processing analysis of the spectral information derived from the three color bands. MATLAB was also employed to investigate the reproducibility and relative brightness of the muzzle flash events. Rigorous measurements of optical depth for the detonation events could not be made directly from the imagery; characterizations respective of this phenomenology were contingent on qualitative observations only.

##### **3.1.1 Phantom Software Processing**

###### **Timing**

Temporal measurement relative to event initiation, at time  $t = 0$ , is derived from frame

number, frame rate, and frame interval which are all displayed by the Cine file viewing interface. Since frame rate and integration time are constant throughout a collection, the interval between frames is constant.

### **Linear scaling**

Scaling is introduced by the user in one of two ways: the user sets the desired units and 1) identifies two markers, whose actual separation is known, lying in the image plane a distance  $d$  from the camera; or 2) calculates the actual length projection of an integer number of pixels, a distance  $d$  from the camera. Either method produces scales that are valid for the image plane perpendicular to the camera's line of sight at distance  $d$ . Linear measurement determines the projection of a separation vector onto the scaling plane. Measurements that are non-coplanar with the scaling plane are thus subject to scaling errors. Assuming zero camera motion during data acquisition, the scale applied to any frame of a video file is valid throughout the entire video. 1) and 2) above were applied to NL2 and Yuma respectively. The NL2 scale reference points were determined by a) the suspended munitions and b) a line on the ground, connecting the two suspension poles. This separation was fixed at three or six meters, depending on munitions mass but the scaling factor was reintroduced for each event in the NL2 data set to ensure accuracy. The linear projection of a single pixel at the distance of the detonations was 0.0529 meters for the Yuma events. This was kept constant since there were no scale markers in the background and only the target distance was known.

### **Length computations**

Lengths are computed by marking two points in an image or video still. The

software then uses the applied scaling values to determine the distance between the points, assuming both points lie in the scaling plane.

### **Linear velocity computations**

Displacement is determined by application of the length scale factor to the difference in target position between two separate video stills. The time separating the stills is derived, automatically, from frame number and frame interval. Positions, velocities, and accelerations of a target can also be computed with a software tool that allows the user to record the location of a target over several frames.

### **Angular velocity computations**

Angular rate is determined by selecting, in one frame, a vertex and a second point which, together, define a reference axis. A third point, selected in a different frame, marks the angular displacement of the reference axis. Timing is as per linear velocity. Angular velocities are independent of length scale and can be measured without the introduction of a scale factor.

### **3.1.2 MATLAB processing**

It was postulated that the limited spectral information, contained in the Phantom camera's three color-bands, might hold useful features (6). MATLAB scripts were applied to the Yuma, NL2, and DTSS data to analyze ratios of color values within pixels and time derivatives of color values. Several processing variations were tested on a small sub-set of data-files drawn from the four field tests. However, in the absence of any a-priori knowledge about what type of processing would be most useful, it was necessary to experiment through trial and error. Data was converted from the Cine format to the

uncompressed AVI format before it was read into MATLAB. Without direct knowledge of the specific band passes, wavelength-dependent pixel responses, and automatic processing, the physical meaning of individual pixel values is uncertain.

Muzzle flash data was also processed using MATLAB. Only the initial frame of data for each of the muzzle flash collections was included due to the residual image artifact. Means and standard deviations were computed, separately for each color, over the entire array. Events were then plotted according to their means (x-axis) and standard deviations (y-axis). The degree of clustering and separation of the data sets in the moment plane were taken to be the reproducibility and relative brightness, respectively.

### **3.1.3 Measurement difficulties and quantification of uncertainty**

#### **Vortices**

Vortices were chosen from the from the daylight events of the Yuma test only since the night events were too unfocused for vortex identification. Motion was typically required to make a vortex contrast with the background. Selection, in the amount of one to three targets per event, was contingent on propensity for accurate measurements of diameter and angular velocity. Temporal location, relative to event initiation, was not considered as a selection criteria.

Long periods of growth and fading, and motion-dependent identification often made exact times of vortex appearance and disappearance impossible to ascertain. Approximate appearance times were determined by starting the video when the vortex was definitely absent and running forward until the vortex was definitely present to determine an appearance time upper-bound. Running the video backward from definitely

present to definitely absent was used to determine an appearance time lower-bound. This same strategy (reversed) was applied to determine upper and lower bounds for disappearance time. Slower vortex motion required faster video playback to achieve the requisite contrast, which necessarily increased the uncertainty in the associated times.

Vortex diameters were determined with length measurements using the Phantom software. However, the interpretation of a vortex boundary was somewhat subjective. Ideally, such a boundary would be the edge of the rotating region of fluid but in practice this was difficult to identify in a still image. Typically a sequence of frames had to be repeated several times to generate a clearer representation of the boundary. Since vortices were not perfectly circular, two measurements of diameter were taken. The mean value then became the diameter and the difference between the mean and one of the measurements was used to estimate the uncertainty.

Angular velocity measurements were also performed with the phantom software and faced the same difficulties as those for diameters. Additionally, it was often difficult to identify suitable markers in a vortex region subject to little change during rotation. Due to this potentially increased error, three measurements of angular velocity were computed for each vortex. The mean value became the angular velocity and the greatest difference between the mean and any of the three measurements was used to estimate the uncertainty. However, due to large variations of uncertainty computed with this method and a seemingly high probability of over or under-estimation, the individual uncertainties were used to compute a mean uncertainty as a percentage of the measured value. The fractional uncertainty was then applied to the whole data set.



## **Shockwave phenomena**

As with vortices, reflected shock fronts did not have perfectly localized boundaries and were also difficult to distinguish in still images. Again, multiple repetitions of a series of frames were necessary to isolate shock front locations. The procedures for identifying initial and final observation times for the shockwaves were the same as those applied to find the appearance and disappearance times of vortices. Phantom software was used to determine linear velocities. Given the high position uncertainty and transient nature of these phenomena, five measurements of linear velocity were recorded for each shock to bolster accuracy. The mean velocity became the reported velocity and the greatest difference between the mean and any of the five velocity measurements was used to estimate the uncertainty. Velocity measurements of the primary shockwaves were also compiled for comparison.

Secondary shocks were much less transient than reflected shocks but were usually subject to low contrast and it was necessary to use the horizon to track their motion. Therefore, as a consequence of geometry, true shock front speed was not directly measured but may be derived under the assumption of spherical expansion. Measurements of secondary shock positions as a function of time (or frame) for each event were taken at, approximately, ten-frame intervals over the duration of observation. Measurements of both primary and secondary shocks were made, for the purpose of comparison. Due to the temporal separation of the two shocks, measurements were not, in general, simultaneous but did occupy approximately the same spatial interval. Fits of leftward and rightward propagation speeds were made independently for each shock, and

combined such that the mean of the slopes of the left and right fits became the reported speed. The difference between the mean and either of its component fits was used to estimate the uncertainty.

### **Secondary detonations**

Secondary detonations were visible in a few of the NL2 events. These were highly transient but had enough contrast to make them easily identifiable. Initiation and termination times were apparent to within a few frames. The reported velocity was the mean of three separate velocity measurements, taken using the phantom software. The greatest difference between the mean and any of the three measurements was used to estimate the uncertainty.

## **3.2 Characterization of Phenomena**

This section details the general results of the analyses performed following acquisition. Gathered data for vortices, shocks, and secondary detonations were recorded in *Microsoft Excel*. *Excel* was also used to generate the plots that display relationships between vortex parameters. Color band and muzzle flash analysis was performed exclusively in MATLAB.

### **3.2.1 Vortices**

Forty-seven vortices, drawn from 21 events of the Yuma test, were recorded and analyzed. Diameter (or radius  $r$ ), angular speed (velocity)  $\Omega$ , location, appearance time  $t_a$ , and disappearance time  $t_d$  were all observed directly in the data and were not derived from other parameters. Duration  $\Delta t$  was taken as the difference between the disappearance and appearance times. These data are summarized in Table 2.

Sample range and outlying data points are the sources of the excessive standard deviations observed for angular speed, appearance time, disappearance time, and duration. It is evident that earlier appearance times were chosen more frequently than later times and smaller angular velocities were chosen more frequently than larger angular velocities. Considering that the only bias applied to vortex selection was measurability, it is statistically plausible to conclude that more vortices form with lower angular speeds and at earlier times.

Table 2. Statistics for vortex data. Appearance time refers to the initial observation of a vortex relative to event initiation at time  $t=0$ . Disappearance time refers to the final observation of a vortex relative to event initiation at time  $t=0$ . Duration refers to the longevity of observation of a vortex.

	Maximum	Minimum	Mean	Standard deviation
Diameter $r$ (m)	1.79	0.317	0.697	0.302
Angular speed $\omega$ (rad/s)	2150	14.8	315	430
Dist from origin (m)	4.23	0.635	2.17	0.886
Appearance time $t_a$ ( $\mu$ s)	145000	1400	31000	34600
Disappearance time $t_d$ ( $\mu$ s)	249000	2900	57800	59500
Duration $\Delta t$ ( $\mu$ s)	121000	1200	26700	29000

Table 3. Statistics for vortex data using log scales

	Maximum	Minimum	Mean	Standard deviation
Log ( $\omega$ )	2.54	0.374	1.36	0.559
Log ( $t_a$ )	5.16	3.15	4.20	0.564
Log ( $t_d$ )	5.40	3.46	4.49	0.548
Log ( $\Delta t$ )	5.08	3.08	4.12	0.580

Disappearance time is omitted due to its systematic dependence on appearance time. The range and outlier artifacts may be avoided by switching to a logarithmic scale for those parameters where the standard deviation exceeds the mean. Comparative plots for data distribution using log and linear scales are provided in Figure 9. Table 3 repeats the data summary using a  $\log_{10}$  scale where appropriate and Table 4 lists the uncertainties associated with the measurements given in Table 2.

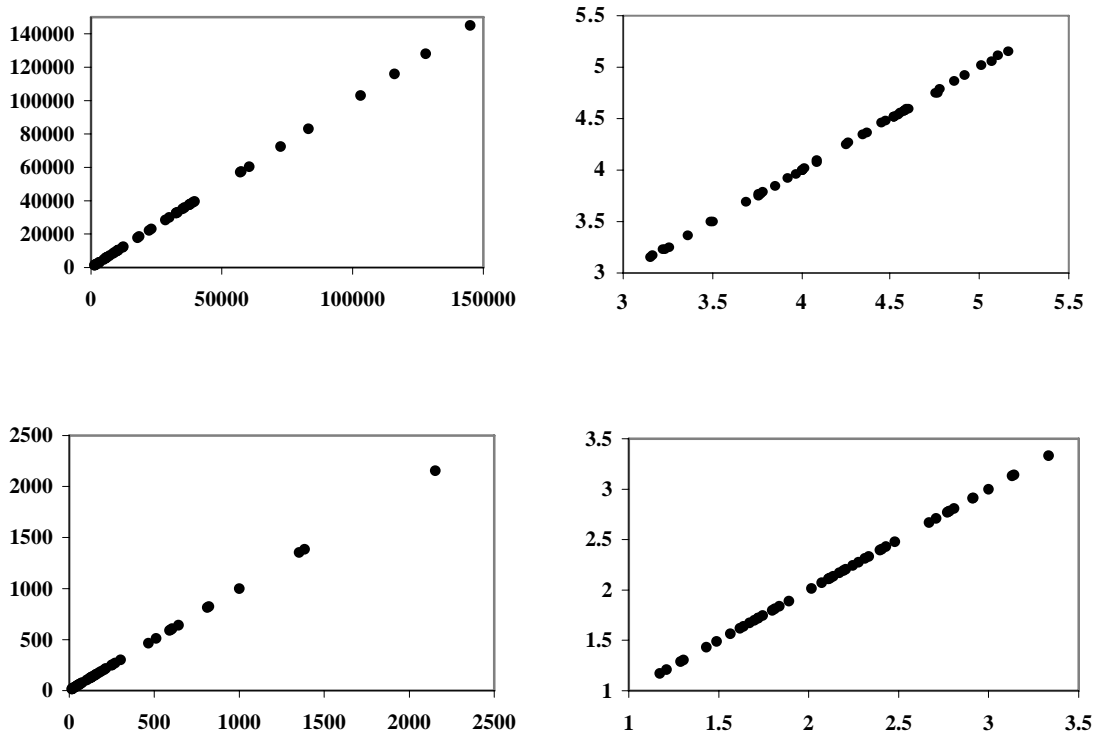


Figure 9. Comparative plots for data distributions using linear and log scales. Data for  $t_a$  (upper left),  $\text{Log}_{10} t_a$  (upper right),  $\omega$  (lower left), and  $\text{Log}_{10} \omega$  (lower right) was plotted against itself to illustrate its distribution in one dimension.

Several correlations among the vortex parameters have been identified. The choices of the axes, though arbitrary in terms of correlation statistics, reflect causality where appropriate. Figure 10 illustrates the trend for angular speed relative to appearance

time. This trend may be summarized with the statement that vortices spin more slowly at later times relative to event initiation. The decrease is very rapid, given the log-log scale of the plot, occurring over  $10^{-1}$  second. Interestingly, a relationship between angular speed and vortex linear dimensions was not observed; an explanation is forthcoming.

Figure 11 illustrates a similar but stronger trend for disappearance time. It is believed that these relationships arise as a result of continually decreasing energy available to drive vortex motion. On linear scales, these relationships are power laws, shown in Figures 12 and 13.

Table 4. Measurement uncertainty statistics

	Max	Min	Mean	Standard deviation
Diameter uncertainty (m)	2.78	0.025	0.624	0.608
% Diameter Uncertainty	14	0.249	4.42	3.27
Angular speed uncertainty (rad/s)	98.4	0.324	17.5	25.4
% Angular speed uncertainty	104	1.72	39.1	21.9
Appearance time uncertainty ( $\mu$ s)	17000	82	4000	4680
% Appearance time uncertainty	31.5	1.45	12	6.66
Disappearance time uncertainty ( $\mu$ s)	25000	100	6370	6600
% Disappearance time uncertainty	24.9	2.86	11	5.81

Figure 14 gives the relationship between the angular speed of a vortex and the duration of time for which it was observed, assuming it was not obscured from the camera. Error bars in this and subsequent figures are occasionally truncated to avoid excessive plot size. Since obscuration of a vortex should be a random process, the presence of a correlation indicates that dissipation, rather than obscuration, was the predominant cause of vortex disappearance. Duration was also found to correlate with appearance times (Figure 15) and disappearance times (Figure 16).

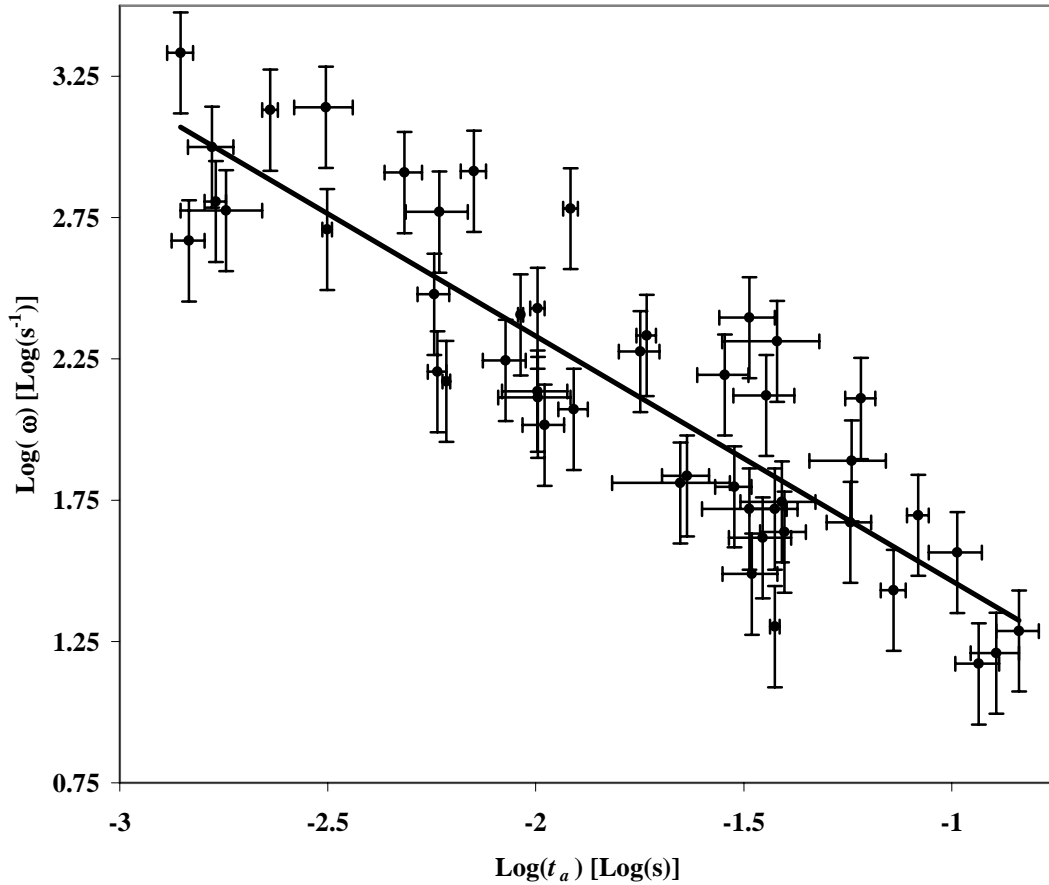


Figure 10.  $\text{Log}_{10}\text{-Log}_{10}$  Relationship between angular speed and appearance time for the entire set of vortex data. The regression line is determined by  $\text{Log } \omega = -0.8661 \text{ Log } t_a + 0.5989$ , with  $R^2 = 0.7648$ .

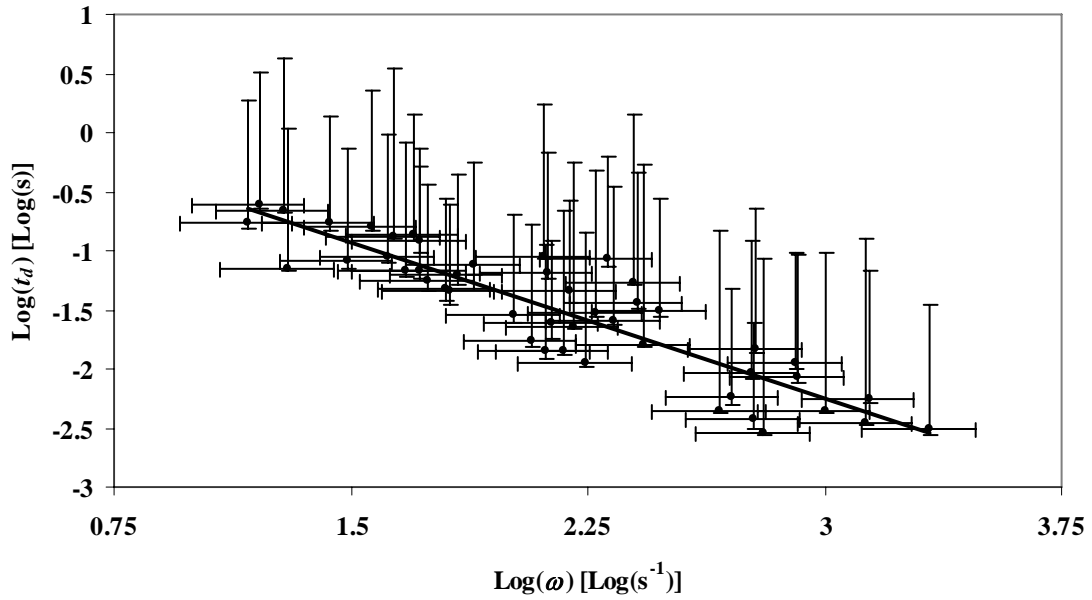


Figure 11.  $\text{Log}_{10}\text{-Log}_{10}$  Relationship between angular speed and disappearance time. The regression line is determined by  $\text{Log } t_d = -0.8793 \text{ Log } \omega + 0.3875$ , with  $R^2 = 0.8032$ .

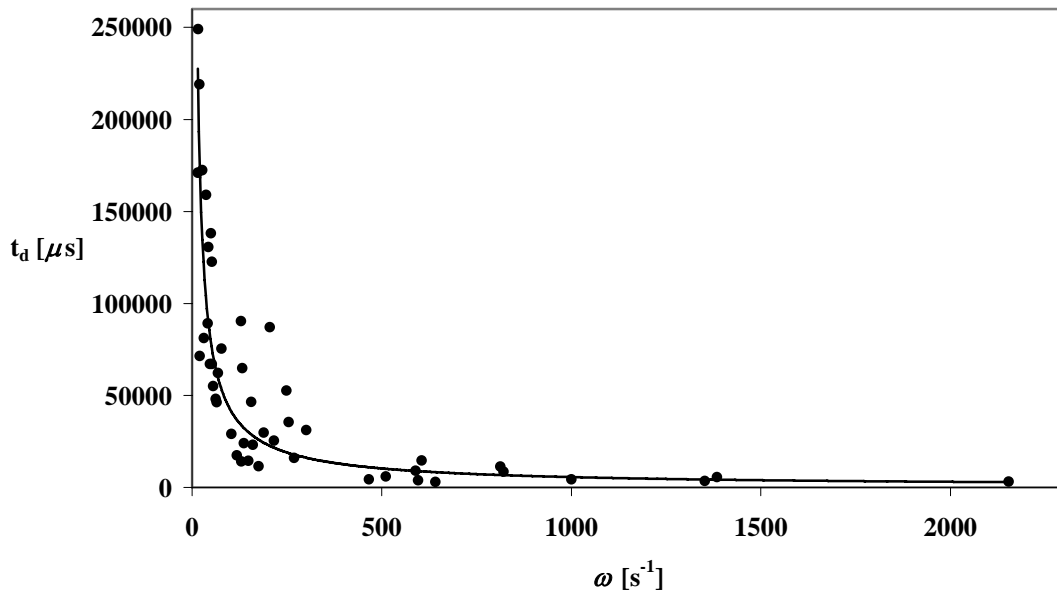


Figure 12. Relationship between time of disappearance and angular speed of a vortex on a linear scale. The regression curve is a power law given by  $t_d = 2 \times 10^6 \omega^{-0.8793}$ , with  $R^2 = 0.5693$ .

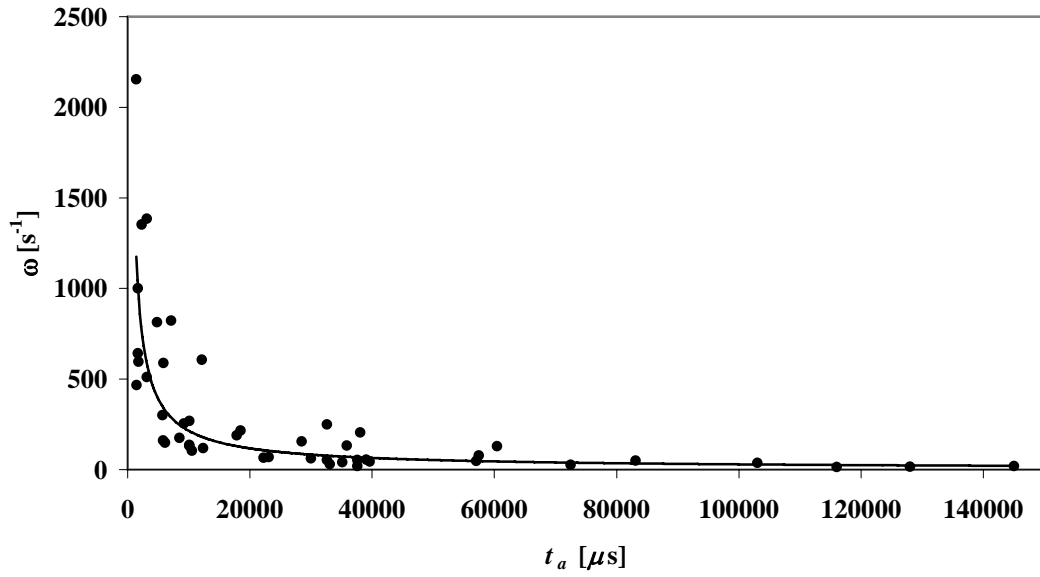


Figure 13. Relationship between angular speed of a vortex and its time of appearance on a linear scale. The regression curve is a power law given by  $\omega = 624031 t_a^{-0.8661}$ , with  $R^2 = 0.7648$ .

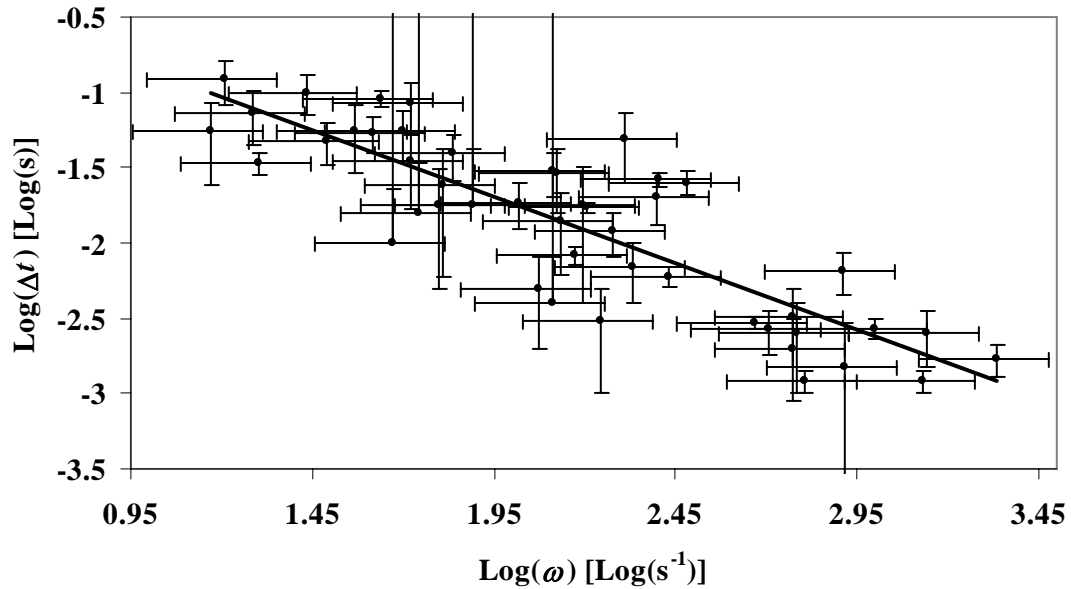


Figure 14.  $\text{Log}_{10}\text{-Log}_{10}$  relationship between the angular speed of a vortex and the duration for which it was observed. The regression line is determined by  $\text{Log } \Delta t = -0.8849 \text{ Log } \omega + 0.0316$ , with  $R^2 = 0.7259$



The difference in the strengths of the correlations illustrated by Figures 15 and 16 is due to the systematic dependence of disappearance time on duration. Nevertheless, it is evident that the time a vortex needs to dissipate is directly related to the time that it forms relative to event initiation. This is consistent with the relationship derived for angular speed and appearance coupled with the relationship derived for duration and angular speed. Vortices that appear earlier spin faster and vortices that spin faster dissipate faster.

Correlations also exist among several, physically meaningful combinations of measured parameters. The relationship between duration and the quantity

$$E = \omega^2 r^2, \quad (31)$$

which has units of kinetic energy per unit mass or mass-specific energy, is shown in Figure 17.

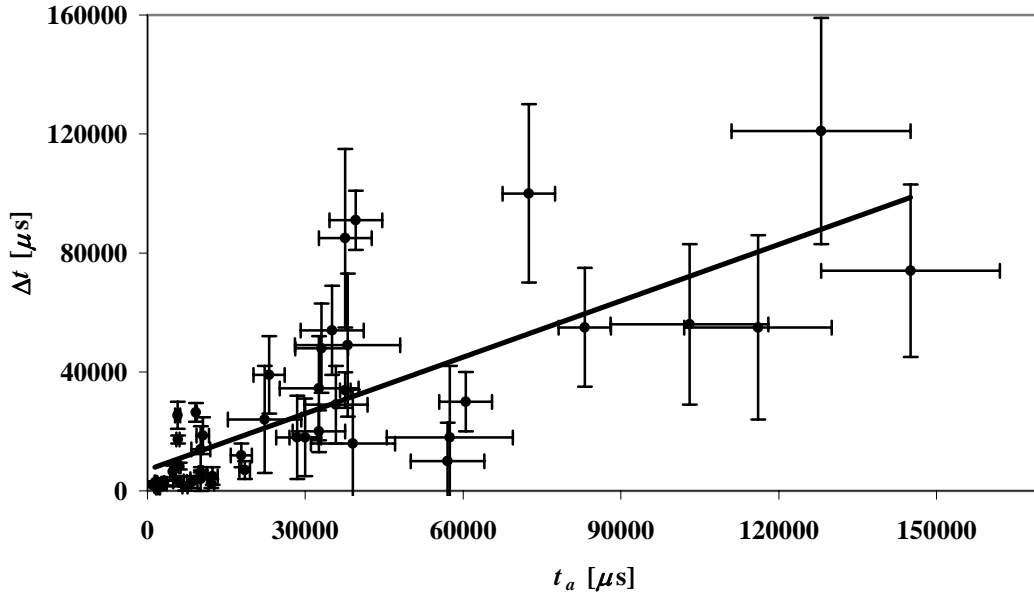


Figure 15. Linear relationship between duration of a vortex and its time of appearance. The regression line is determined by  $\Delta t = -0.6316 t_a + 7120$ , with  $R^2 = 0.5693$ .

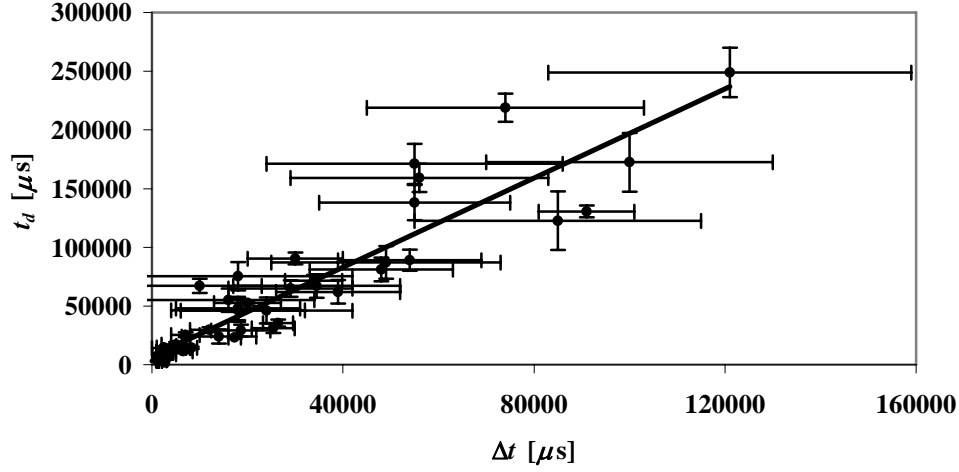


Figure 16. Linear relationship between duration of a vortex and its time of disappearance. The regression line is determined by  $t_d = -1.9013 \Delta t + 0.6952$ , with  $R^2 = 0.8547$ .

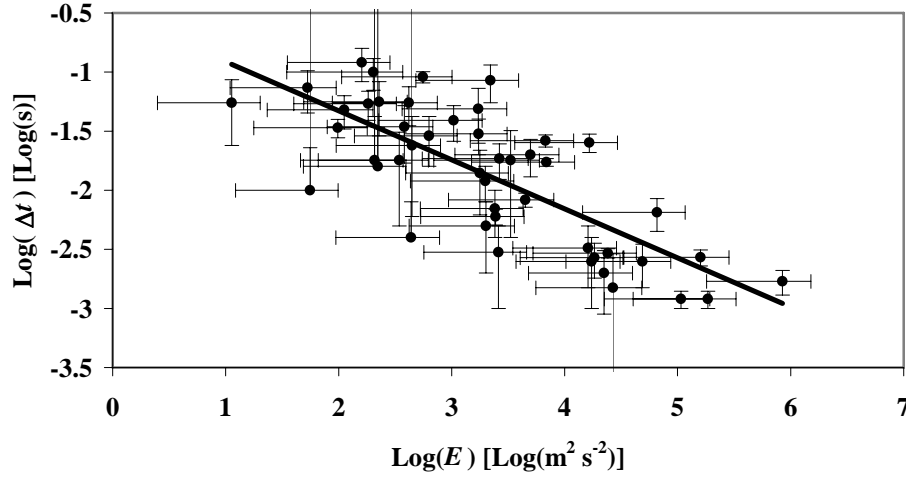


Figure 17.  $\text{Log}_{10}\text{-Log}_{10}$  relationship between vortex duration and energy. The regression line is determined by  $\text{Log } \Delta t = -0.4152 \text{ Log } E - 0.4954$ , with  $R^2 = 0.5769$ .

The longevity of a vortex apparently decreases with vortex energy, as is consistent with the previous conclusions. However, note that this correlation is weaker than the one between duration and angular speed (equal to the correlation between duration and the square of angular speed), presented earlier. The vortex diameter or

radius did not correlate well with any parameter on its own and is apparently the source of weakening. However, as it will be shown, in certain cases the presence of the radius serves to improve the correlation.

A proxy for mass-specific pressure of the gas in the vortex, presumably arising from the centripetal force of rotation, is given by

$$p = \frac{\omega^2}{r} . \quad (32)$$

Figures 18 and 19 show the relationships of this quantity with duration and appearance time respectively. It is clear that pressure correlations follow the same trend as those previous. It is also notable that the presence of  $r$  in Figure 18 improves upon the correlation between duration and angular speed presented in Figure 14.

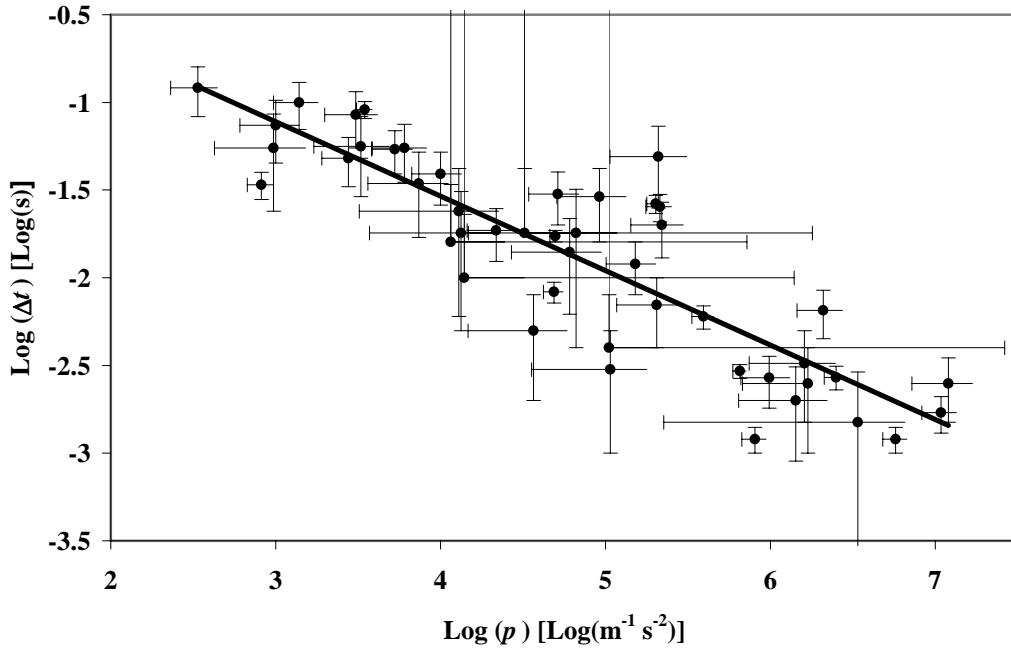


Figure 18.  $\text{Log}_{10}\text{-Log}_{10}$  relationship between pressure and vortex duration. The regression line is determined by  $\text{Log } \Delta t = -0.4243 \text{ Log } p + 0.1626$ , with  $R^2 = 0.7496$ .

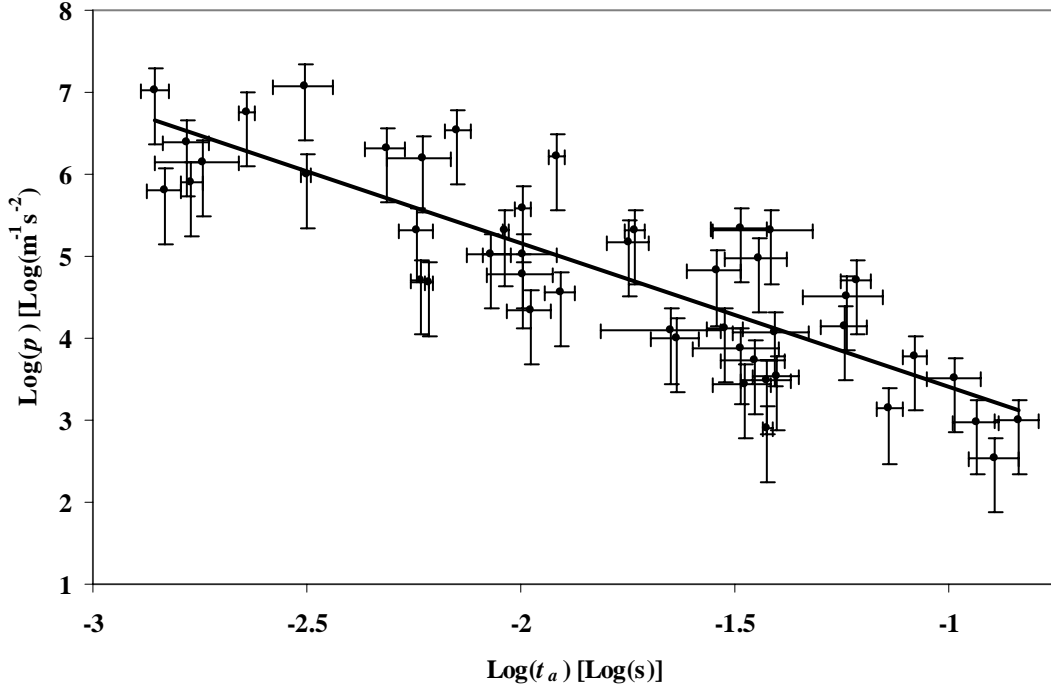


Figure 19.  $\text{Log}_{10}\text{-Log}_{10}$  relationship between pressure and appearance time. The regression line is determined by  $\text{Log } p = -1.7627 \text{ Log } t_a + 1.6357$ , with  $R^2 = 0.7056$ .

Revisiting energy, Figure 20 shows how this quantity is dependent on the time of appearance of a vortex. Proxies for mass-specific power may now be introduced as

$$W = \frac{\omega^2 r^2}{\Delta t} \quad (33a)$$

And

$$Y = r^2 \omega^3 \quad (33b)$$

The important distinction between the two is that (33a) represents the total change in energy over the life of the vortex by virtue of the duration term  $\Delta t$ , while (33b) is reminiscent of a true instantaneous change in energy. The correlations between power and appearance time is given in Figures 21 and 22.

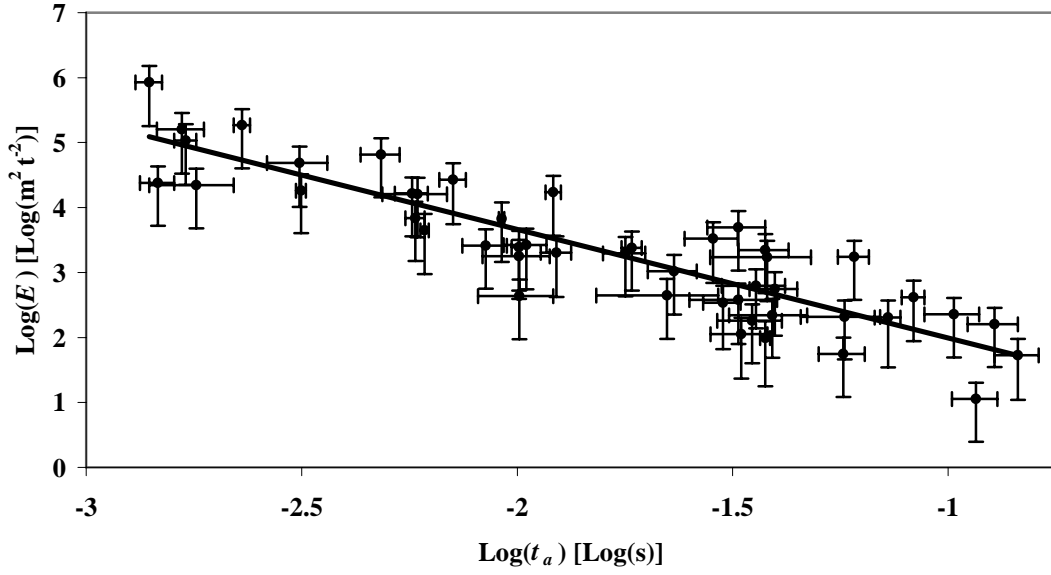


Figure 20. Energy of a vortex versus time of vortex appearance. The regression line is determined by  $\text{Log } E = -1.6709 \text{ Log } t_a + 0.322$  with  $R^2 = 0.7889$ .

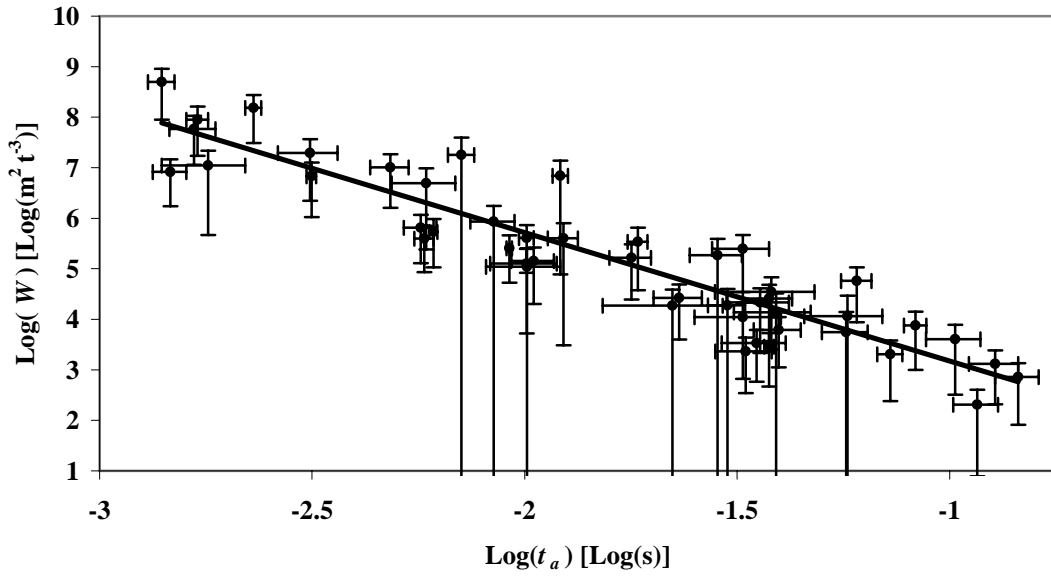


Figure 21. Power of a vortex versus time of vortex appearance using (33a). The regression line is given by  $\text{Log } W = -2.5416 \text{ Log } t_a + 0.6321$  with  $R^2 = 0.8572$ .

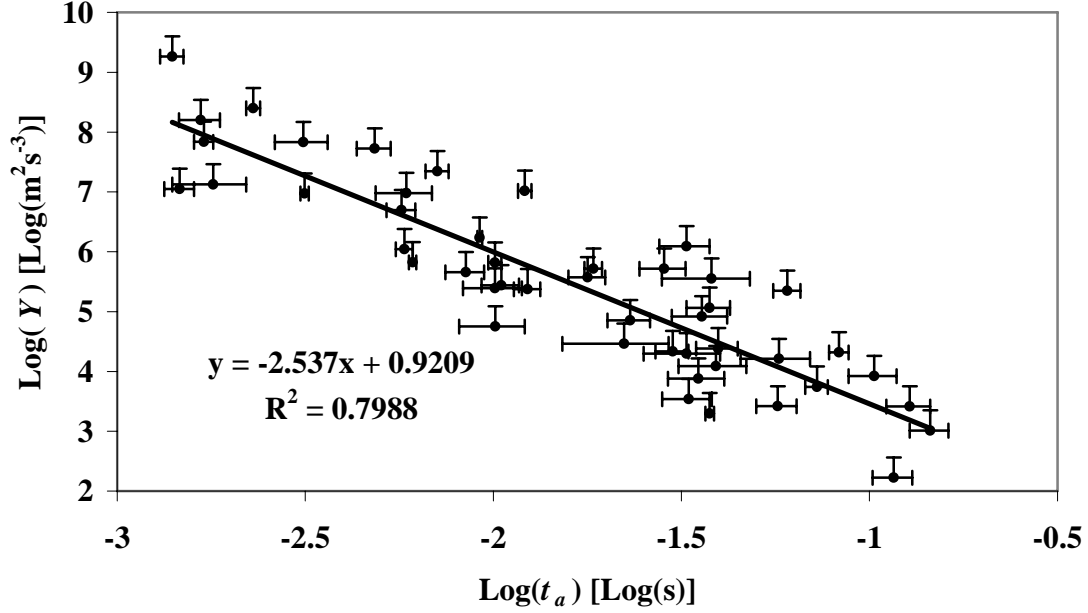


Figure 21b. Power of a vortex versus time of vortex appearance using (33b). The regression line is given by  $\text{Log } Y = -2.537 \text{ Log } t_a + 0.921$  with  $R^2 = 0.7988$ . The large uncertainties in measurements of  $\omega$  necessitated the truncation of the  $-Y$  error bars in this case.

The power-time correlation derived from equation (33a) was the strongest correlation that has been identified (barring those with systematic dependencies) and it indicates that vortex power is the source of the other correlations. The choice of appearance time was dictated by its independence from the other parameters.

Figure 22 demonstrates how reductions in correlation follow from incompleteness of the power parameter and provides additional justification for the physical significance of  $W$ . Furthermore, as indicated by the difference in  $R^2$  values between Figures 21a and b it is apparent that the  $\Delta t$  term carries some important physical information despite the lack of a true physical interpretation of  $W$ . Implied, in either case, is the fact that the  $W$  is somehow more fundamental than any of the directly measured parameters alone.

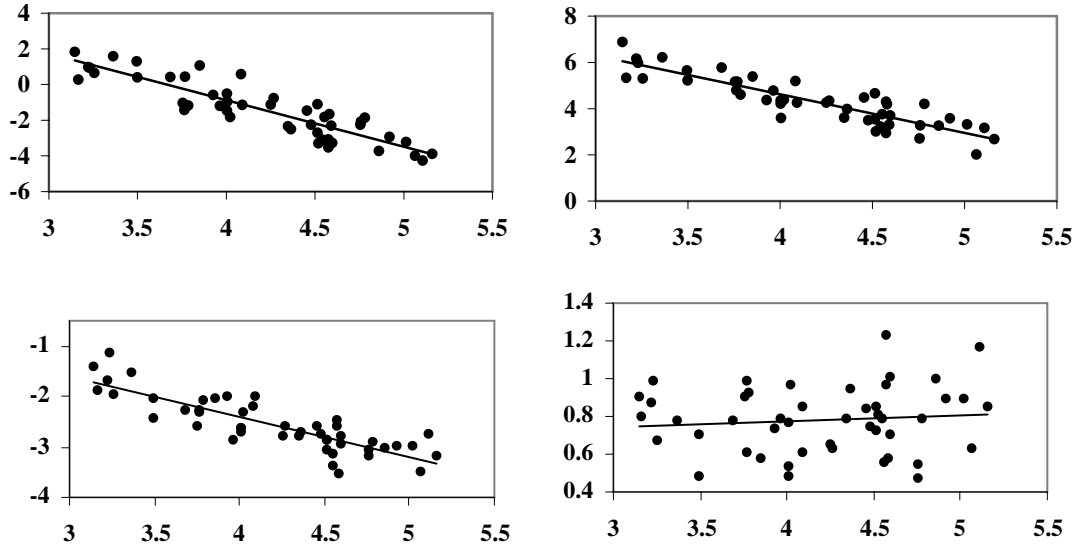


Figure 22 Comparative plots detailing correlations for incomplete parts of the power parameter with appearance time. Beginning at the upper left and moving from left to right: 1)  $\omega^2/\Delta t$  versus  $t_a$ ,  $R^2 = 0.8016$ ; 2)  $\omega^2 r^2$  versus  $t_a$ ,  $R^2 = 0.7889$ ; 3)  $r^2/\Delta t$  versus  $t_a$ ,  $R^2 = 0.7194$ ; 4)  $r$  versus  $t_a$ ,  $R^2 = 0.0097$ . Abcissae and ordinates are on a  $\text{Log}_{10}$  scale in all four plots, with  $t_a$  and  $\Delta t$  given in  $\mu\text{s}$ .

One must infer that the fit in Figure 21b carries real physical meaning inasmuch as it represents the rate at which kinetic energy of the fluid is transformed into heat through viscous forces, as a function of time. This has so far proven to be independent of explosive type, weight, and configuration. It should be stated, however, that the transfer of energy is local, i.e. in the neighborhood of a vortex. The global rate for energy transfer must, at the very least, be some modulation of the local rate with the observed decline in the number of vortices present at a given time.

### 3.2.2 Reflected shocks, secondary detonations, secondary shocks, and opacity

Structured phenomena were routinely observed in conjunction with detonation fireballs. Multiple examples exist in both the Yuma and NL2 data sets. Observation and

measurement were much simpler with the NL2 data due to the larger explosives, greater spatial resolution, and limited agitation of soil particulates. Distinctions among the different structures are dependent on where they are located in relation to the fireball and how they originate.

### **Reflected shocks**

Reflected shocks are the result of the interaction between the primary shock and the ground (or any reflecting surface) and are observed inside the fireball. This claim is based on the clear observations of reflection in the NL2 data set and is circumstantially applied to similar observations in the Yuma data, where structure origins can not clearly be identified. The reflected shock, while inside the fireball, propagates with a different velocity than the primary shock, owing to the difference in media. Figure 23 provides a clear example of a reflected shock and Table 5 summarizes the reflected shock data.

Table 5. Summary of reflected shock data. Reported times and speeds are not necessarily associated.

	Maximum	Minimum	Mean	Standard deviation
Initial time (us)	10800	2700	5400	2030
Final time (us)	12700	4700	7120	2090
Duration	2890	0.329	1720	712
Reflected shock velocity (m/s)	920	534	756	106
Primary shock velocity (m/s)	696	397	518	98.1



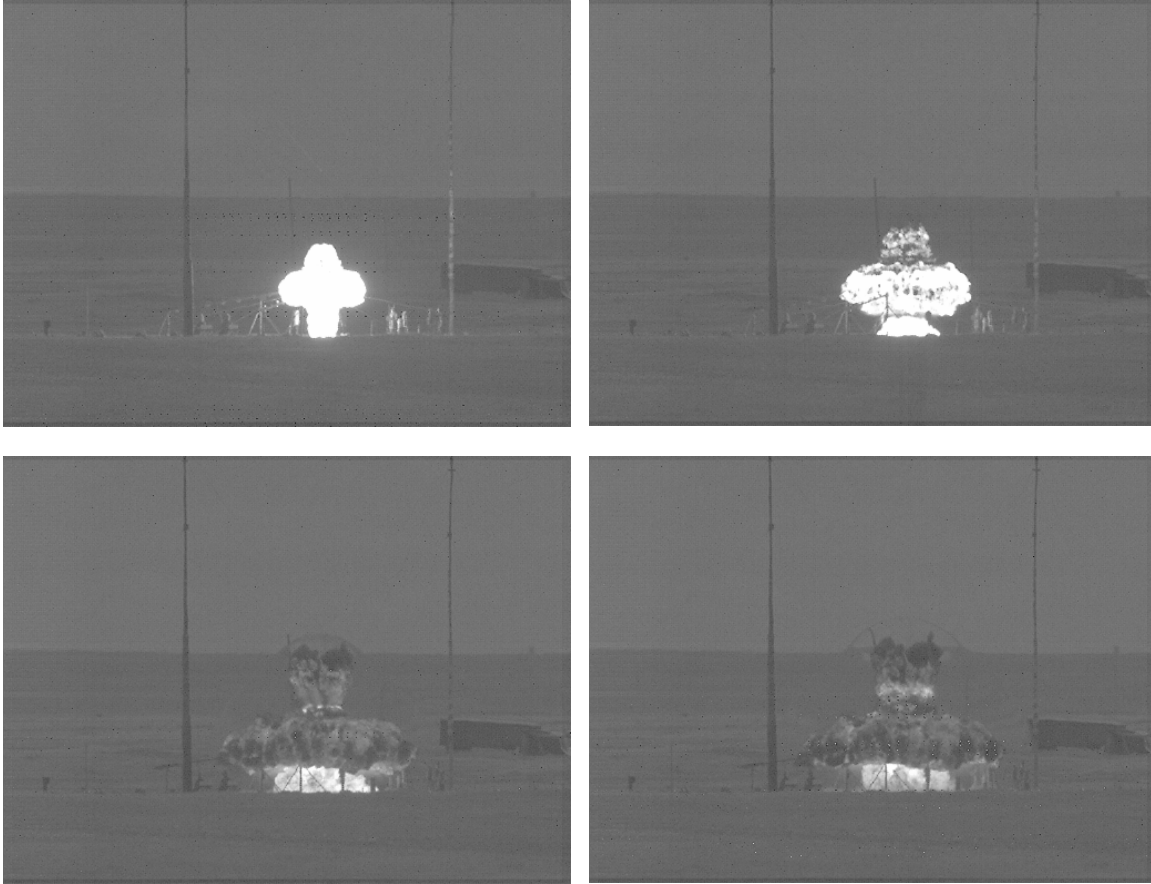


Figure 23. Progression of a shock reflection in NL2 event 2 through several (non-successive) images: 1) interaction with ground (upper left); 2) formation of dome-shaped reflection (upper right); 3) propagation of reflection (bright band) through fireball column (lower left); 4) continued propagation through fireball column (lower right). The cross-shaped fireball is due to the cylindrical geometry of the charge. Also note the primary shock at the top of the fireball in the lower two images. Gamma has been adjusted to enhance each image.

Although no direct correlation was discovered between the primary and reflected shock velocities, the propagation speed difference is readily apparent, as presented in Table 5. For the purpose of comparison, primary and reflected shock velocities were measured simultaneously. The secondary shock was always faster with a velocity difference well outside the uncertainty of either the primary or secondary shock velocity. This relationship is summarized in Table 6.

Table 6. Simultaneous velocities and uncertainties for the primary and reflected shocks. The far-left column gives the difference of the minimum value of the reflected shock and the maximum value of the primary shock, as determined by the respective subtraction or addition of the associated uncertainty.

Event	Reflected shock speed (m/s)	Reflected shock uncertainty (m/s)	Primary shock speed (m/s)	Primary shock uncertainty (m/s)	Minimum reflected-maximum primary (m/s)
322dat01	868	90.3	520	10.4	247
322dat03	815	23.1	433	18.8	340
322dat15	534	22.3	397	35	80.2
322dat52	708	123	421	74.6	88.5
322dat54	798	36.6	442	32	288
322dat57	920	74.5	556	23.9	266
322dat59	759	62.9	526	41.3	129
322dat61	726	13.4	427	43.8	241
322dat65	631	27.1	422	29	153
192dat02	742	74	530	34.9	104
192dat03	734	50.7	596	31.6	55.3
192dat04	613	2.02	483	60.3	67.4
192dat05	823	22.6	645	21.9	134
192dat06	778	18.5	696	19.4	44.4
192dat13	895	42.5	672	22.9	158

## Secondary detonations

Secondary detonations are structured ignitions of un-reacted fuel that remains in the region of the fireball, after the initial detonation. This causes a rapid increase in the apparent brightness and volume of the flame region. Secondary detonations, if they occur, appear to follow closely behind reflected shocks, as per observations in the Yuma and NL2 data. Figure 24 illustrates a secondary detonation and Table 7 summarizes the secondary detonation measurements. The small size of this data set also permits listing its entirety, given in Table 8. All the tabulated data comes from the NL2 events.

Table 7. Summary of secondary detonation data. Reported times and speeds are not necessarily associated

	Maximum	Minimum	Mean	Standard deviation
Detonation begin	11000	5200	6840	2220
Detonation complete	13400	7200	8900	2360
Duration	2600	1400	2060	446
Velocity	3490	857	1670	967

Table 8. Complete set of measurements taken for secondary detonations. All events were part of the NL2 test.

Event	Initial time ( $\mu$ s)	Final time ( $\mu$ s)	Mean detonation speed (m/s)	Uncertainty (m/s)	% Velocity uncertainty
189dat00	5800	7200	1790	332	18.5
192dat02	7700	9400	1090	209	19.1
192dat03	5410	7500	3490	507	14.5
192dat04	5200	7400	1080	45.4	4.2
192dat11	5900	8500	857	86.4	10.1
192dat17	11000	13400	1700	42.4	2.5

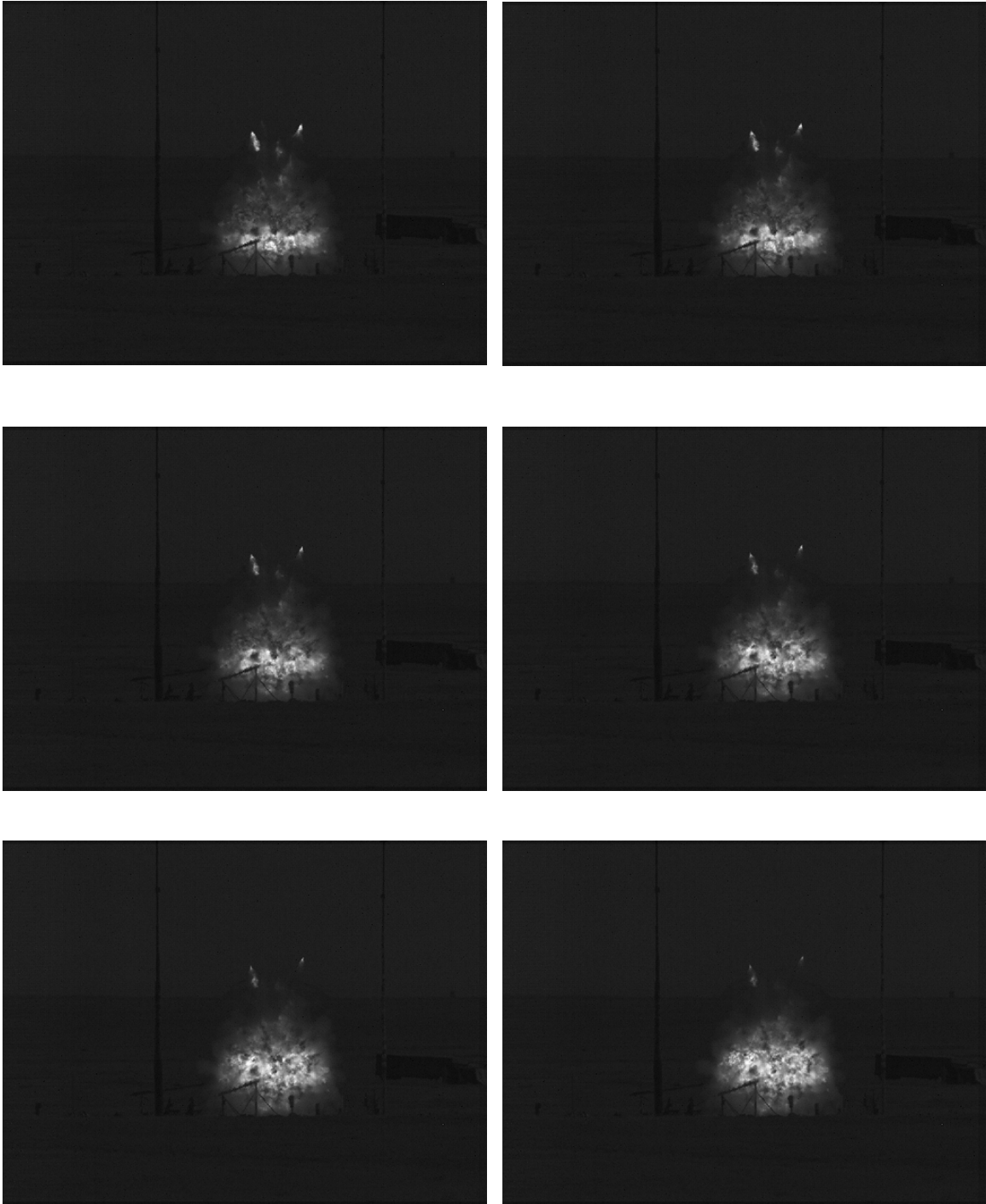


Figure 24. Sequential images of a secondary detonation in NL2 event 3, beginning in the upper left and moving from left to right. The detonation appears to be initiated when the reflected shock (bright band in the first image) reaches the approximate center of the fireball, where the primary detonation originated. The expansion of the bright region is

much faster than the primary or reflected shocks. Images have not been modified.

The transient nature of reflected shocks and secondary detonations was such that only one good, average velocity measurement could be obtained for the duration of observation. Reductions in measurement time significantly increased uncertainty. Out of 48 total events, 17 had at least one instance of a structured phenomenon.

### **Secondary shocks**

Secondary shocks are the products of secondary detonations and can be observed propagating outside the fireball behind the primary shock. An example of a secondary shock is presented in Figure 25. If both shocks had identical propagation profiles, their instantaneous speeds would differ due to deceleration but their positions as a function of time, and thus their average speeds would be identical. However, as one might assume, imagery shows that this is not always the case and the secondary shock propagates with different average absolute speed than the primary shock.

Shock motion was assessed by tracking the refractive index disturbance as it moved along the horizon (level to within a few pixels). Multiple data points were collected for both primary and secondary shocks in each event where secondary shocks could be observed. Linear fits for the  $x$ -position of the disturbance to frame number were highly correlated, indicating that the disturbance propagated with nearly constant speed. As will be explained shortly, this linear relationship is, in part, the result of the viewing angle of the camera. Other fits i.e. second or third-order polynomials did have slightly

improved correlation but the linear fits were used to simplify the velocity comparisons.

Figures 26 and 27 are examples of the position versus time data for a single event.

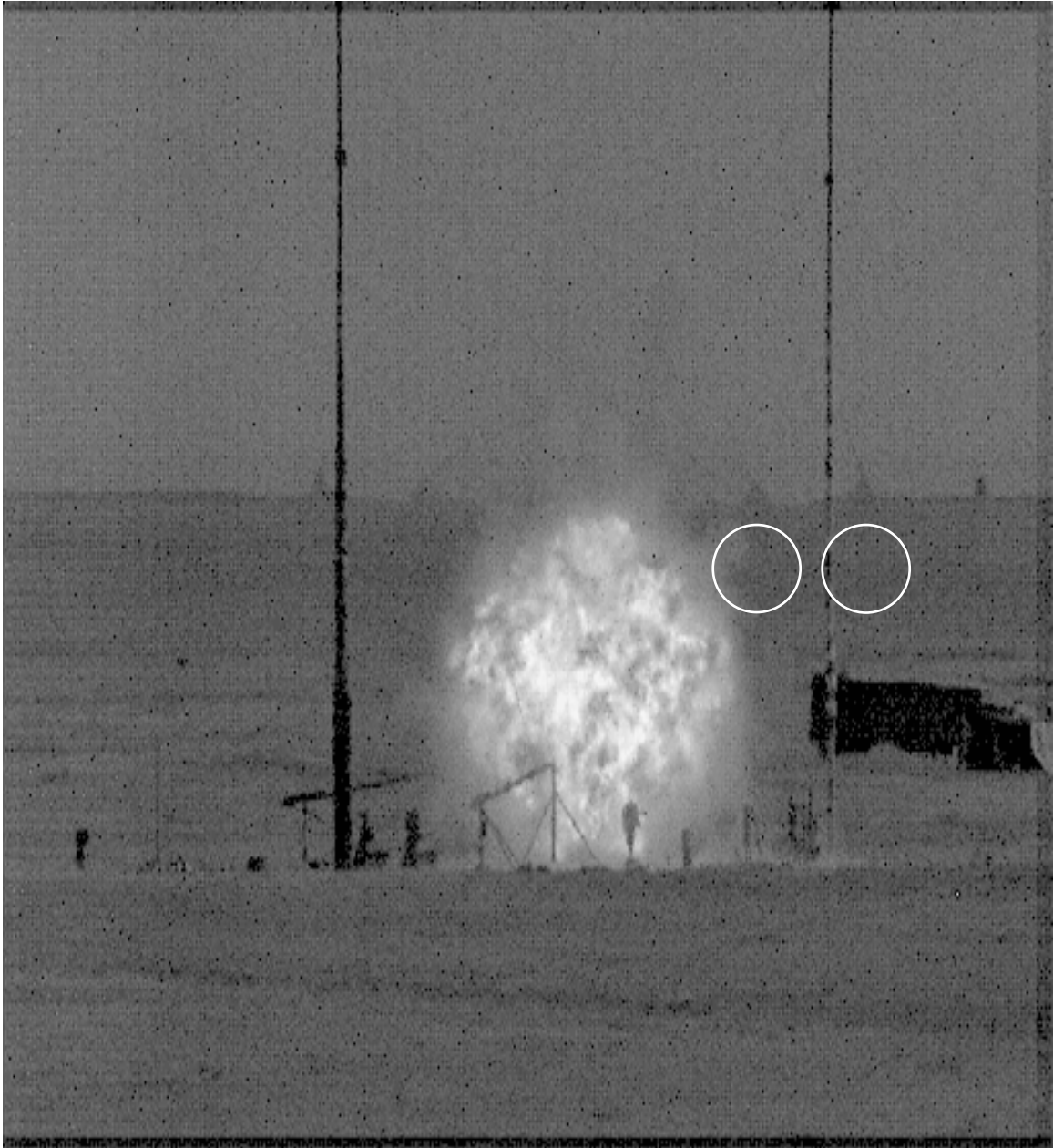


Figure 25. Primary and secondary shocks for NL2 event 3. The positions of the shocks along the horizon are visible due to the change in the index of refraction. The primary shock (right circle) lies outside the span of the two vertical poles, while the secondary shock (left circle) lies within. Contrast and Gamma have been modified to enhance the image.

Uncertainties in the individual position measurements were approximately  $\pm 3$  pixels on average. These uncertainties, due to operator error and low target contrast, accumulated randomly and, as a result, did not significantly affect the individual fit. Assuming that the expansion of a shock is symmetrical about its origin, the leftward and rightward disturbance motions should be identical. Therefore, the reported mean speed, in meters per frame (m/f), is taken to be the mean of the slopes of the left and right fit-lines, and the uncertainty is the difference between the mean and either of its two component slopes.

The difference of the mean speeds calculated from the event shown in Figures 26 and 27 is small (on the order of 0.0015 m/f (1.8 %) of either of the mean speeds) but is still greater than the 0.0007 m/f (1.02%) uncertainty for the mean of the secondary shockwave propagation speed. Mean differences and uncertainties vary widely throughout the data set but for eight out of the ten events, the differences in mean speeds of the primary and secondary shocks exceed the uncertainties in those means. It is not known how much of this difference is attributable to the difference in energy between the two shocks, and how much is attributable to a change of propagation media due to the passage of the primary shock. These data are given in Table 9. One should also note that the reported speeds are not the true speeds of the shock front due to the vertical separation of the detonation origin from the horizon, as seen by the camera (Ref. figures 4 and 25). Instantaneously, the speed of the index gradient along the horizon is the projection of the shock-front propagation vector onto the horizon. Nonetheless, reported

speeds still serve as a valid metric for comparison under the assumption that the origin was common to the primary and secondary detonations.

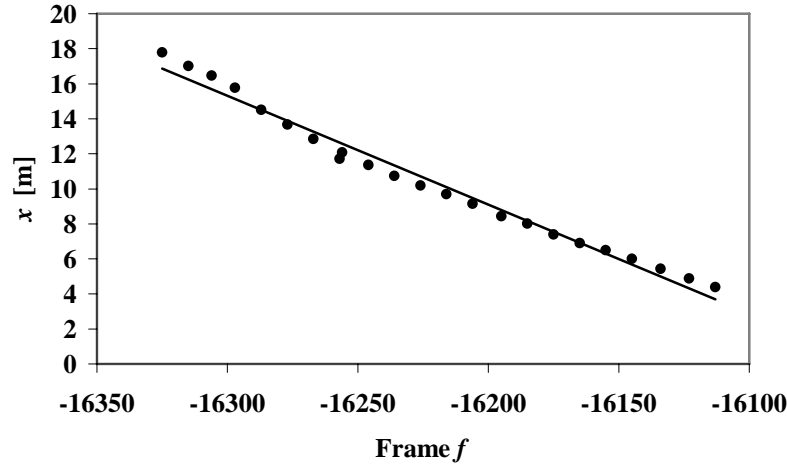


Figure 26. Motion of refractive index disturbance along the horizon for the leftward propagation of the primary shock in NL2 event 2. The regression line follows the relation  $x = -0.0621 f - 997.24$ , with  $R^2 = 0.9824$ . The slope of the regression line is the velocity of the disturbance in meters per frame. The negative sign indicates that the frames were captured prior to trigger (a manual post-event trigger was utilized).

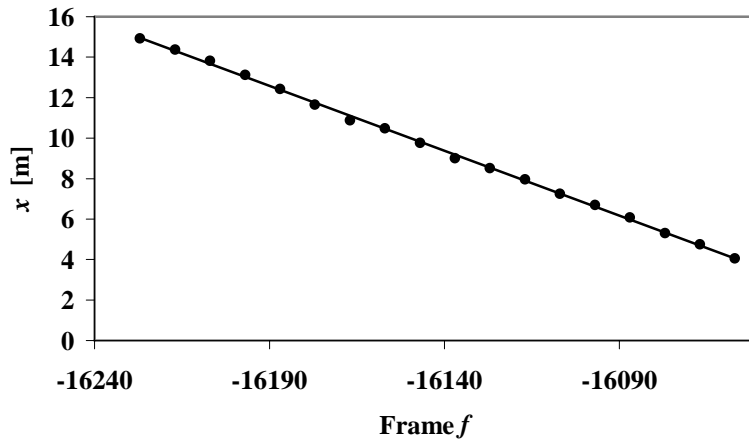


Figure 27. Motion of refractive index disturbance along the horizon for the leftward propagation of the secondary shock in NL2 event 2. The regression line follows the relation  $x = -0.0641 f - 1025.1$ , with  $R^2 = 0.9992$ . The slope of the regression line is the velocity of the disturbance in meters per frame.



Table 9. Speeds of the primary and secondary shock, speed differences between the primary and secondary shock, and uncertainties. All events were part of NL2. A negative sign in the second-to-last column indicates that the velocity difference between the two shocks is within the uncertainty in the velocity of the primary shock.

Event	Frame interval ( $\mu$ s)	Primary speed (m/f)	Primary uncertainty (m/f)	Secondary speed (m/f)	Secondary uncertainty (m/f)	$\Delta C$ (Secondary - Primary) (m/f)	$\Delta C$ - Primary uncertainty (m/f)	$\Delta C$ - secondary uncertainty (m/f)
2	100	0.0623	0.0002	0.0635	0.0007	0.0012	0.0010	0.0005
3	208	0.1104	0.0014	0.1115	0.0004	0.0011	-0.0003	0.0007
4	100	0.1047	0.0017	0.1151	0.0008	0.0104	0.0087	0.0096
5	100	0.0491	0.0003	0.0569	0.0015	0.0078	0.0075	0.0063
6	100	0.0568	0.0001	0.0607	0.0003	0.0039	0.0038	0.0036
8	100	0.0444	0.0001	0.0575	0.0011	0.0131	0.0130	0.0120
9	100	0.0449	0.0004	0.0596	0.0013	0.0147	0.0143	0.0134
10	100	0.0543	0.0016	0.0558	0.0013	0.0015	-0.0001	0.0002
17	100	0.0535	0.0010	0.0500	0.0020	-0.0035	0.0025	0.0015
21	100	0.0689	0.0026	0.0605	0.0050	-0.0084	0.0058	0.0034

## Opacity

Figure 28 is a spliced image showing the explosive charge (blurred object in the white circle) before and during detonation. Unfortunately, the explosive charge is much more difficult to identify in still imagery than in video footage, as a consequence of the low contrast. This also shows up as the dark spot at the center of the blast in the images that comprise Figure 24. Secondary detonations occur when the reflected shock reaches the remaining suspended explosive. The opacity of the flame region of a detonation fireball is not well characterized but it is assumed that the fireball is optically thick. While this assumption may be correct, in a statistical sense, the imagery shows qualitatively at least, that it does not always hold.



Figure 28. NL2 event 3. Before-detonation (left) and during-detonation (right) spliced images showing the suspended explosive charge (centered in the white circle) still visible in the center of the fireball after the primary detonation has occurred. The images have not otherwise been altered.

### 3.2.3 Muzzle flash data

Comparison of the different muzzle flash events is shown in Figures 29-32, in which the mean and standard deviation for each color in a single frame of each event are

plotted on separate axes. The mean values are indicative of the relative brightness while the standard deviations represent a first order approximation of the distribution of pixel values. This produces a qualitative picture of the clustering of the data. The increased clumping in the data from red to blue is attributed to the fact that most of the events radiated primarily at longer wavelengths, producing less overall variation at shorter wavelengths.

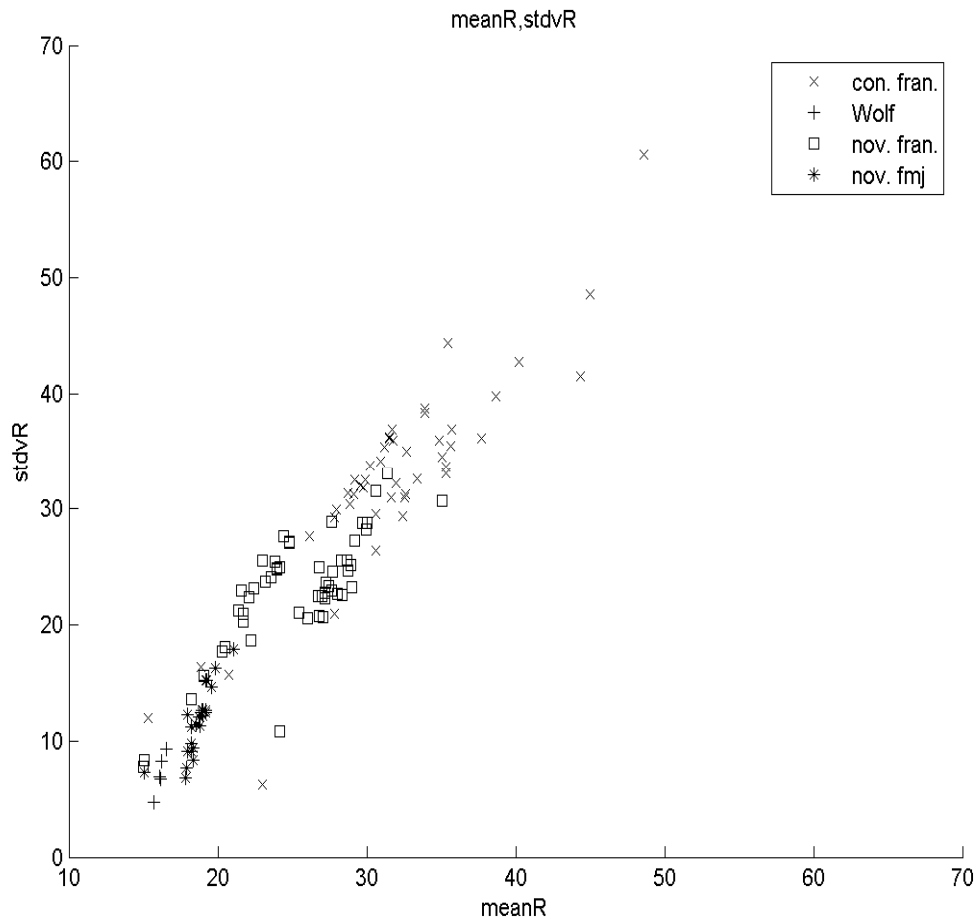


Figure 29. Scatter plot of the mean red value of each event versus the standard deviation of the red values for each event. Values are derived from an 8-bit (0-255) color scale. Symbols are defined according to the legend in the upper right, where *con* stands for conventional, *fran* for frangible, *nov* for novel, and *fmj* for full metal jacket.

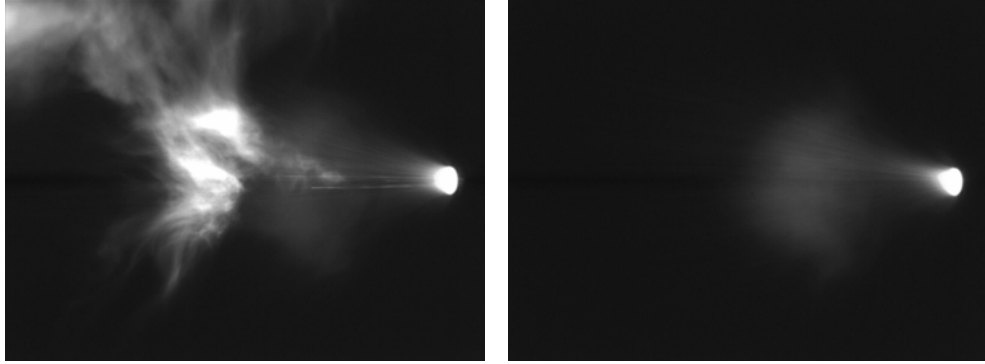


Figure 30. Comparison of the flashes created by two separate conventional rounds.

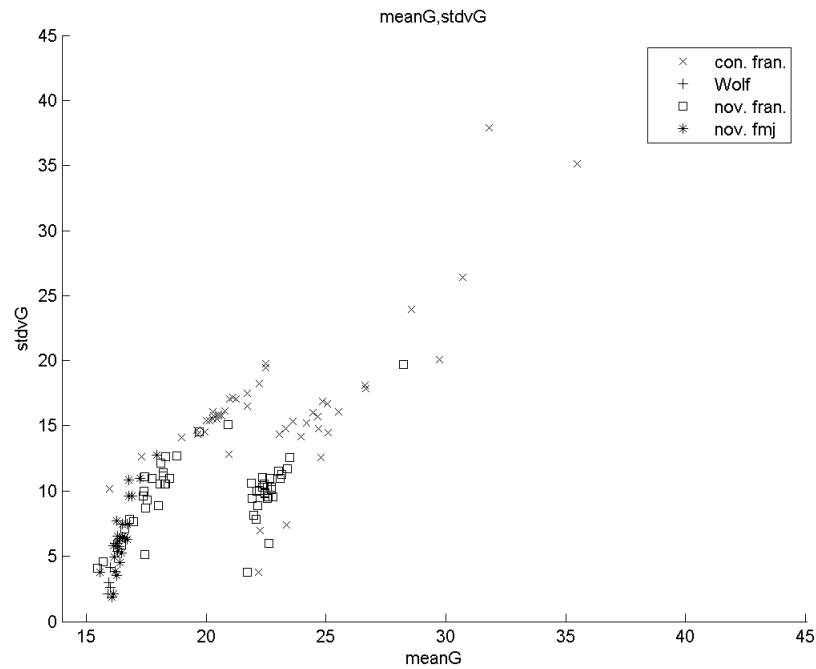


Figure 31. Same as Figure 29 but for green.

The separation of the data is attributed to the gun barrel opening, which was always illuminated, and the presence or absence of a cloud. The expected degree of clustering among munitions of the same type, denoted by their respective symbols was not observed, although there does appear to be a trend from lower left to upper right,

indicating an increase in relative brightness. The Wolf ammunition was the dimmest and had the lowest variability while the conventional frangible ammunition was the brightest, with the highest variability, as seen in figure 30.

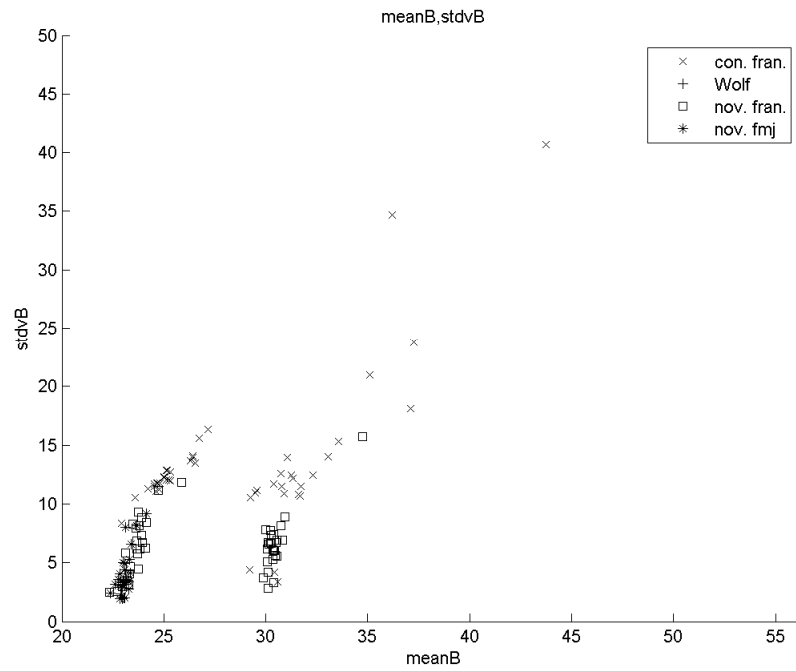


Figure 32. Same as Figure 29 but for blue.

## 4. Discussion

### 4.1 Vortices

Vortex diameters varied from about 0.15, to 0.9 meters—less than an order of magnitude. The spectral range that this encompasses is not known but it is assumed that these are the largest vortices (smallest wavenumbers), based on their measurability. The previous assumption justifies the assertion that the fitted function, shown in Figure 21, gives the rate at which energy was assimilated into the energy cascade at the small wavenumber end. Necessarily, dissipation must occur at the same rate by the large wave number components in accordance with equation (27) in 1.3.3.

As indicated in Figure 33, there was also virtually zero correlation between vortex radius and time of appearance, implying that the length scale of energy assimilation was approximately independent of time (i.e. that the scale of the largest vortices was approximately constant, hence the absence of a temporal correlation). The observed scale invariance is analogous to that generated behind a hypothetical turbulence grid, where length scale depends on solely on grid size and not flow parameters (4:361). This scale invariance is only present at one end of the spectrum.

As a consequence of the direct dependence of viscosity on temperature, the ensuing relationship between Reynolds number and temperature is inverse; and higher temperatures yield lower Reynolds numbers. However, Reynolds numbers for air, in relatively small pipes, can be very high, on the order of  $10^6$  even at modest velocities of 50 m/s (17:22). Thus, even with an increase in temperature, it is assumed that Reynolds numbers near the fireball are initially high due to the high flow velocities. An order of

magnitude estimate for air in the vicinity of a detonation is  $1.16 \cdot 10^7$ , assuming a fireball temperature of 1800 K, a flow velocity of 700 m/s and a length scale of 1 m. While the Reynolds number may decrease with time, if it remains in excess of the critical value, turbulence production occurs with a constant characteristic length. This length and its inverse are taken to be the diameter and wavenumber of the measured vortices, respectively. While assimilation length-scales are constant, any change in viscosity affects the scale of dissipation according to equation (27) in 1.3.3. Heating of the air, in the vicinity of the fireball, raises the viscosity, which has the effect of compressing the wavenumber spectrum from the large wavenumber end (17:317).

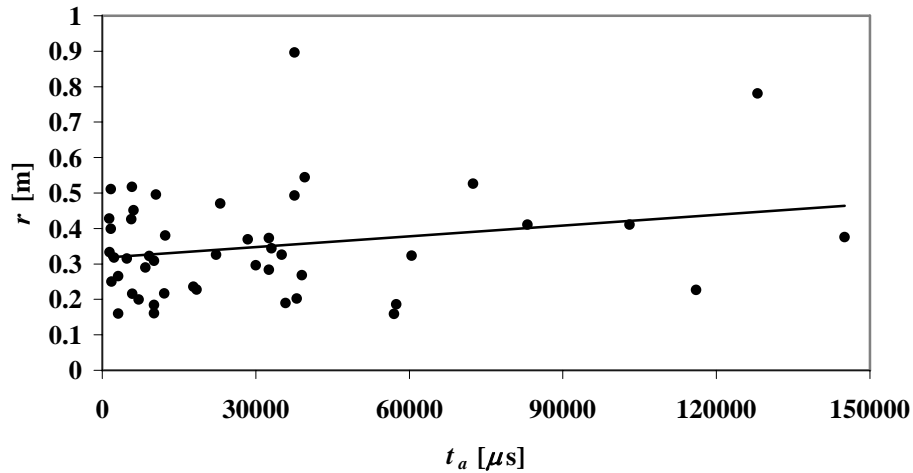


Figure 33. Scatter plot of diameter and time of initial observation. A weak trend toward increasing vortex dimensions is evident but the data is highly uncorrelated, with  $R^2 = 0.0547$ .

As the gas motions near the fireball decrease with increasing time, the energy available to drive the turbulent cascade decreases. Not surprisingly, in reference to the plot of appearance time versus appearance time (Figure 9), it has been observed that the number of active (large) vortices also diminishes with time. The energy dissipation is

therefore present throughout the fluid as a whole as well as at the level of individual vortices. A possible mechanical explanation for this behavior is that the increase in the dissipation length-scale causes a corresponding decrease in the maximum number density of the dissipation vortices for a particular space. Larger dissipation vortices may individually transfer more thermal energy to the fluid than smaller dissipation vortices but their decreased number has the effect of reducing the total active surface area available for dissipation in an equivalent space. While the rate at which energy is assimilated into the cascade decreases with time, so too does the rate at which it dissipates through fluidic heating, thus preserving the requisite balance.

#### **4.1.1 Further speculation**

The phenomenon of spectral compression offers another possible means to understand the power relationship for the individual vortices. It follows that a reduction in spectral (wavenumber) space, owing to an increase in viscosity of the fluid, corresponds a longer dissipation time. This is loosely analogous to the relationship between pulse length and spectral mode width in optics. A decrease in the energy assimilation rate is offset by a decrease in dissipation rate, with dissipation occurring at smaller wavenumbers. As a result, vortices last longer even though they have less energy, and are driven with less power, consistent with Figures 10, 15, and 21.

Additional justification for these ideas becomes evident when one considers, independently, the correlations between the duration or the energy of a vortex and the time it appeared. These are given in Figures 15 and 17, respectively. The term for energy  $r^2\omega^2$  includes, intrinsically, information about the length-scale of turbulent energy



production, which is of the order  $r_0$ , having wavenumber  $k_0 = 1/r_0$ . Similarly, the duration  $\Delta t$  is proportional to the inverse of the spectral width  $\Delta k$ . Separately, these parameters show definite correlation with the time after detonation but their mutual inclusion into the term for power guarantees a stronger correlation due to the completeness of the spectral information. It should be noted that there is no physical justification for the inferred relationship between  $\Delta t$  and  $\Delta k$  other than the apparent dependence of several correlations on the inclusion of the  $\Delta t$  term.

### **RMS Turbulent Velocity Fluctuations**

It can be shown (4:358) that the root mean square (RMS) of the turbulent velocity fluctuations  $u'_{rms}$  is determined by

$$u'_{rms} = \left( 2 \int_{k_0}^{k_K} E dk \right)^{1/2} \approx 2 \frac{\epsilon_0^{1/3}}{k_0^{1/3}} \quad (34)$$

where  $k_K$ , the Kolmogorov wavenumber, is the large wavenumber cutoff of the spectrum. Substituting the measured vortex power for  $\epsilon_0$  and the inverse of the measured vortex radius for  $k_0$  returns the RMS turbulent velocity fluctuations associated with the vortex. A scatter plot of this value versus time, for each vortex, results in the relationship presented in Figure 34. Of course, the values used to compute  $\epsilon_0$  and  $k_0$  are the same values that have been used throughout the previous analyses. However, it is telling that their apparent non-trivial combination, according to equation (34) was unforeseen. Furthermore, the correlation is unlikely random by virtue of its agreement with physical expectations, in that the RMS velocity fluctuations show a rapid decrease with respect to time and lie between seemingly reasonable upper and lower bounds.

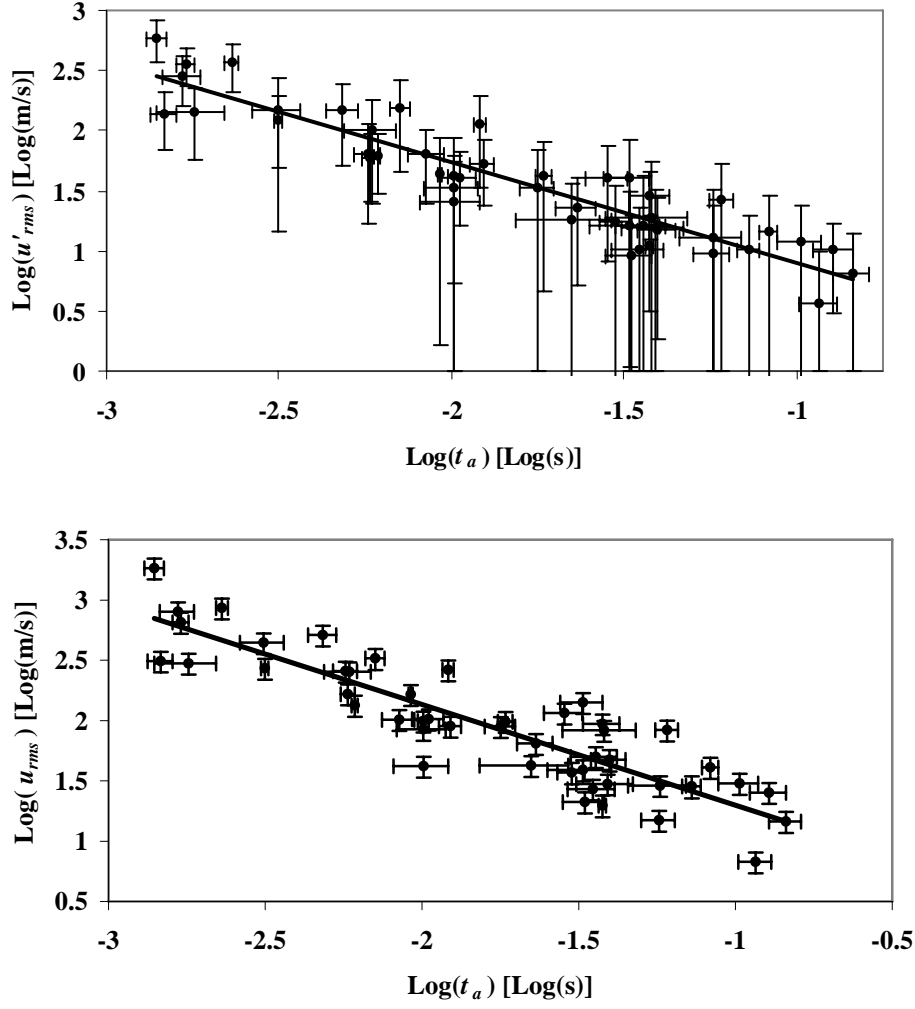


Figure 34. Top:  $\text{Log}_{10}\text{-Log}_{10}$  relationship between  $u'_{rms}$  and time of vortex appearance computed using the distributed (average) power  $W$ . The regression line is given by  $\text{Log } u'_{rms} = -0.837 \text{ Log } t_a + 0.0647$ , with  $R^2 = 0.8559$ . Bottom:  $\text{Log}_{10}\text{-Log}_{10}$  relationship between  $u'_{rms}$  and time of vortex appearance computed using instantaneous power  $Y$ . The regression line is given by  $\text{Log } u'_{rms} = -0.8355 \text{ Log } t_a + 0.462$ , with  $R^2 = 0.7889$ .

## Reynolds Number

Given (34), an alternate definition of Reynolds number (4:358) is forthcoming as

$$\text{Re} = \frac{u'_{rms}}{k_0 \nu} \approx 2 \frac{k_K^{4/3}}{k_0^{4/3}} \quad (35)$$

Sufficient information exists to find  $k_K$  upon introduction of the assumption, previously stated, that  $\Delta k$  is inversely proportional to  $\Delta t$ . The proportionality constant is chosen, arbitrarily through unit analysis, to be  $\eta u'_{rms}$ , where  $\eta$  is, as yet, undetermined with units  $[T]^2[L]^{-2}$  (inverse of mass-specific energy), and a value on the order of 30; whereby

$$k_K = \frac{\eta \cdot u'_{rms}}{\Delta t} + k_0 \approx \frac{\eta \cdot u'_{rms}}{\Delta t} \quad (36a)$$

An alternative and physically justifiable definition of the  $k_K$  is given in (36b)

$$k_K = \left( \frac{v^3}{Y} \right)^{-1/4} \quad (36b)$$

The approximation in equatuion (36a) ensues from the fact that, typically,  $k_K \gg k_0$  (4:358). With  $k_K$  now defined by the measured vortex parameters, a scatter plot of Reynolds number as a function of time may be generated according to equation (35). This relationship is given in the upper plot of Figure 35.

The lower plot in figure 35 shows the Reynolds number-time relationship computed using physically justifiable calculations for instantaneous input power and  $k_K$ . However, the correlation is significantly weaker than that for the upper plot, again demonstrating the physical significance of  $\Delta t$ . Additionally, determination of  $v$  in equation (36b) is contingent on the assumptions of a gas temperature and composition for the fireball; in this case 1800 K and dry air, respectively. While the existence of  $\eta$  is pure speculation, Reynolds numbers derived from equation (36a) exhibit the proper trend with time, and fit more closely with the observed data than those using equation (36b).

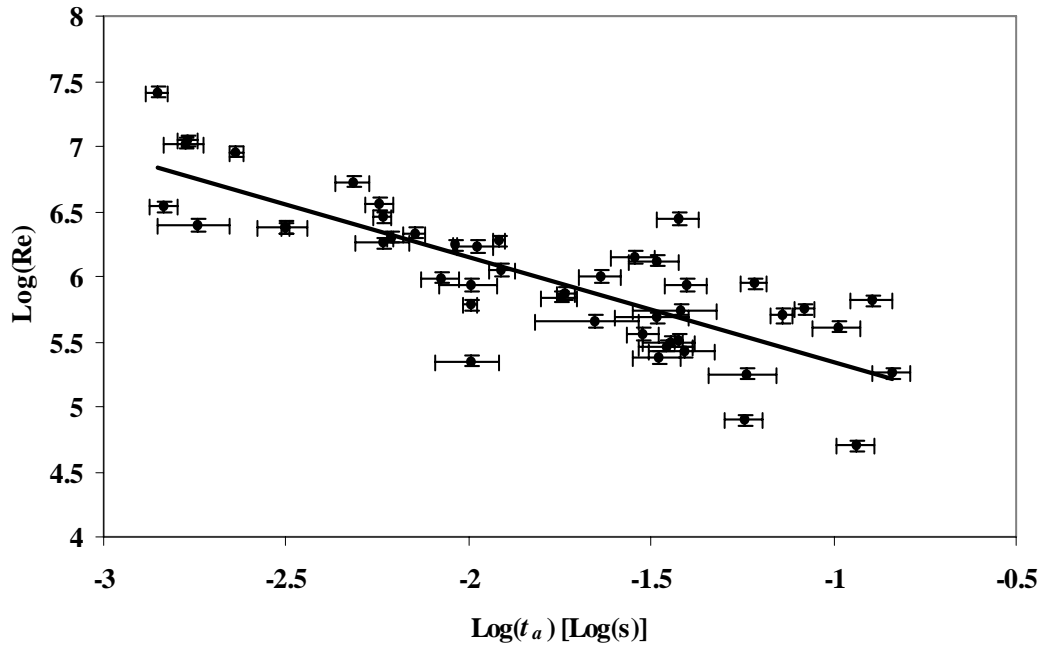
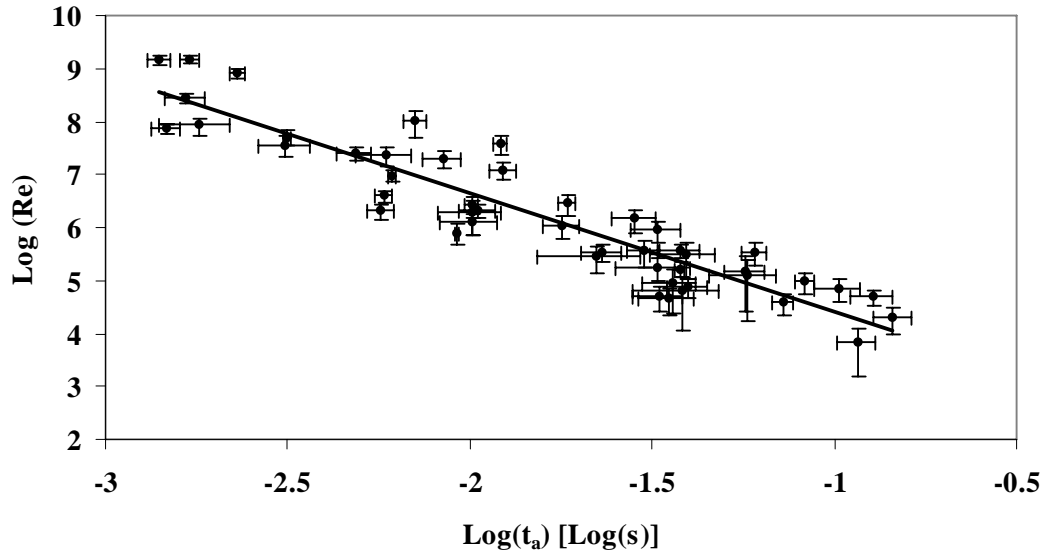


Figure 35. Top:  $\text{Log}_{10}\text{-Log}_{10}$  relationship between Reynolds number and time calculated using equation 36a. The regression line is given by  $\text{Log } Re = -2.2362 \text{ Log } t_a + 2.1864$ , with  $R^2 = 0.8579$ . Bottom:  $\text{Log}_{10}\text{-Log}_{10}$  relationship between Reynolds number and time calculated using equation 36b. The regression line is given by  $\text{Log } Re = -0.8049 \text{ Log } t_a + 4.5455$ , with  $R^2 = 0.6601$

## 4.2 Reflected and secondary shocks, and secondary detonations

These shall be treated together owing to the less extensive analysis as compared with the vortices and the innate similarities in the physics behind them.

### 4.2.1 Reflected Shocks

Treatment of reflected shocks may be found in Landau and Lifshitz but the derivations are heretofore unnecessary. The important result is that strong shocks in air will undergo regular reflection from a solid surface provided the angle between the propagation velocity vector and the surface normal does not exceed  $40^\circ$  (12:412). Given that portions of the shocks in the observed data were traveling parallel to the surface normal, the observation of shock reflection is most likely valid. The existence of this shock reflection is particularly interesting however, because it can be seen propagating backward through the fireball, behind the primary front. Owing to the dependence of shock velocity on the thermodynamic properties, particularly the adiabatic exponent, of the propagation medium, deduction of those properties becomes possible if the reflected shock velocity  $C_R$  is known.

Using equation (24), and its associated equations for the other state variables, one may derive the pressure, temperature, density, and flow velocity for the gas at any fraction of the primary shock radius, as was done by Zel'dovich (20:96). This can be accomplished without any reference to the velocity of a reflected shock traveling behind the primary shock. However, in the region of the fireball, the validity of the state variable values computed using the primary shock is uncertain. Knowledge only of reflected shock velocity is insufficient to derive any further thermodynamic information respecting

the propagation medium, as is clear from equation (16). Upon determination of the energy that was initially released into the primary shock, equation (23) could be of some utility, though there is a much simpler path that rests on a few additional assumptions. At this point it becomes important to clearly define the problem before continuing.

Consider two infinite, planar shockwaves, one being a distance  $d$  ahead the other, with parallel propagation velocities or, likewise, stationary with parallel fluid flows. The reference frame is constructed such that the trailing shock is at position  $x = 0$ . These two shocks now divide space into three regions. Region I, defined as  $x > d$ , lies ahead of the lead shock at  $x = d$  and has parameters  $p$ ,  $\rho$ , and  $u$ , consistent with the theory derived in 1.3.2. Region II, where  $0 < x < d$ , lies between the two shocks, sequential to Region I in the direction of the flow with parameters  $p'(x)$ ,  $\rho'(x)$ , and  $u'(x)$ . Region III, where  $x < 0$ , is then downstream from the second shock with parameters  $p''(x)$ ,  $\rho''(x)$ , and  $u''(x)$ . This situation may now be generalized to include two (approximately) spherical, concentric shocks, where the trailing shock, at  $x=0$ , becomes the reflection. Although  $\gamma$  is normally said to be constant, in the region of the fireball  $\gamma$  must change due to the explosive products and high temperatures; therefore,  $\gamma$  is now taken as  $\gamma'$  in Region II.

It has already been assumed, in the original derivation of the shock velocity that the lead shock is strong, i.e. that the pressure difference across the shock front is large (20:93); accordingly:

$$p'(d^-) - p \approx p'(d^-) \text{ or } p \ll p'(d^-), \quad (37)$$

where the superscript  $(-)$  indicates the negative side of the discontinuity. The new assumptions become: 1) the energy associated with the primary shock was conserved

during reflection; 2) the reflected shock is strong relative to Region II; and 3) that  $d$  is large enough to allow  $u' \approx -C_R$  at  $x = 0$ . It now stands to reason that

$$p''(0^-) - p'(0^+) \approx p''(0^-) \text{ or } p'(0^+) \ll p''(0^-) \quad (38)$$

There is also an expectation of  $p'(0^+) \leq p$ , mutually consistent with equation (24) and the fact that the fireball was no longer expanding when measurements of the reflected shock velocity were made. Conservation of energy now requires

$$p''(0^-) \approx p'(d^-) \quad (39)$$

Applying these same arguments to the density allows one to write an approximate equality for the mass-specific energies immediately behind both shocks, giving

$$\frac{p'}{\rho'} \approx \frac{p''}{\rho''}, \quad (40)$$

and thereby eliminating the necessity for computation of pressure or density in Region II.

Upon coupling this result with equations (20) and (21), algebraic manipulation finds

$$\frac{u^2}{u'(0)^2} = \frac{(\gamma' - 1)(\gamma + 1)^2}{(\gamma - 1)(\gamma' + 1)^2} \quad (41)$$

This leads to the simple quadratic equation in  $\gamma'$ :

$$a\gamma'^2 + (2a - 1)\gamma' + a + 1 = 0, \quad (42)$$

Where  $a$  is constant formed from the known values  $\gamma$ ,  $u$ , and  $u'$ , given by

$$a = \frac{u^2}{u'^2} \frac{(\gamma - 1)}{(\gamma + 1)^2} \quad (43)$$

Thus

$$\gamma' = \frac{(1 - 2a) \pm \sqrt{(2a - 1)^2 - 4a(a + 1)}}{2a} \quad (44)$$

The existence of two solutions is not understood, in a physical sense, but the negative radical returns the most realistic results. These are displayed in Table 10. Values of  $\gamma$  ranged between 1.08 and 1.3, with a mean value of 1.16 and a standard deviation of 0.06 over the 15 data points. It must be noted that there is one obvious discrepancy in equation (39). That formula predicts equality of the primary and reflected shock velocities if  $\gamma$  is constant and it is uncertain what errors this introduces into the computations of  $\gamma$ .

Table 10. Values of  $\gamma$  for their respective events and times.  $\gamma_-$  is taken to be the physically meaningful solution. The mean value of  $\gamma_-$  is approximately 1.16 with a standard deviation of 0.06 over the 15 data points.

Event	Initial observation time ( $\mu$ s)	Final observation time ( $\mu$ s)	Reflected shock mean velocity (m/s)	Primary shock mean velocity (m/s)		$\gamma_-$	$\gamma_-$ uncertainty
322dat01	5730	6530	868	520	37.0	1.11	0.0330
322dat03	10800	12700	815	433	47.8	1.09	0.0140
322dat15	7600	10200	534	397	22.9	1.18	0.0520
322dat52	5750	6740	708	421	37.5	1.11	0.0940
322dat54	5630	7500	798	442	43.9	1.09	0.0250
322dat57	5880	6620	920	556	36.3	1.11	0.0370
322dat59	6990	8230	759	526	26.8	1.16	0.0650
322dat61	4880	7770	726	427	38.4	1.11	0.0220
322dat65	4550	7290	631	422	29.0	1.14	0.0420
192dat02	5200	6200	742	530	25.1	1.17	0.0660
192dat03	2710	4790	734	596	18.6	1.23	0.0710
192dat04	4200	5200	613	483	20.0	1.21	0.0540
192dat05	2700	4700	823	645	20.3	1.21	0.0340
192dat06	4900	6900	778	696	14.7	1.29	0.0260
192dat13	3500	5500	895	672	22.4	1.19	0.0320

The mean measurement time  $t_m$  is defined as

$$t_m = t_i + \frac{(t_f - t_i)}{2}, \quad (45)$$

where  $t_i$  is the initial time, listed in the second column of table Table 10, and  $t_f$  is the



final time, listed in the third column. A weak quadratic correlation appears to exist between  $\gamma$  and  $t_m$ , as indicated in Figure 36. A similar correlation exists for the positive solution as well but its display is omitted here. This trend is the reverse of what is expected, in that  $\gamma$  is moving farther away from, rather than returning to its nominal value of 1.4. However, the fitted curve predicts a minimum  $\gamma$  of 1.1 at a time of 11 milliseconds, followed by a return to higher  $\gamma$  thereafter. The increase can not continue ad infinitum, of course, and  $\gamma$  must eventually stabilize at its atmospheric value. Implied is the fact that the quadratic behavior can only be valid over some finite (short) time interval.

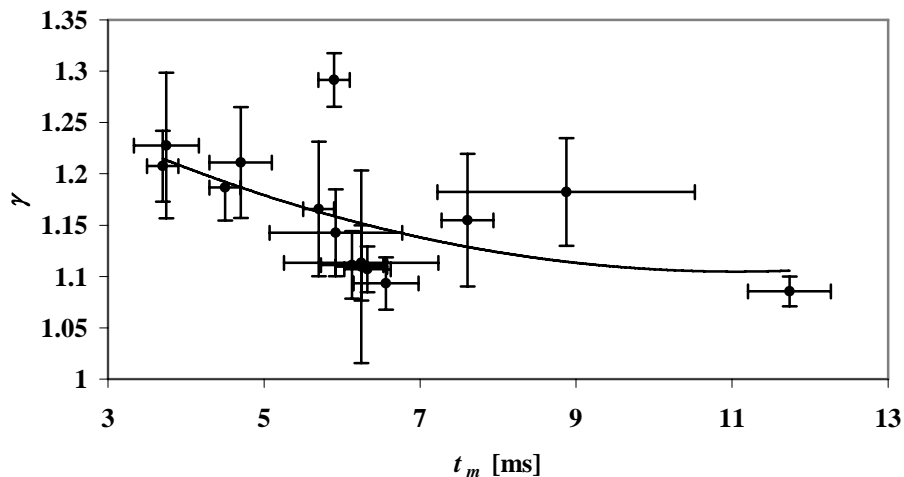


Figure 36. Correlation between  $\gamma$  and time of measurement. The regression curve is determined by  $\gamma = 0.002 t_m^2 - 0.045 t_m + 1.3534$  with  $R^2 = 0.2916$ .

It is entirely possible that the quadratic relationship is coincidental based on the small correlation coefficient but, should this not be the case, then it may be inferred that  $\gamma$  has a strong dependence on explosive type, or configuration due to differing chemical mechanisms. Omission of the outlying data point at approximate coordinates (6,1.3),

associated with event 192dat06 returns the relationship in Figure 37. Note that the value of the constant for the regression in the upper plot of figure 37 does the best job of predicting the correct  $\gamma$  at time  $t = 0$ . However, the cubic fit at the bottom of figure 37 may actually represent a more physically realistic behavior for  $\gamma$ , given the evolution of chemical composition of the fireball and the dependence of  $\gamma$  on the presence of molecular vibrational states.

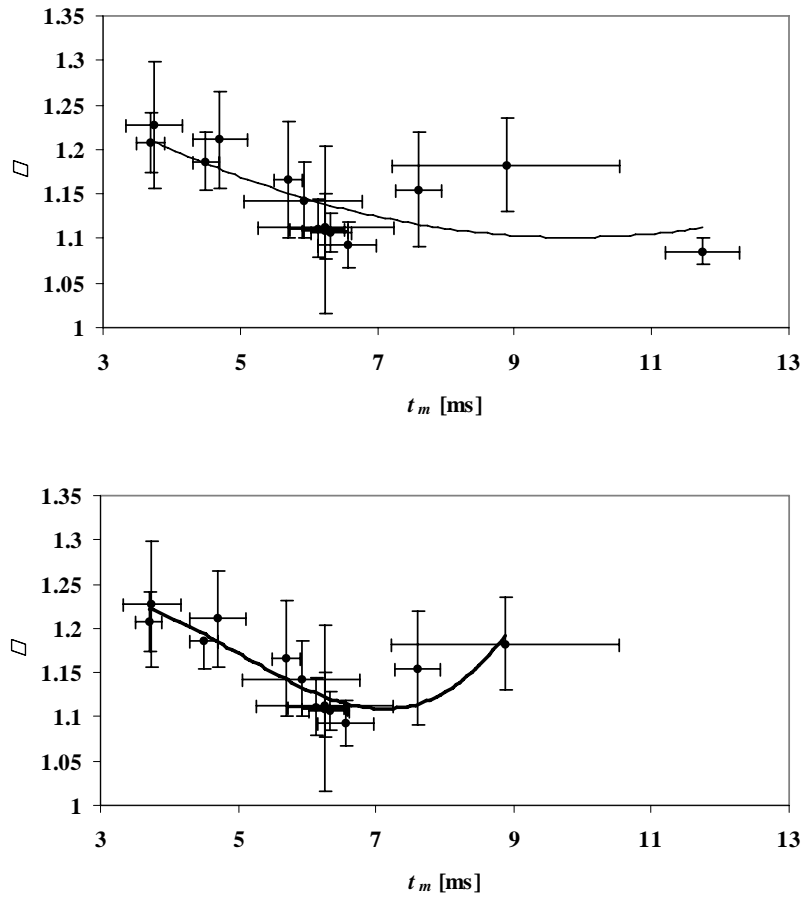


Figure 37. Top: Removal of one outlying data point at (6,1.3) from the original data shown in fig. 36 permits the new quadratic fit  $\gamma = 0.0029 t_m^2 - 0.0571 t_m + 1.382$ , and  $R^2 = 0.4953$ . Bottom: omission of a second outlying point at approximately (12,1.1) permits the cubic fit  $\gamma = 0.0033 t_m^3 - 0.05 t_m^2 + 0.2061 t_m + 0.9755$  and  $R^2 = 0.8198$ .

#### 4.2.2 Secondary detonations and secondary shocks

The observations of secondary detonations are important in that they justify the assumption that not all the explosive is consumed in the initial blast. Otherwise, at this point, the secondary detonations are little more than a curiosity. In fact, the term “secondary detonation” must not be taken for granted; it is subject to the qualification that knowledge of whether these events actually constitute detonations or deflagrations is uncertain. CJ theory permits this determination in the context of known state variables but the limited coincidence of secondary detonations and shock reflections precluded the requisite measurements. It may be possible, in such coincident cases, especially given the apparent linkage of both phenomena, that the method of the previous section could be used to compute the state variables and subsequently infer whether  $D$  is indicative of detonation or deflagration. This was not done here, and furthermore, the previous argument is not entirely complete in that a pressing question as to whether the fuel is dispersed throughout the fireball or whether it remains in a condensed, solid form has yet to be answered. Only one qualitative observation in NL2 event three points to the latter; whence, if this is the case for the other events, then “detonation” is a valid description. It follows that the measured velocities are the expansion rates of the secondary detonation products within the region of the first fireball. This is further supported by the qualitative observation of the subsequent emergence of the second shockwave, and thereby gives some measure of the inefficiency of the primary detonation event.

Comparisons of the primary and secondary shock velocities show that variations between the two are considerable, ranging between 0% and 30% but no correlation was

found to exist between the two velocities. It is suspected that the secondary shock contains less energy but may still propagate with greater velocity due to the change in medium resulting from the passage of the primary shock. This, however, has not been experimentally verified and cases may exist where the secondary shock is the more energetic of the two. Accordingly, the secondary shock possesses some utility for determination of the energy that went into the second detonation in a manner analogous to (18) and (19). However, the approach would involve considerably more difficulty due to the constantly changing medium behind the primary shock.

#### **4.2.3 Opacity**

There were two separate observations of apparent optical thinness in Yuma event 65 and NL2 event 3. However, that is only a frequency of about 4%, which is clearly too small to justify, on statistical grounds, that fireballs are regularly optically thin in the visible. There may, in fact, be more cases where the fireball is optically thin but looks optically thick due to saturation of the camera. Furthermore, in both cases where optical thinness was observed, the duration of that observation was very short, roughly a millisecond or so. This seems hardly long enough to be of any practical utility toward altering any previously employed assumptions, at least where visible spectra are concerned. It can, however be said with certainty that the fireball is optically thick or at least highly opaque by the time it reaches its end state. Ascertaining the degree of optical thinness between event initiation and the complete decay of the fireball will require data where instrument saturation has been avoided.

### 4.3 Spectral analysis

Multiple image processing techniques were used in an attempt to extract information from the Phantom camera's three integration bands. Virtually no analysis has been conducted, at this point. It is still worth mentioning that two of the techniques were decidedly more applicable than the others, based on the absence of excessive noise. Both involved simultaneous computation of the mean and the standard deviation for the array of values of each color in each frame. Plots of the ratios of the means for each unique combination of two colors and likewise for the standard deviations as functions of time (frame) gave clear representations of the temporal behavior of the particular event; these also easily distinguished the differences in that behavior among the three colors, as seen in Figure 38. The actual significance of those differences has yet to be ascertained.

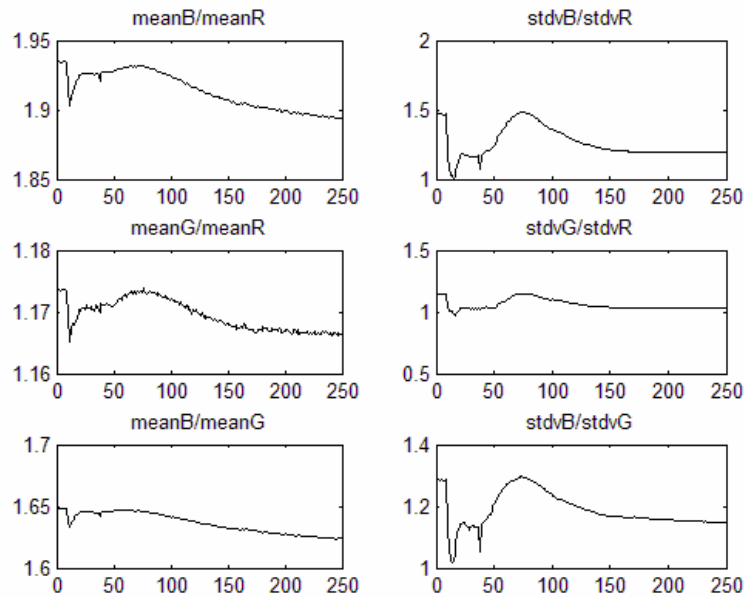


Figure 38. Plots of the ratios of mean and standard deviations of different colors as a function of frame number for Yuma event 46. R, G, and B refer to red, green, and blue respectively.

The second technique, a simple modification of the first, involved computation of coefficient of variation, defined as the ratio of the standard deviation to the mean, for the pixels in each color-band. Plots of these values as a function of time also revealed the relative temporal behavior of the event among the three colors. These behaviors were also found to be approximately consistent in both absolute and relative magnitude (e.g. red coefficient of variation > green coefficient of variation > blue coefficient of variation) across the entire 12-event sample. The consistency becomes apparent upon comparison of figures 39 and 40, which were generated from two different events.

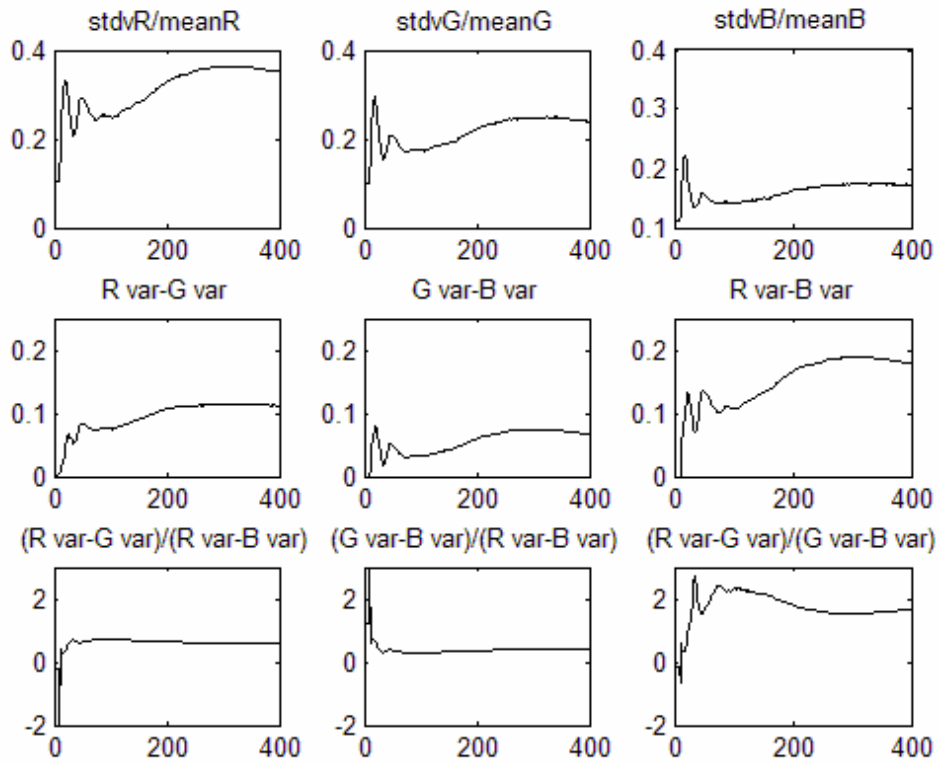


Figure 39. Plots of : 1) the coefficients of variation for red R, green G, and blue B (first row); 2) the differences of the coefficients for each unique combination of colors (second row), and 3) the three unique ratios of these differences (third row). The abscissae are in frame number. Plots are all generated from NL2 event 3.

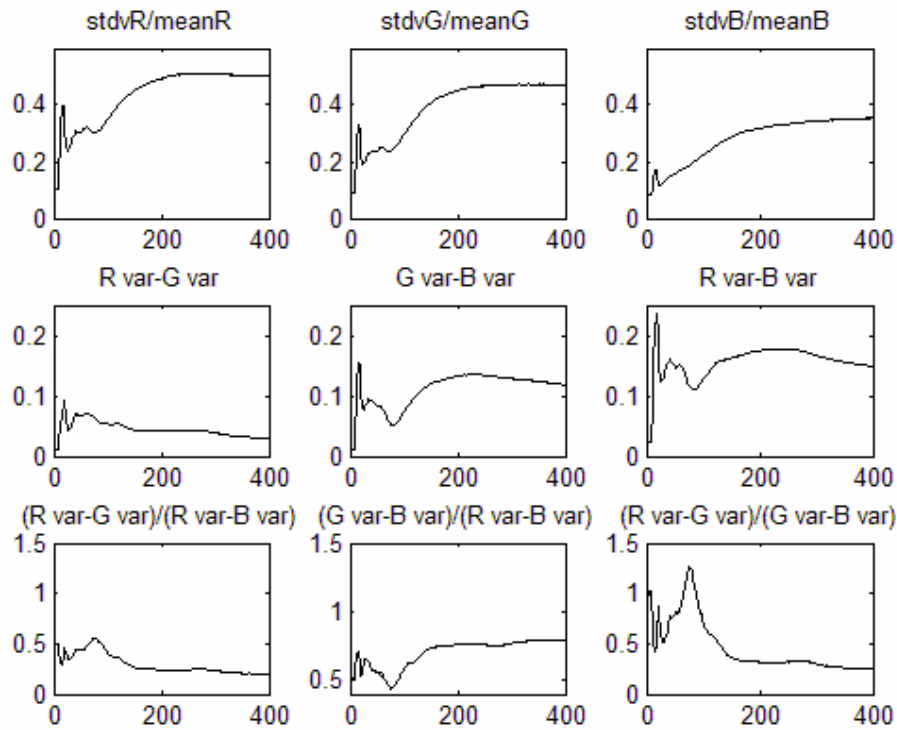


Figure 40. Plots for Yuma event 3. Parameters of each plot are the same as figure 4.3-2. Note the similarity, between the two events, in the magnitudes of the values and in the respective behavior of the three colors, such that  $R > G > B$ .

Consistency is unexpected as it demonstrates independence from the differences in camera settings, calibrations, and image processing throughout the 12 samples. This degree of robustness is important given that the precise influence of manipulations to the instrument and data on the relative behaviors of the colors is uncertain. However, quantitative bounds for this robustness in terms of the degree of manipulation have, so far, not been established.

#### 4.4 Muzzle Flash

All the other data, thus far, is derived from large explosive events with great variability among configuration, and explosive type, making assessment of

reproducibility impossible. The muzzle flash tests break this pattern and provide an opportunity to look at a relatively large number of small explosive events with much more controlled variability. Currently though, little more than qualitative statements can be made about the muzzle flash data. The most important realization is derived from the lack of separation among the different ammunition types in Figures 29, 31, and 32. Contrary to expectations, this appears to indicate a limited reproducibility among the different types, in visible wavelengths. The true degree of clustering has yet to be quantified but any clustering is, in general, not obvious. The trend from lower left to upper right in the red is indicative at least some separation but the amount of variation, especially among the conventional frangible rounds indicate that even small explosive events may not be highly reproducible, at least in terms of their brightness relative to one another. The images in Figure 30 give some indication as to how great this variability can be, even for small events. A final interesting observation is the relationship between the standard deviation and the mean for each event. In general this is linear, but the slope appears to vary among the three colors, implying that there may be some wavelength dependence to the variance of the muzzle flash radiance.



## 5. Conclusions and Recommendations

The muzzle flash and opacity topics have been omitted here as a result of insufficient analysis necessary to warrant definite conclusions. Generalized conclusions follow:

1. Several correlations were found to exist among parameters of turbulent vortices around detonation fireballs
2. The strength of the correlation for vortex power with time was found to differ for an instantaneous formulation of power and an average formulation, with  $R^2$  values of 0.7988 and 0.8572 respectively.
3. Vortex correlations demonstrated significant invariance with respect to explosive parameters for timescales on the order of 1 ms after detonation or greater.
4. It should be possible to use shockwave reflections to measure the adiabatic exponent  $\gamma$  in the interior of the fireball.
5. Measurements of  $\gamma$  relying on shock reflections were found to be variable, ranging between 1.08 and 1.3 and weakly correlated to time.
6. Observations of secondary detonations and secondary shockwaves confirm that significant explosive fuel remains after the initial detonation event.
7. Eight of the observed secondary shocks traveled with an absolute, lab-frame velocity equal to or greater than that of the primary shock. Two of the secondary shocks were slower.

8. The coefficient of variation is a useful metric for comparison of phantom-derived spectral data from multiple events.

## 5.1 Vortices

Several parameters of selected vortices were measured in events of the Yuma data set. These include maximum vortex radius, vortex rotation rate, initial time of observation, final time of observation, and vortex position with respect to detonation origin. Several measured vortex parameters were found to correlate well amongst themselves. These included angular speed versus time and length of observation versus angular speed. The length of observation of a vortex was also found to correlate with the final time of observation. Furthermore, the random selection of vortices, based on measurability criteria, reveals a temporal dependence to their number or a “temporal density.”

Additional correlations were discovered to exist between several physically meaningful combinations of vortex parameters, determined through unit analysis. These included vortex energy versus time, vortex gas pressure (resulting from angular acceleration) versus time, and vortex power versus time. Given the sample of 41 data points, nearly all the referenced correlations are strong, with an  $R^2$  in excess of 0.7. Furthermore, all the correlations are independent of the various explosive types, weights, configurations, and orientations used in the Yuma test.

The vortex correlations may be explained in terms of the turbulent energy spectrum. Energy is assimilated into a turbulent energy cascade at the large length scale (small wavenumber) of the observed vortices. The energy is then transmitted to

progressively smaller vortices, down to a length scale where the majority of dissipation occurs, through increases in thermal energy and entropy of the fluid; this scale is directly related to the fluid viscosity. Dissipation must balance assimilation, which is also directly related to viscosity at a given flow velocity. A decrease in the rate of energy input is then directly related to a compression of the spectrum from the dissipation length-scale (large wavenumber end). In mechanical terms, increased flow resistance forces dissipation to occur at larger length-scales; but this decreases the surface area available for dissipation. Consequently, the motions of the fluid persist for increasing lengths of time even though their energy is constantly decreasing. Intuitively, one would assume the converse and hold dissipation constant but the data clearly indicate that such is not the case. A more speculative spectral description of the observed behavior was presented in section 4. The spectral and mechanical formulations offer two perspectives for describing the same phenomenon.

The power as a function of time is representative of the rate of energy input into the turbulent energy spectrum. Two metrics for power, one involving an instantaneous rate and one a temporal average correlate very well with time, having  $R^2$  values of 0.7988 and 0.8572, respectively. The difference is attributable to the inclusion of vortex duration (longevity), used in the average metric, and may be a consequence of spectral information (i.e. the large and small wavenumbers) contained therein. The application of this theory produces realistic correlations for the RMS turbulent velocity fluctuations and Reynolds numbers with time. Again however, for reasons unknown, the correlations for both have significantly higher  $R^2$  values when the average power metric is used in their

computation. Predictions for RMS turbulent velocity values show a decreasing trend from about 500 m/s to 10 m/s over about 100 ms, while Reynolds numbers exhibit a decrease from  $10^9$  to  $10^3$  over the same time interval.

The degree of independence that the data seem to exhibit with respect to variability in ordinance corroborates the assumption that very little information, unique to the origins of an explosion persists for a significant length of time. According to these data and analyses, the window for obtaining unique information is something on the order of  $10^{-1}$  seconds. In truth, this value is probably a significant over-estimate, due to the appearance of such strong correlations, beginning with the earliest measurements at about  $10^{-3}$  seconds. Unfortunately, though, to look back any further in time would constitute nothing but guess-work. Turbulence, at least, does not seem to present itself as a viable feature for classification. However, the importance of these efforts is not entirely lost on the absence of useful features. The observations of changes in power, energy, and length-scales of dissipation are directly relatable to physical processes occurring inside the fireball and consequently, could be used to verify the results of other measurements.

## **5.2 Reflected Shocks**

Velocities and times of observation were recorded for reflections of the primary shock propagating through the fireball; these were compared with simultaneous measurements for the un-reflected primary shock. The results of this comparison show that the velocity of the shock reflection, inside the fireball, was significantly larger than the velocity of the un-reflected shock, over the same time interval. On average, the un-reflected portion was 69% slower for a simultaneous time interval. Such measurements

are useful in that they permit computations of the adiabatic exponent inside the fireball. However, these computations amount to spatial and temporal averages, owing to the nature of the data.

Values of the adiabatic exponents range from 1.08 to 1.3, with a mean of 1.16 and a standard deviation of 0.06. A very weak quadratic correlation, having an  $R^2$  value of 0.292, between the adiabatic exponent and time of measurement, relative to time of detonation, is also evident. This correlation was markedly improved to an  $R^2$  of 0.495 by the removal of one outlying data point. A cubic fit subsequent to the removal of a second outlying point may correspond better to physical expectations for the behavior of  $\gamma$  in a region of evolving chemical composition. However, the second regression function infers an adiabatic exponent of 1.38 at the time of detonation, which is nearest of the three to the value 1.4, assumed for air at room temperature.

The assumptions necessary to derive these values were contingent on idealizations but the seeming reasonability of the results implies that such assumptions were not wholly inaccurate. Much greater variability exists for the computed values of the adiabatic exponent than for any of the vorticity characteristics. Whether the technique employed measures a real physical feature is uncertain, but even in the absence of physical meaning, it may possess value as a classification tool. The observed variability warrants further investigation.

### **5.3 Secondary detonations and secondary shocks**

The very existence of these phenomena provides validation to the assumption that condensed explosives are not entirely or instantaneously consumed in the initial

detonation. The prominence of the secondary detonation and the emergence of the secondary shock further imply that a significant fraction of the fuel remains after the primary event. Propagations of the secondary shocks outside the fireball were recorded and compared to those of the primary shocks. Regressions for position versus time for both primary and secondary shocks returned linear relationships, whose slopes are taken to be the velocities. Relative velocities varied widely, with the difference ranging between 2% and 30% of the primary shock velocity; on average the difference is about 12%. For six out of the ten events, secondary shock velocities were the larger of the two. For two events, the velocities were equal to within the uncertainty in one of the velocity uncertainties larger, and for the remaining two events the primary shock velocity was larger. This velocity difference is assumed to be codependent on the quantity of fuel left over from the primary detonation and the medium behind the primary shock but these dependencies remain to be decoupled.

A final important feature is the trend of the disturbance propagation, whose linearity is peculiar, given the geometry of the system. Assuming spherical propagation, the shock-front normal is inclined with respect to the horizon due to the initial separation between the horizon and the explosive charge. The instantaneous horizon velocity is then the projection of the true velocity onto the horizon. As the angle between the shock-front normal and the horizon decreases with distance, the projected velocity approaches the true velocity. This implies that the true shock velocity is converging toward the horizon velocity of the index gradient determined by regression.

## **5.4 Spectral Analysis**

The spectral analysis was incomplete in that it did not permit any conclusions regarding phenomenology. Nonetheless, it has still been demonstrated that 1) there is a significant degree of structure and variability among the three colors, for the several events and 2) that at least one metric, the coefficient of variation, may be a practical means for making like-comparisons of different events. Both of these results could potentially be exploited in future work on classification.

## **5.5 Recommendations**

Thus far, turbulence has shown little variability in behavior with respect to detonations. However, this point can not be made definitively, as there is also plenty of room to increase the variability of the data set. The primary question to answer now is how well this invariability holds over the broadest possible range of explosive types and configurations. Even lacking variability, the most important aspect of this phenomenology is that it can be used to enhance models of the behavior of the fireball and thus supplement other measurements. It would be beneficial to identify some highly reproducible features of fireballs that can be used to justify or dismiss assumptions that are necessary to draw conclusions from other data sources. This should be the focus of any future efforts to understand detonation turbulence.

In contrast to turbulence, measurements of the adiabatic exponent, using the technique described previously, appear to have a high degree of variability. Whether or not the values are physically correct they may still provide a useful feature for classification. The next logical step is to investigate the temporal dependence of the

adiabatic exponent, inside the fireball. This may be accomplished simply by varying the distance of the detonation origin from the reflecting surface. Assuming a relatively constant shock propagation speed for a given explosive type, a profile of the adiabatic exponent inside the fireball, can be determined as a function of time. Again, this could be used to test any assumptions respecting fireball thermodynamics.

The same may be the case with the spectral analysis as well but so little has been done in this area that it is impossible to say what utility it might have. The techniques employed here have demonstrated some robustness with respect to manipulations of the data. This leads to the important realization that any observed variability between events is indicative of phenomenology. Furthermore, great distinction in the structure of different events has been observed and this should be looked at in greater detail. In regards to the specific question of obscuration of the hot parts of a fireball, one technique shows potential promise. Using the three Phantom color-bands, one may generate a  $3 \times N$  matrix containing the red, green, and blue values of a pixel for each frame of a video. Given Planckian behavior, it is expected that variations of the red, green, and blue values are not independent. Dependencies can be evaluated by taking the covariance of the pixel value matrix at sequential steps of some arbitrary number of frames. Subsequent comparisons of these variations to expectations of a cooling Planckian can determine the irradiant history of the pixel in question. Wide variation from Planckian would indicate obscuration. Of course, nighttime data would have to be analyzed to avoid corruptions from solar reflection.

The recommendations may be condensed as follows:



1. Determine the degree of invariability of the turbulence through a set of field experiments
2. Produce temporal profile of adiabatic exponent inside fireball
3. Use covariance of RGB pixels to measure fireball obscuration

## Appendix A-1: Phantom Camera Data



A PHOTO-SONICS COMPANY



LEADERS IN HIGH SPEED PHOTOGRAPHIC MOTION ANALYSIS SYSTEMS

### PHANTOM<sup>®</sup> v7 CAMERA



With a new high resolution sensor featuring incredible speed and the sensitivity to take advantage of 2  $\mu$ sec exposure times, the new Phantom<sup>®</sup> v7.0 raises the bar in digital high-speed camera performance. This is a true replacement for many high-speed film applications, including most 16mm rotating prism requirements. Long record times for missile launch and flight mission are now supported with a real time streaming output!

- SR-CMOS 800 x 600 pixel sensor, color or monochrome
- 4,800pps full frame, 10,000pps at 512 x 384 and 150,000 maximum
- 12 bit image depth for extended gray scale, 24, 36 or 48 bit color images
- Global (snap-shot) on-chip shuttering to 2 microseconds
- Auto Exposure control
- "EDR" Extended Dynamic Range exposure control
- IRIG-B timing, modulated or un-modulated, IRIG lock w/phase shift
- Continuous data streaming up to 2,000pps (8 bit), 1,500 pps (12 bit)
- Range Data Input
- Continuous color video output
- Automated multiple session recording for remote unmanned operation
- Rugged high-g configuration
- FireWire<sup>®</sup> (IEEE 1394) or RS232/422 serial digital control
- 10/100 Ethernet control
- 100% compatibility with Phantom<sup>®</sup> v4, v5 and v6 cameras

WE HAVE A WAY OF LOOKING AT THINGS!

## Appendix A-1: Phantom Camera Data

LEADERS IN HIGH SPEED PHOTOGRAPHIC MOTION ANALYSIS SYSTEMS

<p><b>Imager</b></p> <ul style="list-style-type: none"> <li>• Auto exposure</li> <li>• EDR Extended Dynamic Range™</li> </ul> <p><b>Standard features include:</b></p> <ul style="list-style-type: none"> <li>• High-G configuration</li> <li>• Continuous data streaming to 2000pps (3Q03)</li> <li>• Range Data Input</li> <li>• Continuous recording</li> <li>• Pre-trigger &amp; Post-trigger recording</li> <li>• On chip global shuttering</li> <li>• Strobe sync</li> <li>• Segmented integral image memory</li> <li>• Continuous color video output</li> <li>• IRIG-B timing capture w/ phase shift</li> <li>• FireWire™ digital interface</li> <li>• 10/100 Ethernet (1Gbit 2Q03)</li> </ul> <p><b>Sensor:</b> 12 Bit, 800 x 600 pixel SR-CMOS monochrome, or selectable 24, 36, or 48 bit color SR-CMOS array</p> <p><b>Sensitivity:</b> 4800 ISO/ASA monochrome, 1200 ISO/ASA color</p> <p><b>Pictures per Second (PPS):</b> Full sensor: to 4,800pps, or 512x384 to 10,000pps</p> <p><b>Allocated formats:</b> to 150,000pps with "CAR" (Continuously Adjustable Resolution) feature</p> <p><b>Exposure Time:</b> Variable, independent of sample rate (pps) to 2 µs (1 µs option)</p> <p><b>Triggering:</b> Continuously variable pre/post</p> <p><b>Imager Control:</b> Via FireWire™, 10/100 Ethernet, RS232/422 Serial (1Gbit Ethernet 2Q03)</p> <p><b>Preview and Focusing:</b> Via computer monitor or continuous video out</p> <p><b>Lens Mounts:</b> Nikon mount standard. Many other lens mounts available, including Photo-Sonics Hi-G type and C-mount</p> <p><b>INPUTS/OUTPUTS</b> (via integrated quick-release connectors):</p> <p><b>Trigger:</b> TTL pulse, or switch closure</p> <p><b>Sync Image:</b> TTL pulse</p> <p><b>Event Marker:</b> TTL pulse or switch closure</p> <p><b>Ready Signal:</b> TTL pulse</p> <p><b>IRIG-B Timing:</b> IRIG-B code, modulated or unmodulated input with IRIG-B output, lock and variable phase shift</p> <p><b>Range Data Input</b></p> <p><b>RS232</b></p> <p><b>Strobe Sync:</b> TTL pulse</p>	<p><b>Network:</b> Via FireWire™ digital interface (IEEE 1394) and 10/100 Ethernet (1 Gbit Ethernet available 2Q03)</p> <p><b>Video Out:</b> NTSC or PAL or Serial Digital Video (SDI)</p> <p><b>Power:</b> 28VDC/1.5 Amp</p> <p><b>MEMORY</b></p> <p><b>Standard:</b></p> <ul style="list-style-type: none"> <li>• 1024 MB integral image memory</li> <li>• Records 1,400 images for .3 sec of continuous recording at 4,800pps, full format.</li> <li>• Longer recording times for lower sample rates and allocated formats (for example, 14.4 sec at 100pps)</li> </ul> <p><b>Optional:</b></p> <ul style="list-style-type: none"> <li>• 2048 MB integral image memory continuously records 2,800 images (.6 sec) at 4,800pps full frame</li> <li>• 4096 MB option will record 5,600 full frame images (1.2 sec) at 4,800pps full frame</li> <li>• Non-Volatile Flash Memory, up to 4 GB (2Q03)</li> </ul> <p><b>Environmental</b></p> <ul style="list-style-type: none"> <li>• 100g up to 10 milliseconds</li> <li>• 50g up to 100 milliseconds</li> <li>• Three axis</li> </ul> <p><b>SOFTWARE</b></p> <p><i>Phantom® operates in a Windows™ environment with familiar commands found in familiar places. Standard functions include:</i></p> <p><b>Acquisition:</b></p> <ul style="list-style-type: none"> <li>• Image capture, IRIG-B timing capture &amp; standard time annotation</li> <li>• Field-of-view &amp; focus</li> <li>• Sample rate &amp; aspect ratio selection</li> <li>• Shutter speed</li> <li>• Histogram</li> <li>• Brightness &amp; contrast, gamma adjust</li> <li>• Trigger modes</li> <li>• Continuous record</li> <li>• Save &amp; recall setups</li> </ul> <p><b>Analytical playback:</b></p> <ul style="list-style-type: none"> <li>• Immediate playback of cine</li> <li>• Variable playback speeds in forward or reverse, including freeze frame and endless loop</li> <li>• Random Go-to-Image</li> <li>• View single images at random from any cine</li> </ul>	<ul style="list-style-type: none"> <li>• Tile/cascade multiple images on one screen</li> <li>• Timing data displayed with each image</li> <li>• Ciné editor</li> <li>• Multi Ciné Viewer</li> </ul> <p><b>Measurements:</b></p> <ul style="list-style-type: none"> <li>• Linear or angular measurements</li> <li>• Displacement</li> <li>• Velocity</li> <li>• RPMs</li> <li>• 100 data points per image</li> <li>• English and metric units</li> <li>• Generate measurement reports</li> <li>• Report files and images are compatible with spreadsheet software, and image analysis software such as TrackEye®, Image Express®, or Falcon®</li> </ul> <p><b>Image processing:</b></p> <ul style="list-style-type: none"> <li>• Smooth, sharpen, pseudocolor, negative image, and edge detection</li> <li>• Brightness, contrast and gamma adjust</li> <li>• 3x3 and 5x5 filter matrix for custom image processing</li> <li>• Unprocessed original cine is saved as a separate file</li> </ul> <p><b>File management:</b></p> <ul style="list-style-type: none"> <li>• Organize, save, compress and export cinés, or single images</li> <li>• File formats are compatible with most word processing, desktop publishing, and presentation software</li> </ul> <p><b>DIMENSIONS</b></p> <ul style="list-style-type: none"> <li>• <b>Size:</b> 4.3 x 4.0 x 9.5 in (12.5 x 11 x 25 cm) (HWD)</li> <li>• <b>Weight:</b> 7 lbs (3.2 kg)</li> <li>• <b>Power:</b> 28VDC/1.5 Amp</li> <li>• <b>Mounting:</b> 1/4-20 in and four 10-32 threaded hole pattern in base and top</li> <li>• <b>Mounting Axis:</b> Any position</li> <li>• <b>Material &amp; Finish:</b> Machined aluminum housing, powder coat finish</li> <li>• <b>Country of Origin:</b> United States of America</li> </ul> <p><b>STANDARD ACCESSORIES</b></p> <ul style="list-style-type: none"> <li>• Phantom® software. Single user license</li> <li>• 1024 MB integral image memory</li> <li>• FireWire® digital interface. Ethernet. Sync output pulse, trigger, video out, and IRIG-B</li> <li>• 110/220 VAC-28VDC International Power Adapter. 12 ft (3.7 m) power cord.</li> <li>• One year warranty</li> </ul> 
--	--	--



INSTRUMENTATION MARKETING CORP.

© Copyright 2001 All Rights Reserved.

Instrumentation Marketing Corp.  
820 S. Mariposa Street  
Burbank, CA 91506  
PH. 818-842-2141  
FAX 818-842-2610

email: Mail@photosonics.com

Photo-Sonics International Ltd.  
5 Thame Business Park  
Wenman Road, Thame  
Oxon. OX9 3FR  
England  
TEL +44(1844) 260600  
FAX +44(1844) 260126

A PHOTO-SONICS COMPANY



## Appendix A-2: Bronze Scorpio Data

Ev #	Event type	Frame rate (pps)	Frame Interval (us)	Exposure time (us)	Window size (x,y)
1	155mm TNT, erect	7500	133	121	512,384
3	155mm TNT, erect	7500	133	121	512,384
5	155mm TNT, erect	7500	133	121	512,384
7	155mm TNT, prone, broadside	7500	133	121	512,384
9	155mm TNT, prone, broadside	10000	100	90	512,384
11	105mm TNT, erect	10000	100	90	512,384
13	105mm TNT, erect	10000	100	90	512,384
15	105mm TNT, erect	10000	100	90	512,384
17	105mm TNT, prone, broadside	10000	100	90	512,384
19	105mm TNT, prone, broadside	10000	100	90	512,384
21	3 x 1.25# C-4	10000	100	90	512,384
23	155mm TNT, erect	10000	100	90	512,384
27	155mm TNT, prone, broadside	4800	208	192	800,600
29	155mm TNT, prone, broadside	4800	208	192	800,600
33	105mm TNT, erect	4800	208	192	800,600
35	105mm TNT, erect	4800	208	192	800,600
39	105mm TNT, erect	4800	208	192	800,600
42	105mm TNT, erect	4800	208	192	800,600
43	10# C-4	4800	208	192	800,600
46	155mm TNT, erect	4800	208	192	800,600
47	155mm TNT, erect	4800	208	192	800,600
52	155mm TNT, erect	24200	41	36	320,240
53	10# C-4	7270	138	36	640,480
54	155mm Comp B, erect	4800	208	36	800,600
56	155mm Comp B, erect	24200	41	36	320,240
57	2 x 155mm Comp B, erect	24200	41	36	320,240
59	2 x 155mm Comp B, erect	24200	41	36	320,240
61	event 61: 155mm CompB Plywood/Standing	26900	37	32	256,256
65	30# C-4	26900	37	13	256,256

The optic for all events was a Nikon 400mm focal length lens.

### Appendix A-3: NL2 Data

Trial number	Approx. date & time	Nominal charge mass (kg)	Charge composition	Charge geometry	Casing Material	Height of Burst (m)
0	Friday July 8 1415	20	C4 Rehearsal	Sphere	Polyethylene	3
1	Monday July 11 0845	20	C4 Baseline	Sphere	Polyethylene	3
2	Monday July 11 1400	20	C4 Baseline	Cylinder	Polyethylene	3
3	Monday July 11 1600	20	Mix 2	Sphere	Polyethylene	3
4	Tuesday July 12 0840	20	Mix 2	Cylinder	Polyethylene	3
5	Tuesday July 12 1355	20	Mix 4	Sphere	Polyethylene	3
6	Tuesday July 12 1555	20	Mix 4	Cylinder	Polyethylene	3
7	Wednesday July 13 0835	20	TSWG 1	Sphere	Polyethylene	3
8	Wednesday July 13 1350	20	TSWG 1	Cylinder	Polyethylene	3
9	Wednesday July 13 1550	20	TSWG 2	Sphere	Polyethylene	3
10	Wednesday July 13 1750	20	TSWG 2	Cylinder	Polyethylene	3
11	Thursday July 14 0830	20	Mix 2	Sphere	Aluminum	3
12	Thursday July 14 1345	20	Mix 2	Sphere	Steel	3
13	Thursday July 14 1545	20	Mix 2	Cylinder	Steel	3
14	Friday July 15 0825	20	Mix 4	Sphere	Aluminum	3
15	Friday July 15 1340	20	Mix 4	Sphere	Steel	3
16	Friday July 15 1540	20	Mix 4	Cylinder	Steel	3
17	Monday July 18 1325	150	Mix 2	Sphere	Polyethylene	6
18	Tuesday July 19 1320	150	Mix 2	Cylinder	Polyethylene	6
19	Wednesday July 20 1315	150	Mix 2	Sphere	Aluminum	6
20	Thursday July 21 1310	150	Mix 2	Sphere	Steel	6
21	Friday July 22 1305	150	Mix 2	Cylinder	Steel	6

### Appendix A-3: NL2 Data

Trial number	Camera Settings				Comments
0	Frame rate (pps)	Frame interval (us)	Exposure time (us)	Window size (x,y)	
1	5000	200	90	512,384	
2	10000	100	90	512,384	Changed phantom lens from AFIT Nikon to our 400mm lens. Much closer picture
3	4800	208	90	512,384	
4	10000	100	95	512,384	
5	10000	100	62	512,384	
6	10000	100	62	512,384	
7	10000	100	62	512,384	
8	10000	100	62	512,384	
9	10000	100	62	512,384	
10	10000	100	62	512,384	
11	10000	100	62	512,384	
12	10000	100	90	512,384	
13	10000	100	90	512,384	
14	10000	100	90	512,384	
15	10000	100	90	512,384	No data
16	x	x	x	x	No data
17	x	x	x	x	
18	10000	100	40	512,384	
19	10000	100	40	512,384	
20	10000	100	40	512,384	
21	10000	100	40	512,384	
	10000	100	40	512,384	

#### Appendix A-4: DTSS data

Test #	1	2	3	4	5	6
Time	1920	1938	1959	2024	2048	2106
Datafile	no collection	dat02.cin	dat03.cin	dat04.cin	dat05.cin	dat06.cin
File size (GB)	N/A	3.2	3.89	2.7	2.43	2.81
Recording time (seconds)	N/A	7.158	8.684	6.054	5.456	6.298
Optic	Nikon, 180mm focal length	Nikon, 180mm focal length	Nikon, 180mm focal length	Nikon, 180mm focal length	Nikon, 180mm focal length	Nikon, 180mm focal length
Aperture setting	22	22	22	22	22	22
Target distance (ft)	139	139	139	139	139	139
FOV (x,y) (radians)	0.0978, 0.0733	0.0978, 0.0733	0.0978, 0.0733	0.0978, 0.0733	0.0978, 0.0733	0.0978, 0.0733
Linear span at target distance (x,y) (meters)	4.121,3.091	4.121,3.091	4.121,3.091	4.121,3.091	4.121,3.091	4.121,3.091
Window size (x,y) (pixels)	800,600	800,600	800,600	800,600	800,600	800,600
Frame rate (pictures per second)	1000	1000	1000	1000	1000	1000
Exposure time (microseconds)	944	944	944	944	944	944
Camera trigger	manual, post trigger	manual, post trigger	manual, post trigger	manual, post trigger	manual, post trigger	manual, post trigger
Video format	NTSC	NTSC	NTSC	NTSC	NTSC	NTSC

## Appendix A-5: Muzzle Flash data

Test	TPL muzzle flash	TPL muzzle flash	TPL muzzle flash	TPL muzzle flash	TPL muzzle flash	TPL muzzle flash
Event	1 x .45, unk flash	2 x .45, unk flash	1 x .45, unk flash	1 x .45, unk flash	1 x .45, unk flash	1 x .45, unk flash
Date/time	28-Nov	28-Nov	28-Nov	28-Nov	29-Nov	29-Nov
Filename	mfest01	mfest02	mfest03	mfest04	dat_s001	dat_s002
Event frame #s	4683	6069, 9217	2660	2663	6646	2958
Weather	n/a, indoors	n/a, indoors	n/a, indoors	n/a, indoors	n/a, indoors	n/a, indoors
Optic	Nikon 20-35 mm, zoom	Nikon 20-35 mm, zoom	Nikon 20-35 mm	Nikon 20-35 mm, zoom	Nikon 180 mm fl	Nikon 180 mm fl
Aperture stop	4	2.8	2.8	2.8	2.8	2.8
Field stop	n/a	n/a	n/a	n/a	n/a	n/a
zoom	unk	unk	unk	unk	n/a	n/a
Target dist. (in)	72	72	72	72	72	72
Window size (x,y)	unk	unk	unk	unk	800,600	800,600
Frame rate (pps)	2000	1500	1500	1500	1500	1000
Exposure time (us)	470 us (max)	627 us (max)	627 us (max)	627 us (max)	627 us (max)	627 us (max)
Trigger	hard TTL pretrigger	hard TTL pretrigger	hard TTL pretrigger	hard TTL pretrigger	hard TTL pretrigger	hard TTL pretrigger
Video Format	NTSC	NTSC	NTSC	NTSC	NTSC	NTSC
Test	TPL muzzle flash	TPL muzzle flash	TPL muzzle flash	TPL muzzle flash	TPL muzzle flash	TPL muzzle flash
Event	1 x .45 3-r	1 x .45	3 x .45 con, fran	3 x .45 con, fran	3 x .45 con, fran	3 x .45 con, fran
Date/time	29-Nov	29-Nov	29-Nov	29-Nov	29-Nov	29-Nov
Filename	dat_s003	dat_s004	dat_c005	dat_c006	dat_c007	dat_c008
Event frame #s	2553	403	242, 320, 378	559, 759, 1199	1685, 2048, 2430	1984, 2369, 3250
Weather	n/a, indoors	n/a, indoors	n/a, indoors	n/a, indoors	n/a, indoors	n/a, indoors
Optic	Nikon 52 mm fl	Nikon 52 mm fl	Nikon 52 mm fl	Nikon 52 mm fl	Nikon 52 mm fl	Nikon 52 mm fl
Aperture stop	1.8	1.8	1.8	1.8	1.8	1.8
Field stop	n/a	n/a	n/a	n/a	n/a	n/a
Zoom	n/a	n/a	n/a	n/a	n/a	n/a
Target dist. (in)	40.5	40.5	40.5	40.5	40.5	40.5
Window size (x,y)	320,240	512,256	512,512	512,512	512,512	512,512
Frame rate (pps)	1000	100	100	200	500	1000
Exposure time (us)	947 (max)	9495 (max)	9495 (max)	4745 (max)	1895 (max)	945 (max)
Trigger	hard TTL pretrigger	hard TTL pretrigger	hard TTL pretrigger	hard TTL pretrigger	hard TTL pretrigger	hard TTL pretrigger
Video Format	NTSC	NTSC	NTSC	NTSC	NTSC	NTSC



## Appendix A-5: Muzzle Flash data

Test	TPL muzzle flash	TPL muzzle flash	TPL muzzle flash	TPL muzzle flash	TPL muzzle flash	TPL muzzle flash
Event	.45 nov, fran	1 x .45 nov, fran	2 x .45 nov, fran	6 x .45 con, fran	6 x .45 con, fran	4 x .45 con, fran
Date/time	29-Nov	29-Nov	29-Nov	30-Nov	30-Nov	30-Nov
Filename	n/a, no data collected	dat_n010	dat_n011	dat_c012	dat_c013	dat_c014
Event frame #s	n/a	254	223, 302	337, 408, 480, 546, 611, 673	233, 300, 366, 429, 488, 547	259, 314, 368, 419
Weather	n/a	n/a, indoors	n/a, indoors	n/a, indoors	n/a, indoors	n/a, indoors
Optic	n/a	Nikon 52 mm fl	Nikon 52 mm fl	Nikon 52 mm fl	Nikon 52 mm fl	Nikon 52 mm fl
Aperture stop	n/a	1.8	1.8	1.8	1.8	1.8
Field stop	n/a	n/a	n/a	n/a	n/a	n/a
Zoom	n/a	n/a	n/a	n/a	n/a	n/a
Target dist. (in)	n/a	40.5	40.5	25	25	25
Window size (x,y)	n/a	512,256	512,512	800,600	800,600	800,600
Frame rate (pps)	n/a	100	100	100	100	100
Exposure time (us)	n/a	9495 (max)	9495 (max)	9495 (max)	9495 (max)	9495 (max)
Trigger	n/a	hard TTL pretrigger	hard TTL pretrigger	hard TTL pretrigger	hard TTL pretrigger	hard TTL pretrigger
Video Format	n/a	NTSC	NTSC	NTSC	NTSC	NTSC
Test	TPL muzzle flash	TPL muzzle flash	TPL muzzle flash	TPL muzzle flash	TPL muzzle flash	TPL muzzle flash
Event	4 x .45 con, fran	7 x .45 nov, fran	7 x .45 nov, fran	7 x .45 nov, fran	7 x .45 nov, fran	.45 nov, fran
Date/time	30-Nov	30-Nov	30-Nov	30-Nov	30-Nov	30-Nov
Filename	dat_c015	dat_n016	dat_n017	dat_n018	dat_n019	n/a, no data
Event frame #s	232, 300, 358, 416, 471, 526, 580	248, 309, 374, 436, 499, 564, 623	279, 348, 415, 481, 549, 611	322, 392, 458, 525, 592, 653, 712	257, 326, 386, 441, 496, 551, 602	n/a
Weather	n/a, indoors	n/a, indoors	n/a, indoors	n/a, indoors	n/a, indoors	n/a
Optic	Nikon 52 mm fl	Nikon 52 mm fl	Nikon 52 mm fl	Nikon 52 mm fl	Nikon 52 mm fl	n/a
Aperture stop	1.8	1.8	1.8	1.8	1.8	n/a
Field stop	n/a	n/a	n/a	n/a	n/a	n/a
Zoom	n/a	n/a	n/a	n/a	n/a	n/a
Target dist. (in)	25	25	25	25	25	n/a
Window size (x,y)	800,600	800,600	800,600	800,600	800,600	n/a
Frame rate (pps)	100	100	100	100	100	n/a
Exposure time (us)	9495 (max)	9495 (max)	9495 (max)	9495 (max)	9495 (max)	n/a
Trigger	hard TTL pretrigger	hard TTL pretrigger	hard TTL pretrigger	hard TTL pretrigger	hard TTL pretrigger	n/a
Video Format	NTSC	NTSC	NTSC	NTSC	NTSC	n/a

## Appendix A-5: Muzzle Flash data

Test	TPL muzzle flash	TPL muzzle flash	TPL muzzle flash	TPL muzzle flash	TPL muzzle flash	TPL muzzle flash
Event	4 x .45 con, fran	7 x .45 nov, fran	7 x .45 nov, fran	7 x .45 nov, fran	7 x .45 nov, fran	.45 nov, fran
Date/time	30-Nov	30-Nov	30-Nov	30-Nov	30-Nov	30-Nov
Filename	dat_c015	dat_n016	dat_n017	dat_n018	dat_n019	n/a, no data
Event frame #s	232, 300, 358, 416, 471, 526, 580	248, 309, 374, 436, 499, 564, 623	279, 348, 415, 481, 549, 611	322, 392, 458, 525, 592, 653, 712	257, 326, 386, 441, 496, 551, 602	n/a
Weather	n/a, indoors	n/a, indoors	n/a, indoors	n/a, indoors	n/a, indoors	n/a
Optic	Nikon 52 mm fl	Nikon 52 mm fl	Nikon 52 mm fl	Nikon 52 mm fl	Nikon 52 mm fl	n/a
Aperture stop	1.8	1.8	1.8	1.8	1.8	n/a
Field stop	n/a	n/a	n/a	n/a	n/a	n/a
Zoom	n/a	n/a	n/a	n/a	n/a	n/a
Target dist. (in)	25	25	25	25	25	n/a
Window size (x,y)	800,600	800,600	800,600	800,600	800,600	n/a
Frame rate (pps)	100	100	100	100	100	n/a
Exposure time (us)	9495 (max)	9495 (max)	9495 (max)	9495 (max)	9495 (max)	n/a
Trigger	hard TTL pretrigger	hard TTL pretrigger	hard TTL pretrigger	hard TTL pretrigger	hard TTL pretrigger	n/a
Video Format	NTSC	NTSC	NTSC	NTSC	NTSC	n/a
Test	TPL muzzle flash	TPL muzzle flash	TPL muzzle flash	TPL muzzle flash	TPL muzzle flash	TPL muzzle flash
Event	7 x .45 con, fran	1 x .45 con, fran	7 x .45 con, fran	5 x .45 con, fran	2 x .45 con, fran	1 x .45 con, fran
Date/time	30-Nov	30-Nov	30-Nov	30-Nov	30-Nov	30-Nov
Filename	dat_c021	dat_c022	dat_c023	dat_c024	dat_c025	dat_c026
Event frame #s	487, 623, 748, 877, 1003, 1121, 1236	423	513, 598, 681, 765, 852, 942, 1029	527, 618, 707, 794, 882	545, 636	451
Weather	n/a, indoors	n/a, indoors	n/a, indoors	n/a, indoors	n/a, indoors	n/a, indoors
Optic	Nikon 52 mm fl	Nikon 52 mm fl	Nikon 52 mm fl	Nikon 52 mm fl	Nikon 52 mm fl	Nikon 52 mm fl
Aperture stop	1.8	1.8	1.8	1.8	1.8	1.8
Field stop	n/a	n/a	n/a	n/a	n/a	n/a
Zoom	n/a	n/a	n/a	n/a	n/a	n/a
Target dist. (in)	25	25	25	25	25	25
Window size (x,y)	800,600	800,600	800,600	800,600	800,600	800,600
Frame rate (pps)	200	200	200	200	200	200
Exposure time (us)	4745 (max)	4745 (max)	4745 (max)	4745 (max)	4745 (max)	4745 (max)
Trigger	hard TTL pretrigger	hard TTL pretrigger	hard TTL pretrigger	hard TTL pretrigger	hard TTL pretrigger	hard TTL pretrigger
Video Format	NTSC	NTSC	NTSC	NTSC	NTSC	NTSC

## Appendix A-5: Muzzle Flash data

Test	TPL muzzle flash	TPL muzzle flash	TPL muzzle flash	TPL muzzle flash	TPL muzzle flash	TPL muzzle flash
Event	2 x .45 nov fran	1 x .45 nov fmj	6 x .45 nov fmj	6 x .45 nov fmj	6 x .45 nov fmj	6 x .45 nov fmj
Date/time	30-Nov	30-Nov	30-Nov	30-Nov	30-Nov	30-Nov
Filename	dat_n033	dat_n034	dat_n035	dat_n036	dat_n037	dat_n038
Event frame #s	469, 611	361	444, 595, 779, 940, 1192, 1432	441, 568, 721, 822, 947, 1023	399, 527, 634, 728, 820, 902	491, 606, 711, 798, 988, 1061
Weather	n/a, indoors	n/a, indoors	n/a, indoors	n/a, indoors	n/a, indoors	n/a, indoors
Optic	Nikon 52 mm fl	Nikon 52 mm fl	Nikon 52 mm fl	Nikon 52 mm fl	Nikon 52 mm fl	Nikon 52 mm fl
Aperture stop	1.8	1.8	1.8	1.8	1.8	1.8
Field stop	n/a	n/a	n/a	n/a	n/a	n/a
Zoom	n/a	n/a	n/a	n/a	n/a	n/a
Target dist. (in)	25	25	25	25	25	25
Window size (x,y)	800,600	800,600	800,600	800,600	800,600	800,600
Frame rate (pps)	200	200	200	200	200	200
Exposure time (us)	4745 (max)	4745 (max)	4745 (max)	4745 (max)	4745 (max)	4745 (max)
Trigger	hard TTL pretrigger	hard TTL pretrigger	hard TTL pretrigger	hard TTL pretrigger	hard TTL pretrigger	hard TTL pretrigger
Video Format	NTSC	NTSC	NTSC	NTSC	NTSC	NTSC
Test	TPL muzzle flash					
Event	5 x .45 Wolf fmj					
Date/time	30-Nov					
Filename	dat_cf39					
Event frame #s	347, 460, 548, 617, 683					
Weather	n/a, indoors					
Optic	Nikon 52 mm fl					
Aperture stop	1.8					
Field stop	n/a					
Zoom	n/a					
Target dist. (in)	25					
Window size (x,y)	800,600					
Frame rate (pps)	200					
Exposure time (us)	4745 (max)					
Trigger	hard TTL pretrigger					
Video Format	NTSC					

### Bibliography

1. Bronze Scorpio Test Report. National Air and Space Intelligence Center, 17 May 2005.
2. Dills, Anthony N., Kevin Gross, Glen P. Perram, "Detonation discrimination techniques using a Fourier Transform IR spectrometer system and a Near IR FPA."
3. Dual Thrust Smokey SAM test report. Air Force Research Laboratory, 26 October 2005.
4. Faber, T. E., *Fluid Dynamics for Physicists*. Cambridge University Press, New York, NY 1995.
5. Fickett, W., W. C. Davis, *Detonation Theory and Experiment*. Dover Publications, Inc. Mineola, NY 1979.
6. Gross, Kevin C., AFIT Doctoral Student, October 2005
7. Gross, Kevin C., Anthony N. Dills, Glen P. Perram, "The dynamics and spectroscopy of fireballs arising from the detonation of conventional explosive materials."
8. Hassel, E., et al, "Large-eddy simulation and laser diagnostic measurements of mixing in a coaxial jet mixer." *Chemical Engineering Science*, 2005.
9. Horvat, Andrej; Ivo Kljenak, Jure Marn, "Two Dimensional Large Eddy Simulation of Turbulent Natural Convection Due to Internal Heat Generation." *International Journal of Heat and Mass Transfer* 44:3985-3995 (2001)
10. Kagan, L., G. Sivashinski, "Effect of Lewis Number on Flame Propagation Through Vortical Flows" *Combust. Flame* 142:235-240 (2005)
11. Kagan, L., and G. Sivashinski., "Flame Propagation and Extinction in Large-Scale Vortical Flows" *Combust. Flame* 120:222-232 (1999)
12. Landau, L. D., E. M. Lifshitz, *Fluid Mechanics*. Pergamon Press, Ltd. New York, NY 1959
13. Northern Lights Trials II test report. National Air and Space Intelligence Center, 5 July 2005.

14. Orson, J. A., W. F. Bagby, and G. P. Perram, "Infrared signatures from bomb detonations," *Infrared Physics and Technology*, 44, pp.101-107, 2003.
15. Phantom Camera Control Software Documentation. Vision Research, Inc. Wayne, NJ 25 Nov 2003
16. Reinecke, Martin "Modeling and simulation of turbulent combustion in Type Ia Supernovae," Doctoral dissertation. Max-Planck-Institut Fur Astrophysik, 2001.
17. Tritton, D. J., *Physical Fluid Dynamics* Second Edition. Oxford University Press, NY 1988.
18. Tomomi, Uchiyama., Masaaki Naruse, "Three-dimensional vortex simulation for particulate jet generated by free falling particles." *Chemical Engineering Science*. Article in press 2005.
19. US Army. Army Material Command Pamphlet, AMCP 706-180 *Principals of Explosive Behavior*. Headquarters, US Army Materiel Command, April 1972.
20. Zel'dovich, Ya. B., Yu. P. Raizer, *Physics of Shockwaves and High-Temperature Thermodynamic Phenomena*. Dover Publications, Inc. Mineola, NY 19

REPORT DOCUMENTATION PAGE				Form Approved OMB No. 074-0188	
<p>The public reporting burden for this collection of information is estimated to average 1 hour per response, including the time for reviewing instructions, searching existing data sources, gathering and maintaining the data needed, and completing and reviewing the collection of information. Send comments regarding this burden estimate or any other aspect of the collection of information, including suggestions for reducing this burden to Department of Defense, Washington Headquarters Services, Directorate for Information Operations and Reports (0704-0188), 1215 Jefferson Davis Highway, Suite 1204, Arlington, VA 22202-4302. Respondents should be aware that notwithstanding any other provision of law, no person shall be subject to a penalty for failing to comply with a collection of information if it does not display a currently valid OMB control number.</p> <p><b>PLEASE DO NOT RETURN YOUR FORM TO THE ABOVE ADDRESS.</b></p>					
1. REPORT DATE (dd-mm-yyyy) 23-03-2006		2. REPORT TYPE Master's Thesis		3. DATES COVERED (From – To) March 2005 – March 2006	
4. TITLE AND SUBTITLE  CHARACTERIZATION OF DETONATION PHENOMENA OBSERVED IN HIGH-SPEED, VISIBLE IMAGERY				5a. CONTRACT NUMBER	
				5b. GRANT NUMBER	
				5c. PROGRAM ELEMENT NUMBER	
6. AUTHOR(S)  Warren, Trevor W, First Lieutenant, USAF				5d. PROJECT NUMBER	
				5e. TASK NUMBER	
				5f. WORK UNIT NUMBER	
7. PERFORMING ORGANIZATION NAMES(S) AND ADDRESS(S) Air Force Institute of Technology Graduate School of Engineering and Management (AFIT/EN) 2950 Hobson Way, Building 640 WPAFB OH 45433-8865				8. PERFORMING ORGANIZATION REPORT NUMBER  AFIT/GAP/ENP/06-20	
9. SPONSORING/MONITORING AGENCY NAME(S) AND ADDRESS(ES) National Air and Space Intelligence Center (NASIC/DEMI) 4180 Watson Way Wright Patterson AFB, OH 45433 Sharon Staley, NASIC/DEMI DSN: 787-2962				10. SPONSOR/MONITOR'S ACRONYM(S)	
				11. SPONSOR/MONITOR'S REPORT NUMBER(S)	
12. DISTRIBUTION/AVAILABILITY STATEMENT  APPROVED FOR PUBLIC RELEASE; DISTRIBUTION UNLIMITED.					
13. SUPPLEMENTARY NOTES					
14. ABSTRACT  Measurements for radius, angular velocity, initial time of observation, and final time of observation were made for turbulent vortices around detonation fireballs. A proxy for vortex power, determined through unit analysis, was found to correlate well to initial (and final) time of observation with $R^2$ equal to 0.8572. The linear trend on a $\log_{10}$ - $\log_{10}$ plot was indicative of a rapid decrease (over $10^{-1}$ s) in power associated with the decay of the fireball. Predictions, based on turbulent spectral theory were made for root-mean-square velocity fluctuations and Reynolds numbers, both as functions of time. In addition, reflected shock speeds inside the fireball were found to be, on average, 69% higher than those of the un-reflected shock outside. This difference in speed was used to estimate the adiabatic exponent inside the fireball. Values of the adiabatic exponent were found to range between 1.08 and 1.3, while exhibiting a decreasing trend in time, and a weak quadratic dependence on time. Lastly, comparisons of the primary and secondary shock velocities showed that the secondary shock was faster in eight out of ten events. For the remaining two events, the speeds were equal to within the uncertainty of the measurements. The speed of the secondary shock varied from 1.8% to 30% faster than the primary shock.					
15. SUBJECT TERMS Detonation, explosion, fireball, shockwave, vortices, turbulence, adiabatic exponent					
16. SECURITY CLASSIFICATION OF:			17. LIMITATION OF ABSTRACT	18. NUMBER OF PAGES	19a. NAME OF RESPONSIBLE PERSON
a. REPORT	b. ABSTRACT	c. THIS PAGE			Dr. Glen P. Perram AFIT/ENP
U	U	U	UU	118	19b. TELEPHONE NUMBER (Include area code) (937) 255-3636 Glen.Perram@afit.edu